PhD Thesis

Early kilonovae from neutron star mergers

(中性子星合体からの初期キロノバ放射)

Submitted by

Smaranika Banerjee

for

the partial fulfilment of the
degree of Doctor of Philosophy

Department of Astronomy,
GRADUATE SCHOOL OF SCIENCE,
Tohoku University

August 2022

This thesis is dedicated to all my teachers and role models, who inspired me to venture the wonderful worlds of Physics and Astronomy.

Acknowledgement

The last three years in Japan have been an enthralling experience for me. I have received lots of motivation and inspiration, which helped me to grow as a person and researcher. As I am concluding the journey here, I want to thank many people for supporting me throughout.

First and foremost, I would like to express my sincere gratitude to Dr. Masaomi Tanaka (Masaomi-san). He has been not only my PhD guide but also my mentor in science and research life. His support and guidance have helped me to understand the way of thinking and the attitude a researcher must possess. Also, I want to thank him for his never-ending 'why's, which have propelled me to delve deeper into the topic. Moreover, I have gained many insights from him about being a better writer and effective communicator. Finally, I also want to thank him for always ensuring that I do not need to worry about anything but science in a country where I do not speak the language.

I would like to take this opportunity to thank Dr. Varun Bhalerao, my former supervisor and present-day collaborator. He introduced me to the exciting field of Astronomy during master's, and I learned a lot about observational Astronomy, thanks to his constant and enthusiastic guidance and support.

I have been fortunate enough to have many collaborators in different disciplines from different parts of the world. I want to thank Prof. Gediminas Gediminas and Dr. Daiji Kato for their kind collaboration. They have taught me many things about Atomic Physics and research practises in Atomic Physics. Through this collaboration, I was able to gain expertise and contribute to many papers on the different disciplines of Atomic Physics.

I wish to express my sincere gratitude to Dr. Kenta Hotokezaka, whom I first met as a naive beginner of Astronomy in India. Since then, he has always been supportive and taught me many things about various topics on neutron star mergers. I want to thank Dr. Kyohei Kawaguchi, with whom I could discuss detailed things about coding in radiative transfer, and Dr. Hamid Hamidani, from whom I have learned many things on Hydrodynamic simulations. I would also like to thank Dr. Takayuki Ohgami for the collaboration. Also, I want to thank Dr. Masaru Shibata, Dr. Kunihito Ioka, Dr. Shinya Wanajo, Dr. Nozomu Tominaga, Dr. Sho Fujibayashi, with whom I have been fortunate enough to share thoughts and learn various things in different times during my PhD.

I am grateful to many senior colleagues at Tohoku University. I especially want to mention Dr. Kengo Tomida, from whom I have learned many things about simulations; Dr. Mitsuru Kokubo (now at Princeton University), discussions with whom has always been exciting due to his vast knowledge of different topics in Astronomy; Dr. Yutaka Hirai, from whom I learned many things about not only his research topic, galactic chemical evolution, but also the practical things about the career path as a researcher.

The journey during PhD has been fruitful and interesting, thanks to my peers at Tohoku University. I want to thank Sei Saito, who has always been very friendly. He discussed the various seminars and lectures that I could not attend because of

my poor Japanese. Also, discussing Japanese culture and language and going out for Ramen have been really amazing. Moreover, I want to thank Dr. Jose Perez, Janek Pflukart, Dr. Hei-Yin Jowett Chan and all others.

I want to thank my Indian Pakistani family in Sendai, who made it a little easier to survive far away from home during the global pandemic. Also, I want to thank my friend from China, Bien Zhen, who has helped me through many things in Japan. She also introduced me to many new things in Japan and got me acquainted with south-east Asian culture. I am glad to have this friendly environment in Japan.

Finally, I want to thank the people whose constant encouragement and support have made it possible for me to come this far. I am thankful to my parents for all their sacrifices and for making my education their priority. I also wish to express my gratitude to 'Mamoni' (uncle) Mr. Goutam Chatterjee, who has been a source of inspiration and support throughout my life; my grandmother, Mrs. Alo Mukherjee, for encouragement, and my bigger family for helping during difficult times. I want to thank Shreya Sarkar, for being the most wonderful friend and always being the source of comfort since undergrad.

Finally, I want to thank my coherent wavelength (soon-to-be Dr.) Bhrigu Rishi Mishra, without whom, the journey to being an Astronomer would have been impossible. He has constantly amplified my courage, even from $\sim$ 7000 km away during the global pandemic. I am really grateful to him for always rooting for me and my dream of being an Astronomer.

Abstract

The origin of elements heavier than iron (atomic number $Z > 26$) has been a long-standing mystery in astrophysics. It has broad implications for other research, such as chemical abundances in stars and the chemical evolution of the galaxies. Theoretical studies predict binary neutron star mergers as one of the most plausible sites for the heavy element synthesis. In the neutron-rich material ejected from the neutron star merger, heavy ($Z > 26$) elements are synthesized via rapid neutron capture (r-process). The radioactive decay of such elements produces emissions in the ultraviolet-optical-infrared range, which is called a kilonova. Detection of a kilonova is the proof of the heavy element synthesis in the neutron star merger ejecta.

Furthermore, the neutron star mergers are the sources of multi-messenger signal, e.g., they emit the gravitational waves and are also associated with the short gamma-ray bursts. The first detection of gravitational wave and electromagnetic signal from a neutron star merger (GW170817) ushered in a new era of multi-messenger astronomy. Also, the detection of a kilonova is made, which has proved that the neutron star mergers are indeed the sources of the heavy element synthesis. In future, many kilonova observations will be made and the theoretical preparations are essential to extract the information from the kilonova light curves. This work is motivated by such purpose.

The kilonova light curve and spectra depend on the bound-bound opacity of the heavy elements. Particularly, if lanthanides ($Z = 57-71$), i.e., the elements with the open f-shell, are present, the opacity is increased dramatically which affects the light curve. Hence, a detailed opacity calculation is necessary to model realistic kilonova light curves and spectra. However, such calculations were largely unavailable for the condition suitable at an early time ($t < 1$ day). Understanding the early kilonova is essential since because the emission at early time can reveal the abundance in the outer ejecta as the photons only from the outer layer can escape at an early time. Hence, understanding the kilonova light curve starting from an early time is important to reveal the abundance pattern from the outer to the inner ejecta.

In the neutron star merger, lighter ($Z \leq 56$) and heavier ($Z > 56$ including lanthanides) r-process elements are expected to be distributed near the pole and the equatorial region, respectively. Such abundance distribution introduces angle dependence to the light curve, especially at an early time ($t \sim$ hours after the merger). Hence, we need the atomic opacity for both the lanthanide-free and lanthanide-rich ejecta to calculate the early light curve of kilonova as observed from the different directions.

We present the detailed atomic structures and opacities of highly ionized elements (up to the tenth ionization) with atomic number $Z = 20 - 88$, suitable for ejecta condition at $t \sim 0.1$ day. We find that the mean opacity for lanthanide-free ejecta (with the abundance of the elements with $Z < 56$) is $\kappa \sim 0.5 - 1\,\mathrm{cm^2\,g^{-1}}$ at $t = 0.1$ day, whereas that for lanthanide-rich ejecta can reach up to $\kappa \sim 5000\,\mathrm{cm^2\,g^{-1}}$ at $t = 0.1$ day.

Using the new opacity, we perform the radiative transfer simulations for the simple spherical ejecta model with the ejecta mass of $M_{\rm ej} = 0.05 M_\odot$ for both the lanthanide-free and lanthanide-rich models, which represent the situation similar to the observation from the polar and equatorial direction. We find that for the lanthanide-free ejecta, the bolometric luminosity is $\sim 2 \times 10^{42}\,{\rm erg\,s^{-1}}$ at $t \sim 0.1$ day. We confirm that the existing early bolometric and multi-color data of GW170817 can be naturally explained by the purely radioactive model of lanthanide-free ejecta. Moreover, we find that if the lanthanides are present in the ejecta, the early light curves become fainter by a (maximum) factor of four, in comparison to lanthanide-free ejecta at $t \sim 0.1$ day. However, the period at which the light curves are affected is relatively brief due to the rapid time evolution of the opacity in the outermost layer of the ejecta.

We predict that, for a source at a distance of ~ 100 Mpc, UV brightness for lanthanide-free kilonova reach 19 mag at $t \sim 0.1$ day, whereas the magnitude for the lanthanide-rich ejecta at $t \sim 0.1$ day can reach only to a magnitude of $\sim 21-22$ mag. Nevertheless, detection of the early kilonova is possible for both lanthanide-free and lanthanide-rich case by the existing UV satellite like *Swift* or the future UV satellites (e.g., ULTRASAT, DORADO, UVEX). Such future detections will provide useful constraints on the abundance in the outer layer of the ejecta and the corresponding nucleosynthesis conditions in the neutron star mergers.

Our work provides the foundation for the more detailed study by constructing the fundamental dataset for atomic opacity. In the future, together with the observations, our work will contribute towards the understanding of *the origin of heavy elements*.

Contents

Chapter 1

Introduction

1.1 Origin of heavy elements

The origin of heavy elements has been a long-standing mystery. According to the current understanding of Big Bang nucleosynthesis, only the lightest of the elements, ^{1,2}H, ^{3,4}He, and ^{7}Li were synthesized during Big Bang. But in the Universe today, we see 92 naturally occurring elements, most of which have at least one stable isotope (see Figure 1.1 for the abundance in the solar system). Hence, the question arises about where does the elements heavier than ^{7}Li, i.e., the elements with $Z > 3$, come from?

A part of the question has been answered in the last century. The elements from the ^{12}C to the iron group elements ($Z \leq 30$) are synthesized during the evolution and the death of the stars via type Ia or core-collapse supernova in the massive stars ($M > 8M_{\odot}$, e.g., Burbidge et al., 1957; Cameron, 1957; Woosley & Heger, 2007). However, such nucleosynthesis cannot explain the origin of the elements beyond the iron group elements (e.g., elements like Ba, Pb, Au, Pt and so on).

To understand the origin of the elements beyond the iron peak elements, we need to first consider the nucleosynthesis condition under which the heavy elements are synthesized. It is well known that the nucleosynthesis inside the stars happens mainly via the charged particle capture. For example, inside the main sequence stars, the net reaction to convert ^{1}H to ^{4}He is as follows:

$$4\,^{1}\mathrm{H} \rightarrow {}^{4}\mathrm{He} + 2\beta^{+} + 2\nu_{\mathrm{e}} + 2\gamma + 24.64\,\mathrm{MeV} \tag{1.1}$$

Beyond iron, elements cannot be synthesized via charged particle capture since the process becomes endothermic owing to the fact that iron has the highest nuclear binding energy. Instead, heavier elements are synthesized mainly via neutron capture. Another nucleosynthesis process, proton capture (p-process), also exists, which can explain the extremely small amount of the neutron deficit elements observed exclusively in the solar system (e.g., ^{138}La, Arnould & Goriely, 2003). Here we discuss nucleosynthesis via neutron capture only.

Neutron capture happens in an environment where the neutron density is high, about $n_{\mathrm{n}} \geq 10^{8}\,\mathrm{cm}^{-3}$ (Frebel, 2018). The outcome of the neutron capture nucleosynthesis varies depending on whether the neutron capture timescale is faster than

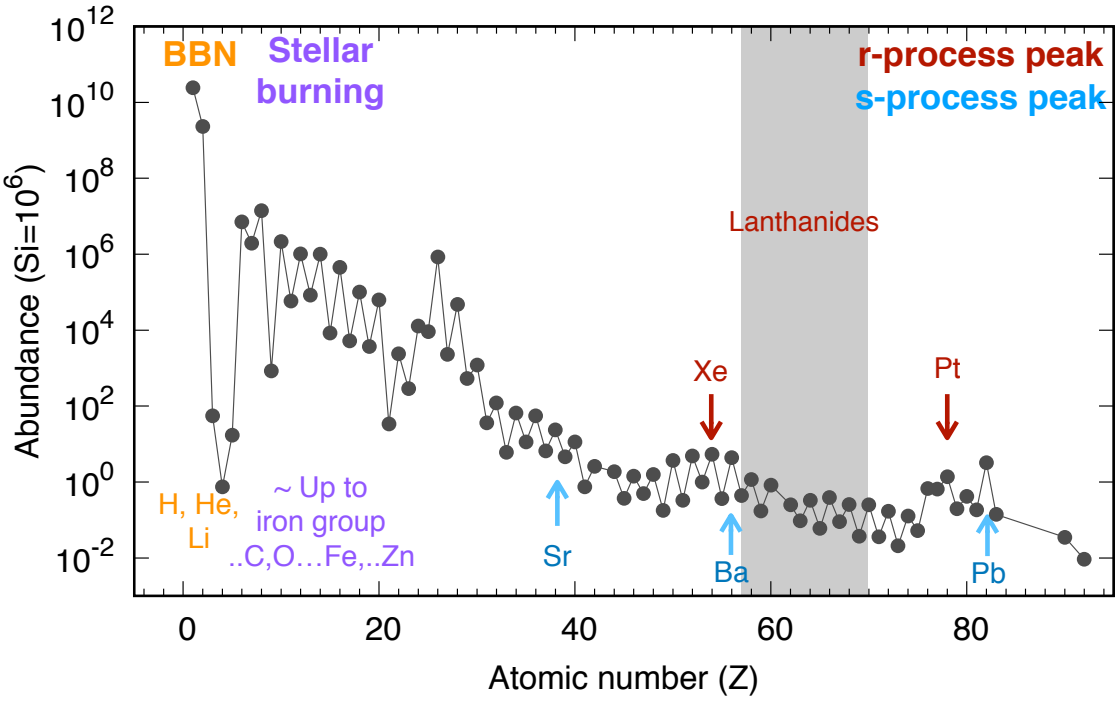

Figure 1.1: Abundance of the elements in solar systems. The data is from Lodders (2003).

that of the β-decay timescale. If the neutron capture occurs on a timescale slower than that of the β-decay (slow-process or s-process), then the elements such as ^{138}Ba are produced (Ott et al., 2019). s-process occurs inside the double shell (^{1}H and ^{4}He) burning low-mass asymptotic giant branch stars ($M < 8M_\odot$).

However, s-process can not explain the origin of the neutron-rich isotopes such as ^{195}Au. These elements are produced if the neutrons are captured on a timescale faster than β-decay (rapid-neutron capture process or r-process). Such nucleosynthesis happens at an extremely neutron-rich environment $n_n \geq 10^{22}\,\mathrm{cm}^{-3}$ (Frebel, 2018).

The sites where such high neutron density suitable for the r-process nucleosynthesis can be realized has been a long unsolved question in astrophysics. Different sites have been proposed, such as, the magneto-rotational supernova (Nishimura et al., 2015) and the compact object mergers, i.e., the merger of the two neutron star or a neutron star and a black hole (Lattimer & Schramm, 1974; Eichler et al., 1989; Freiburghaus et al., 1999; Korobkin et al., 2012; Wanajo et al., 2014). Recently neutron star merger has been confirmed to be the sites of r-process nucleosynthesis. However, it is not yet established whether these are the only sites for the r-process nucleosynthesis (Côté et al., 2019).

Understanding the r-process site has broader application in several fields, such as, galactic chemical evolution (GCE), where we study the evolution of the chemical composition of a galaxy. The lack of understanding of the source of the r-process elements (unlike the other sources of chemical enrichment, such as stars) introduces uncertainties in the predictions of GCE.

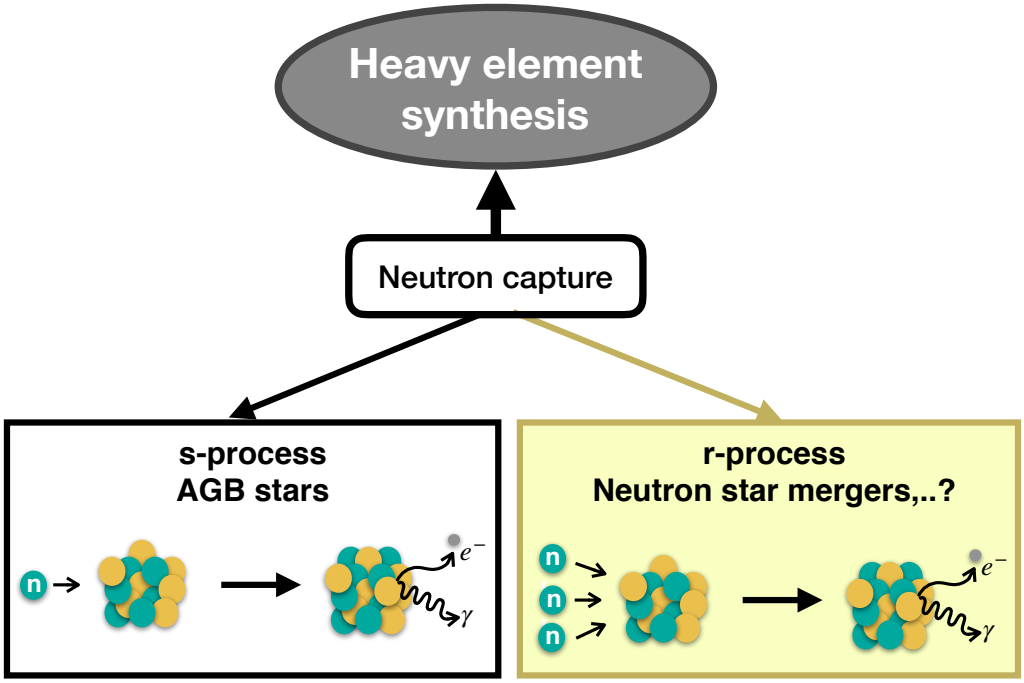

Figure 1.2: The nucleosynthesis channels for the heavy element synthesis beyond iron peak elements. The neutron star mergers are the only confirmed channel for r-process nucleosynthesis to produce the heavy elements.

We can consider evolution of Eu (mostly r-process element) in galactic disk to understand the scenario. [Eu/Fe] evolution with [Fe/H] shows decreasing trend similar to the [α/Fe] evolution with [Fe/H] (Côté et al., 2019). To explain such a trend, many GCE models predict two different sources with early and late delay time for Eu production, similar to the type Ia and core-collapse supernova as the sources for Fe production (Côté et al., 2019). Therefore, it is important to understand the source of the r-process elements for broader field of applications.

In this thesis, we focus on the neutron star mergers as the source of the r-process elements to understand *the cosmic origin of heavy elements*. Our study will also contribute to the other fields of study, such as GCE.

1.2 Neutron star merger

1.2.1 Overview

Neutron stars are the remnants of the massive stars ($M > 8M_\odot$) after the core-collapse. No stellar burning occurs inside them. The maximum mass of the neutron stars is predicted to be around $\leq 2.6M_\odot$ for a radius of $10 - 14$ km depending on the equation of state, which is still highly uncertain (Özel & Freire, 2016).

The neutron star binaries should be abundant in the Universe since more than

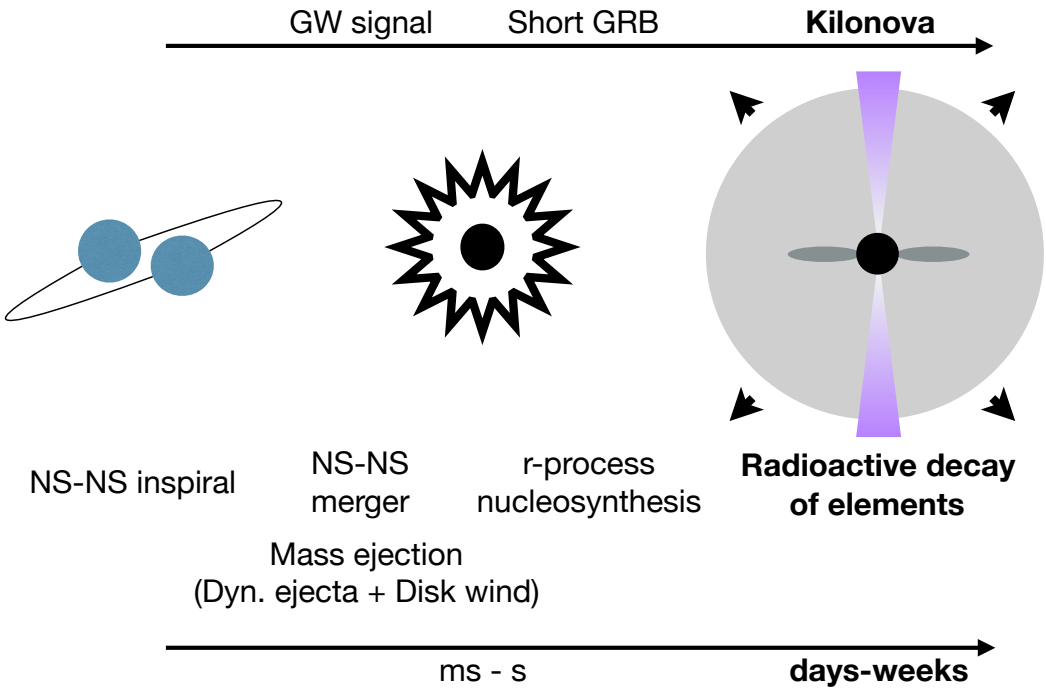

Figure 1.3: The multi-messenger signal from the neutron star merger. The gravitational wave at the moment of the merger is detectable by the ground-based gravitational wave observatories (Nissanke et al., 2013). A relativistic jet might get launched producing a short GRB $\sim$ seconds after the merger. Finally, the radioactive decay of the heavy elements produce the UVOIR signal in a timescale of days to weeks.

50% of the massive stars spend their main sequence lifetime in binaries (Rosswog & Brüggen, 2011). However, the stellar binaries must survive the supernova explosions of their companion to form compact object binaries. Whether such a scenario actually occurs had remained an open question until the seminal discovery of the Hulse-Taylor binary pulsar (pulsar is a highly magnetized neutron star) in 1975 (Hulse & Taylor, 1975).

Two orbiting neutron stars loose energy via emission of the gravitational wave (GW) by the prediction of the General Relativity (Peters & Mathews, 1963). Since the GW carries away energy and the angular momentum, the orbit of the binary shrinks and finally the neutron stars merge. If the merger time is less than the Hubble time, then the neutron star mergers can explain the enrichment of the galaxies with the r-process elements. The fact that at least for some binaries, the merger time is shorter than the Hubble time is established by the discovery of such neutron star binaries in our Galaxy (e.g., Hulse-Taylor binary, Taylor & Weisberg, 1982, also see Wolszczan, 1991; Tauris et al., 2017 for other such binaries in our Galaxy).

During the neutron star merger, a small fraction of the mass is ejected (typically $\sim$ 1% of the solar mass). The ejected material is enough neutron rich so that the

r-process nucleosynthesis occurs. The neutron richness of the ejecta is described by a quantity called the electron fraction, defined as the electron to the baryon ratio ($Y_{\rm e} = n_{\rm e}/(n_{\rm p} + n_{\rm n})$). The electron fraction for neutron star mergers can be as low as $Y_{\rm e} = 0.1$, which is suitable for the production of the heaviest elements such as ^{196}Pt.

The radioactive decay of freshly synthesized heavy elements gives rise to the electromagnetic transient in the ultraviolet, optical, and near infrared (UVOIR) spectrum, similar to the supernova (Li & Paczyński, 1998; Kulkarni, 2005), but on a faster timescale ($\sim$ days - week) and with lower peak luminosities (Metzger et al., 2010; Roberts et al., 2011; Kasen et al., 2013; Tanaka & Hotokezaka, 2013). These transients are called kilonovae (Metzger et al., 2010) or macronovae (Kulkarni, 2005). The UVOIR signal are detectable from space and ground based observatories.

The kilonova signal from the neutron star mergers provide the important hint to understand the origin of heavy elements. Furthermore, The neutron star mergers are important from several other perspectives. For instance, the neutron star mergers are the ideal target for GW observation for the ground based GW networks. Moreover, a relativistic jet is launched after the merger and these mergers are assumed to be associated with the short gamma-ray bursts (short GRB, e.g., Narayan et al., 1992; Paczynski, 1986). Additionally, jet interaction with the surrounding medium produces afterglow signal in X-ray, radio, and optical band.

In summary, neutron star mergers are the sources of the multi-messenger signal (see Figure 1.3) and are important for several reasons. We are interested in the kilonova signal from such mergers since it can be used as a probe to answer the fundamental questions regarding *the origin of heavy elements*.

1.2.2 Observation

First multi-messenger signal from a neutron star merger (GW170817) were detected during the second observing run (O2, Abbott et al., 2017a,b) of the ground based GW detector networks (Laser Interferometer Gravitational-wave Observatory (LIGO) in Livingston, Hanford, and Virgo in Italy), which have been routinely performing the GW observation during the last decade (e.g., Abbott et al., 2019). A short GRB was coincidentally detected at $t \sim 2$ s (where t is the time since the merger) X-ray and radio afterglow were also detected at $t \sim 9$ days and $t \sim 16$ days, respectively (Troja et al., 2017; Hallinan et al., 2017; Mooley & Mooley, 2017). The optical and near-infrared emissions were detected at $t \sim 11$ hours (Coulter et al., 2017; Yang et al., 2017; Valenti et al., 2017), followed by the detection of a bright UV emission by Swift (Evans et al., 2017) at $t \sim 16$ hours (see Figure 1.4 for the bolometric and multi-color light curves of GW170817).

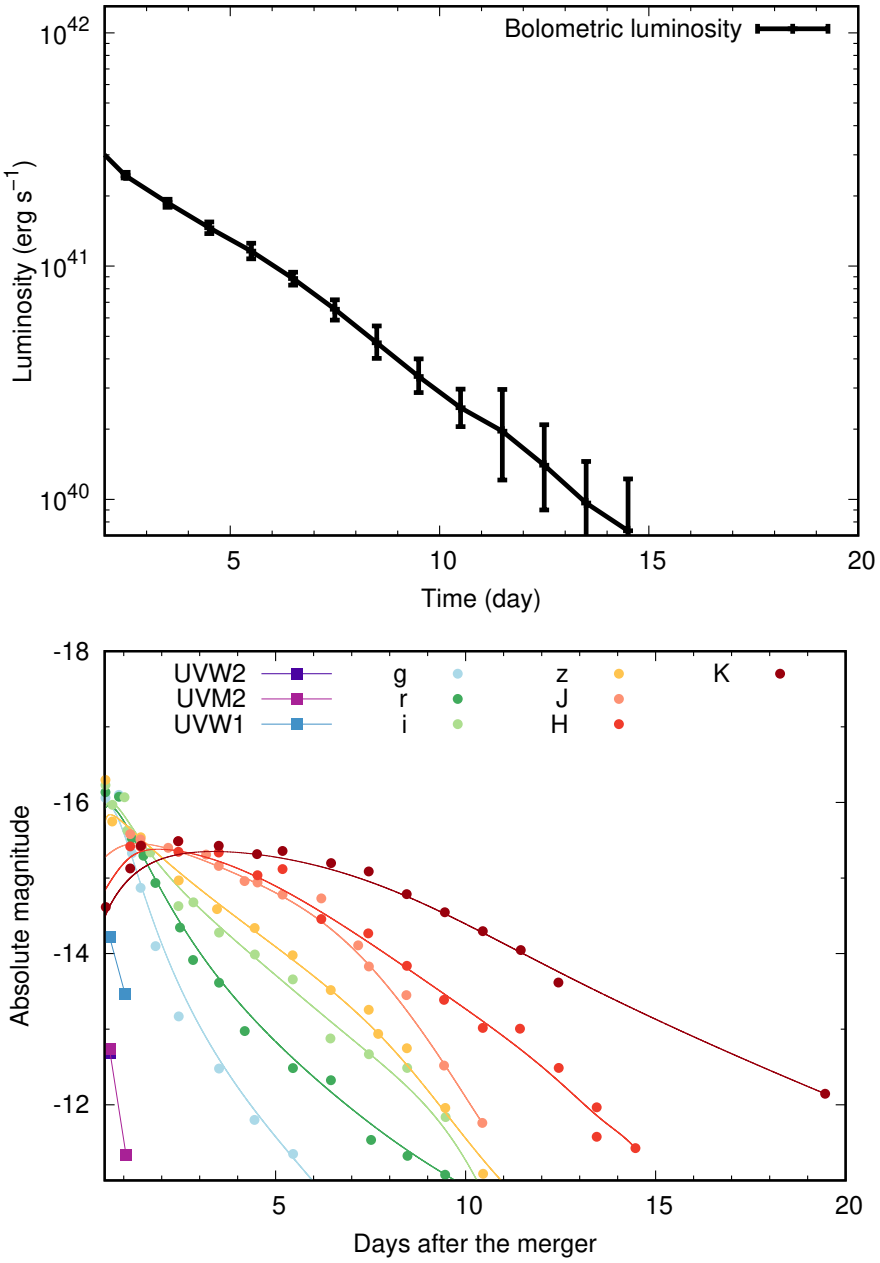

Figure 1.4: The bolometric (top, data from Waxman et al., 2018) and multi-color light curves (bottom, data compiled by Villar et al., 2017) of the kilonova associated with GW170817.

The extensive dataset for GW170817 provide us with a novel way to probe the various physical aspects of neutron star mergers:

- GW170817 puts a limit on the equation of states for the neutron star (e.g., Abbott et al., 2018).
- GRB170817 proves the long assumed association between short GRBs and neutron star mergers (e.g., Connaughton et al. 2017; Savchenko et al. 2017b).
- The thermal emission, specially that at a timescale ($t > 1$ day), are well explained by kilonova (e.g., Kasen et al. 2017; Tanaka et al. 2017; Shibata et al. 2017; Perego et al. 2017; Rosswog et al. 2018; Kawaguchi et al. 2018). This has established the neutron star mergers to be one of the r-process nucleosynthesis sites.

GW from another binary neutron star merger GW190425 (Abbott et al., 2020) is detected in GW network during the third observing run (O3) although no associated EM counterpart was detected (Coughlin et al., 2019).

The fourth observing run for GW observation (O4) is scheduled to start around $\sim$ March of 2023. With the increase in sensitivity of the GW networks and the new detector KAGRA joining, $\sim 10^{+52}_{-10}$ binary neutron star mergers are expected to be annually detected. Many new telescopes are also proposed for effective follow-up of electromagnetic signal, such as, the wide-field satellite in UV (e.g., ULTRASAT, Sagiv et al., 2014), the time-domain survey instrument in IR (Wide-Field Infrared Transient Explorer or WINTER, Frostig et al., 2022). Hence, the detection prospects of kilonovae are bright in the near future and theoretical preparation is necessary to extract information from observations.

1.3 Kilonova from neutron star merger

The idea of kilonova is introduced by Li & Paczyński (1998). They propose that the radioactive ejecta after the neutron star merger produce a thermal transient similar to supernova. The transient is named kilonova by Metzger et al. (2010), who derive the luminosity scale of the transient ($L_{\rm peak} \sim 10^{41}\,{\rm erg\,s^{-1}}$) and find that it is ~ 1000 times brighter than a nova. The transient is also regarded by the name 'macronova' (Kulkarni, 2005). This name is sometimes preferred over kilonova since it is not connected to the particular luminosity scale, which might be subject to change with the advancement in modelling or new observations. In the thesis, we use the name kilonova for the sake of convenience.

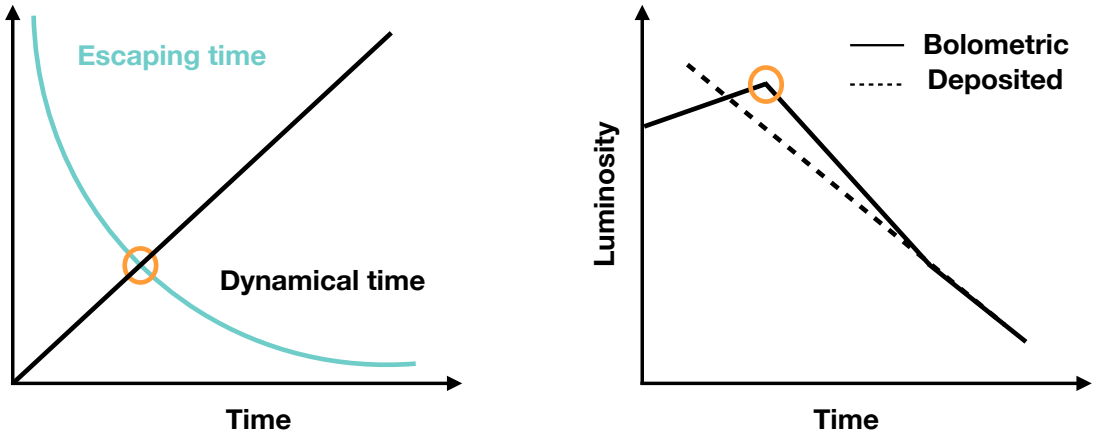

Figure 1.5: The diffusion time evolution with time (left) for an expanding ejecta. When the diffusion timescale becomes equal to the expansion timescale, the peak of the light curve appears (right).

1.3.1 Light curve

The emission mechanism in kilonova is similar to that in the type Ia supernova. Nonetheless, there are a few key differences:

1. The main energy source for kilonova is the radioactive decay of the r-process elements, whereas that in the case of the type Ia supernova is mainly the radioactive decay of the ^{56}Ni (the chain reaction $^{56}\mathrm{Ni} \rightarrow {}^{56}\mathrm{Co} \rightarrow {}^{56}\mathrm{Fe}$).

2. The total mass of the ejecta in case of type Ia supernova ($\sim 1.4 M_{\odot}$) is much higher than that for kilonova ($\sim 0.01 M_{\odot}$).

3. The velocity of the supernova ejecta ($\sim 10000\,\mathrm{km\,s^{-1}}$) is lower than that of the neutron star merger ejecta ($> 30000\,\mathrm{km\,s^{-1}}$).

Keeping the differences in mind, we can model the kilonova following the same prescription as suggested by Arnett (1982) for supernovae. Suppose the spherical and homogeneous ejecta with a continuous radioactive heating are expanding homologously. The radioactive heating heats up the ejecta which emit thermal photons. The thermal photons interact with the ejecta and finally when the photons escape, the kilonova shines. The escape timescale of the photons is determined by the optical depth of the ejecta, which can be determined as $\tau = \rho\kappa R$. Here R is the ejecta radius and κ is the mass absorption coefficient or opacity (in units of $\mathrm{cm^2\,g^{-1}}$). The opacity, κ, is determined by the particular abundances in the ejecta.

The diffusion timescale in the ejecta can be estimated from the optical depth as

$$t_{\mathrm{diff}} = \frac{R}{c}\tau \sim \frac{3\kappa M_{\mathrm{ej}}}{4\pi c v t} \tag{1.2}$$

Here we have adopted $M_{\mathrm{ej}} = (4\pi/3)\rho R^3$ for the homogeneously expanding ejecta. Additionally, since the ejecta are assumed to be expanding homologously, i.e., since

the fractional rate of change in the velocity is constant, we assume $r = vt$, where t is the expansion timescale.

For the photons to effectively diffuse through the ejecta, the diffusion timescale must be comparable to the dynamical timescale $t_{\rm diff} \sim t_{\rm dyn}$ (Figure 1.5). Then the characteristic timescale can be written as:

$$t_{\rm peak} = \left(\frac{3\kappa M_{\rm ej}}{4\pi c v}\right)^{1/2} \sim 8.4\,{\rm days}\left(\frac{M_{\rm ej}}{0.01{\rm M}_\odot}\right)^{0.5}\left(\frac{v}{0.1{\rm c}}\right)^{-0.5}\left(\frac{\kappa}{10\,{\rm cm^2\,g^{-1}}}\right)^{0.5} \quad (1.3)$$

The peak luminosity can be approximated from the deposition luminosity at $t_{\rm peak}$ (Figure 1.5, Arnett, 1982). Hence, we can determine the light curve by estimating the deposition at the peak timescale.

In neutron star mergers, radioactive decay energy is released as a power law $\dot{q}(t) \propto t^{\alpha}$, where $\alpha = -1.1$ to -1.3, similar to that in the terrestrial radioactive waste (Metzger et al., 2010). A part of this energy, say $\epsilon_{\rm dep}$ fraction of it (defined as the thermalization factor), is deposited as thermal energy in the ejecta. Hence, the deposition luminosity is $L_{\rm dep} = \epsilon_{\rm dep} M_{\rm ej} \dot{q}(t)$.

Deriving the thermalization factor $\epsilon_{\rm dep}$ requires the detailed calculation of the microphysical parameters (e.g., the cross-section for Compton scattering and photo-ionization, Barnes et al., 2016). Nonetheless, a ballpark estimation of $\epsilon_{\rm dep}$ can be done as follows. In neutron star mergers, most radioactive decay energy is released via β-decay ($\sim 90\%$). Out of the total energy released via β-decay, $\sim 25\%$ is lost via neutrinos. A fraction of the remaining 75% of the energy, which is carried by the β-particles and the γ-rays, is deposited in the ejecta. Hence, we can assume the $\sim 50\%$ of the total radioactive energy is deposited in the ejecta, i.e., $\epsilon_{\rm dep} \sim 0.5$.

Using the heating rate from Metzger et al. (2010) and $\epsilon_{\rm dep} = 0.5$, we can determine the peak luminosity:

$$L_{\rm peak} = 1.3 \times 10^{40}\,{\rm erg\,s^{-1}}\left(\frac{M_{\rm ej}}{0.01{\rm M}_\odot}\right)^{0.35}\left(\frac{v}{0.1{\rm c}}\right)^{0.65}\left(\frac{\kappa}{10\,{\rm cm^2\,g^{-1}}}\right)^{-0.6}. \quad (1.4)$$

Figure 1.6 (top panel) shows the model light curve for a GW170817-like kilonova. The light curve for a type Ia supernova is also shown for comparison. It is apparent that the shape of the light curve in both cases are determined by the diffusion of photons. However, the peak luminosity of kilonova is fainter ($\sim$ a few magnitudes) in comparison to type Ia supernova. Moreover, the peak timescale for kilonova is much shorter ($\sim$ a week) than the type Ia supernova ($\sim$ a few weeks) The differences appear mainly due to the differences in the ejecta properties such as the total mass, velocity, and the abundance in the ejecta.

Note that both the peak timescale and luminosity for such transients depend on the opacity of the ejecta. For supernova, the main contribution to the opacity is coming from the iron group elements, whereas for kilonova, the dominant contributors to the opacity are the r-process elements. This fact significantly changes the opacity between the two transients. We discuss this in detail in Chapter 2.

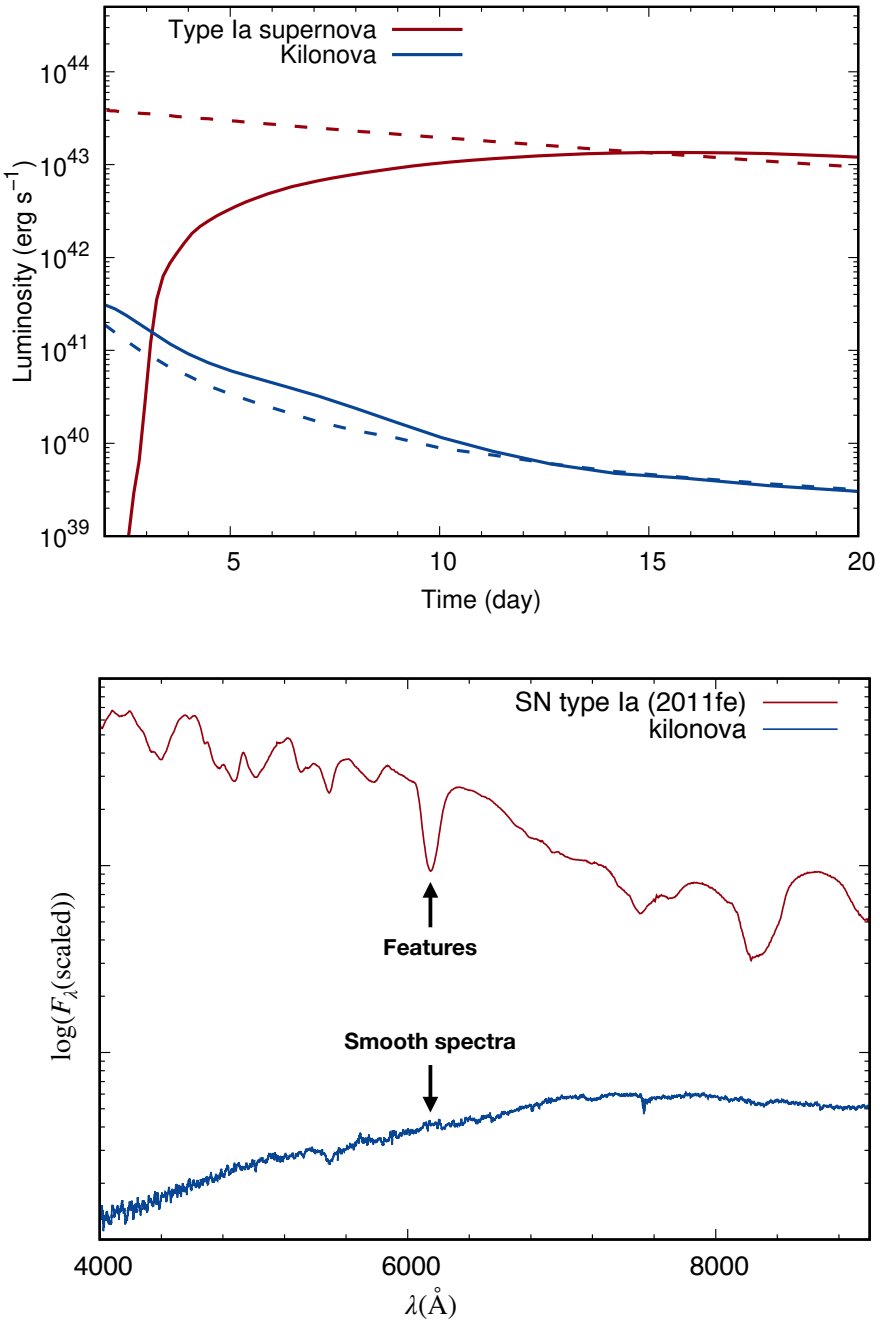

Figure 1.6: **Top:** Light curves for a GW170817-like kilonova assuming through the radioactive decay of r-process elements (blue curve, the light r-process elemental abundance, i.e., $Z = 20 - 56$, Banerjee et al., 2020) and for a type Ia supernova assuming ^{56}Ni decay (red curve, Nomoto et al., 1984). The dashed curves show the deposited luminosity. **Bottom:** Spectra for the type Ia SN2011fe at 7.23 days after the peak light (red curve, Pereira et al., 2013; Yaron & Gal-Yam, 2012) and for the kilonova GW170817 at 3.41 day after the merger or $\sim$ 2 days after the blue band maxima (blue curve, Smartt et al., 2017; Pian et al., 2017).

1.3.2 Spectra

The spectra of the kilonova evolve from UV to optical to NIR in the timescale of about a week. Moreover, the spectra is essentially featureless (blue curve in the bottom panel of Figure 1.6). The fast-evolving featureless spectra are used to differentiate the kilonova from other transients like supernova (red curve in the bottom panel of Figure 1.6).

The spectra in the supernova and kilonova can be understood from the radiative transfer properties in the expanding medium. Here the ejecta are moving with a high velocity and a high-velocity gradient, hence the lines are Doppler shifted, and the line blending occurs. This produces the continuum-like spectra. In supernova, the ejecta velocity and the corresponding degree of line blending are lower than that in the kilonova. Hence, some features are observable in supernova spectra.

The featurelessness of kilonova spectra is its distinguishing signature. At the same time, it becomes challenging to decode the individual heavy elements from such highly blended spectra. In fact, detection of only a few elements has been possible from kilonova spectra of GW170817 (e.g., Watson et al., 2019; Domoto et al., 2021; Perego et al., 2022).

1.3.3 Diversity of kilonovae

In the case of supernova, the diversity in the spectra is observed corresponding to the diversity in the progenitor and the explosion scenarios. The similar diversity for kilonova spectra is not well-understood since the sample of kilonova spectra is only one (at the time of writing the thesis, 2022). Even when the sample increases, it might be difficult to have a clear classification of kilonova on basis of spectra (unlike that in the supernova) since the spectra are featureless.

The kilonova diversity is mainly theoretically discussed based on the color and the timescale. Such diversity is predicted to exist because of the differences in the ejecta properties as obtained in the numerical relativity simulations (see Shibata & Hotokezaka, 2019, for a recent review). Hence, to discuss the diversity, we first need to understand the ejecta properties in neutron star mergers.

In neutron star merger, mass is ejected via several different channels,

1. **Dynamical ejecta:** A part of the mass is unbound ($10^{-4}\,M_\odot - 10^{-2}\,M_\odot$) within several ms after merger. This is mainly due to the tidal disruption or due to the compression induced shock heating in the collision surface (e.g., Bauswein et al., 2013; Hotokezaka et al., 2013a; Sekiguchi et al., 2015, 2016; Radice et al., 2016). This fast moving ($v_{\rm ej} \sim 0.1{\rm c} - 0.3{\rm c}$) ejecta component is called the dynamical ejecta. Based on which mechanism leads to the mass ejection (tidal or shock heating), the ejecta geometry, i.e., the distribution in the tidal plane or polar direction and the electron fraction vary (see red and cyan ejecta in Figure 1.7, which shows the results from the general relativistic hydrodynamic simulation from Fujibayashi et al., 2022).

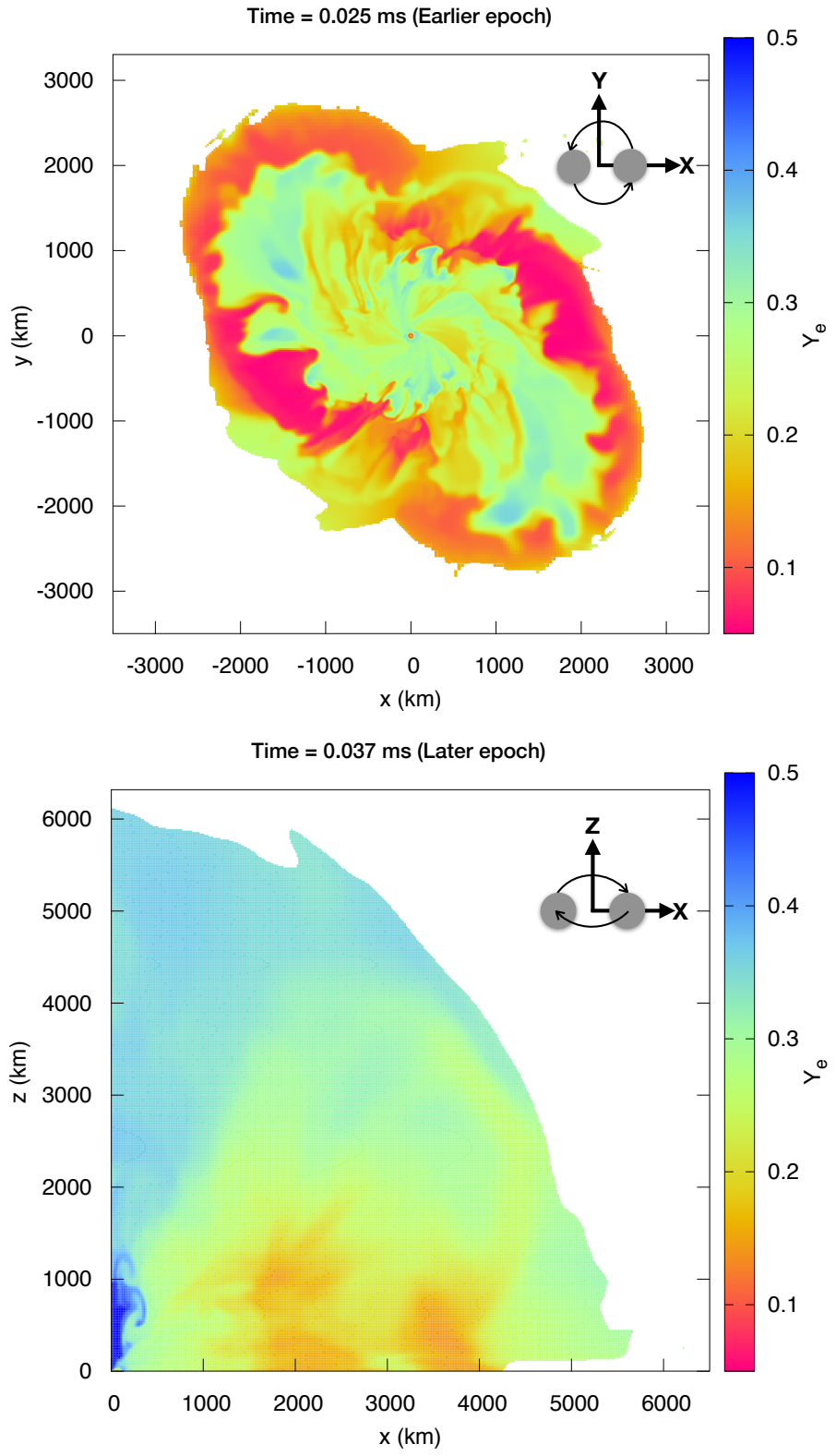

Figure 1.7: Snapshots for equal-mass neutron star merger leaving a hyper-massive neutron star for EoS SFHo135-135 (lifetime before collapsing to BH, $t_{\rm collapse} \sim 13$ ms, Fujibayashi et al., 2022) at $t = 0.025$ s in X-Y plane (top) and $t = 0.037$ s in X-Z plane. The data are obtained from private communication with Sho Fujibayashi.

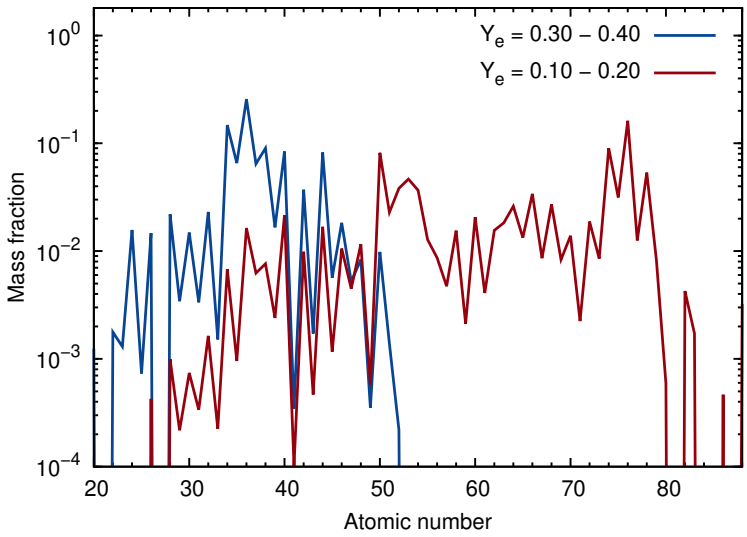

Figure 1.8: The abundance pattern for different electron fraction $Y_e = 0.30 - 0.40$ (blue curve) and $Y_e = 0.10 - 0.20$ (red curve). The data are from Wanajo et al. (2014).

2. **Disk wind ejecta:** Another channel of the mass ejection is from the disk formed around the central remnant. The mass of $\sim 10^{-2}\,M_\odot - 10^{-1}\,M_\odot$ is ejected due to the thermal ν_e heating and (mostly) viscous turbulent heating on a timescale of seconds. This relatively slow-moving ($v_{ej} \sim 0.1c - 0.2c$) ejecta component is called disk wind ejecta (the blue-green ejecta component in Figure 1.7, Fujibayashi et al., 2022, also see Dessart et al., 2009; Metzger & Fernández, 2014; Perego et al., 2014; Just et al., 2015; Siegel & Metzger, 2017; Lippuner et al., 2017; Shibata et al., 2017; Fujibayashi et al., 2018; Just et al., 2022; Fujibayashi et al., 2022).

Elemental abundances vary among different ejecta components. The tidal dynamical ejecta are always neutron rich, i.e., the electron fraction is low, $Y_e \sim 0.1$ (Figure 1.7, Fujibayashi et al., 2022, also see Goriely et al., 2011; Korobkin et al., 2012; Bauswein et al., 2013). On the other hand, the polar dynamical and the disk wind ejecta might have a wider range of $Y_e = 0.1 - 0.4$ (Goriely et al., 2015; Sekiguchi et al., 2015, 2016; Martin et al., 2018; Radice et al., 2018; Perego et al., 2014; Metzger & Fernández, 2014; Lippuner et al., 2017; Siegel & Metzger, 2017; Fujibayashi et al., 2018; Fernández et al., 2019).

In case of low $Y_e < 0.25$, the heaviest elements including lanthanides ($Z = 57 - 71$, see gray patch in Figure 1.1) are synthesized (see the red curve in Figure 1.8, Bauswein et al., 2013; Wanajo et al., 2014; Just et al., 2015; Sekiguchi et al., 2015; Kullmann et al., 2022; Just et al., 2022). Lanthanides are the f-shell complex elements which increase the opacity of the ejecta dramatically, shifting the peak of the light curve to the longer wavelengths (red and NIR) on a timescale of several days to a week (Barnes & Kasen, 2013; Tanaka & Hotokezaka, 2013). Such a kilonova is called the **red kilonova**.

On the other hand, if $Y_e > 0.25$, only light r-process elements are produced (see blue curve in Figure 1.8). In such case, blue emissions from the kilonova can be

observed at an early time ($\sim$ few hours to a few days). This is called the **blue kilonova** (see Figure 1.9 for an illustration).

The blue kilonova is observed if the viweing angle is near to the pole, whereas the red kilonova is always observed. This angle dependence can be understood from our discussion on the ejecta production channels. It is clear that the lanthanide-rich ejecta are mainly distributed in the tidal direction, whereas the lanthanide-free ejecta are distributed more isotropically or near to the pole (Figure 1.7, Fujibayashi et al., 2022). Such a distribution of the compositions introduces a viewing angle dependence in kilonova (Figure 1.9).

To understand the scenario, let us assume a merger where the polar dynamical ejecta and the disk wind ejecta are lanthanide free (same model as shown in Figure 1.7, Fujibayashi et al., 2022). Then if the viewing angle is near to the tidal plane, the blue emission might get completely blocked by the lanthanide-rich tidal dynamical ejecta and only the late time NIR signal will be observed. On the other hand, if the viewing angle is near to the pole, an early ($t < 1$ day) blue kilonova might be observed (see Figure 1.9). Note that the late NIR signal will be observed in this case as well.

Kilonova diversity is expected to be observed depending on the ejecta (or merger) properties and the viewing angle. Observing the NIR signal at a late time is the universal signature of all the kilonovae. However, whether a early blue kilonova is detected depeands on several factors, such as the observing angle and the ejecta component distribution.

Note that the early blue signal might be affected by several other mechanisms. For example, the interaction of the relativistic jet with the surrounding ejecta (Nativi et al., 2021) and the density structure modification, the emission powered by β-decays of free neutrons (Metzger et al., 2015; Gottlieb & Loeb, 2020), or by a long-lived central engine (Metzger et al., 2008; Yu et al., 2013; Metzger & Fernández, 2014; Matsumoto et al., 2018; Metzger et al., 2018; Li et al., 2018; Wollaeger et al., 2019). Hence, presence of such alternative heating sources can affect the onset and the magnitude of the early signal, which can potentially introduce variants of blue kilonova.

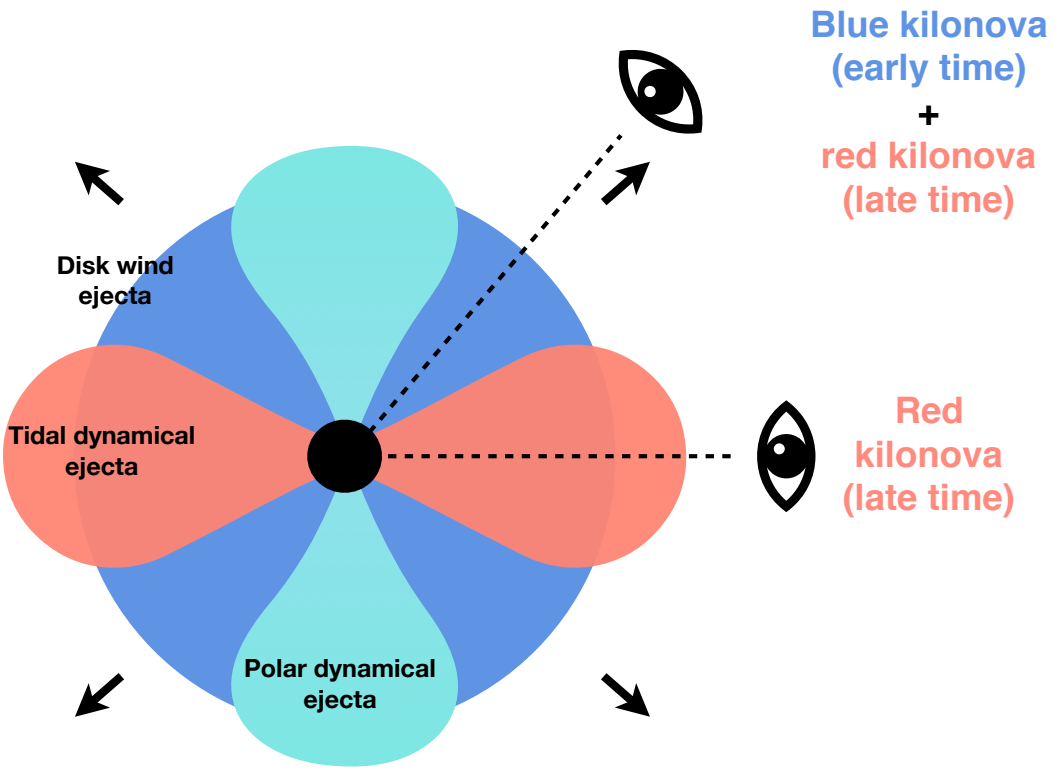

Figure 1.9: Schematic for the ejecta distribution for a neutron star merger motivated from the numerical simulations, see Figure 1.7. The lanthanides are distributed mainly in the tidal plane, and the polar dynamical and the disk wind ejecta are lanthanide-free. The distribusion of the abundances introduces angular dependence in the light curves. For example, the observers from the polar direction will observe the early blue kilonova alongwith the late red kilonova, whereas the observers in the tidal direction will only observe the red kilonova.

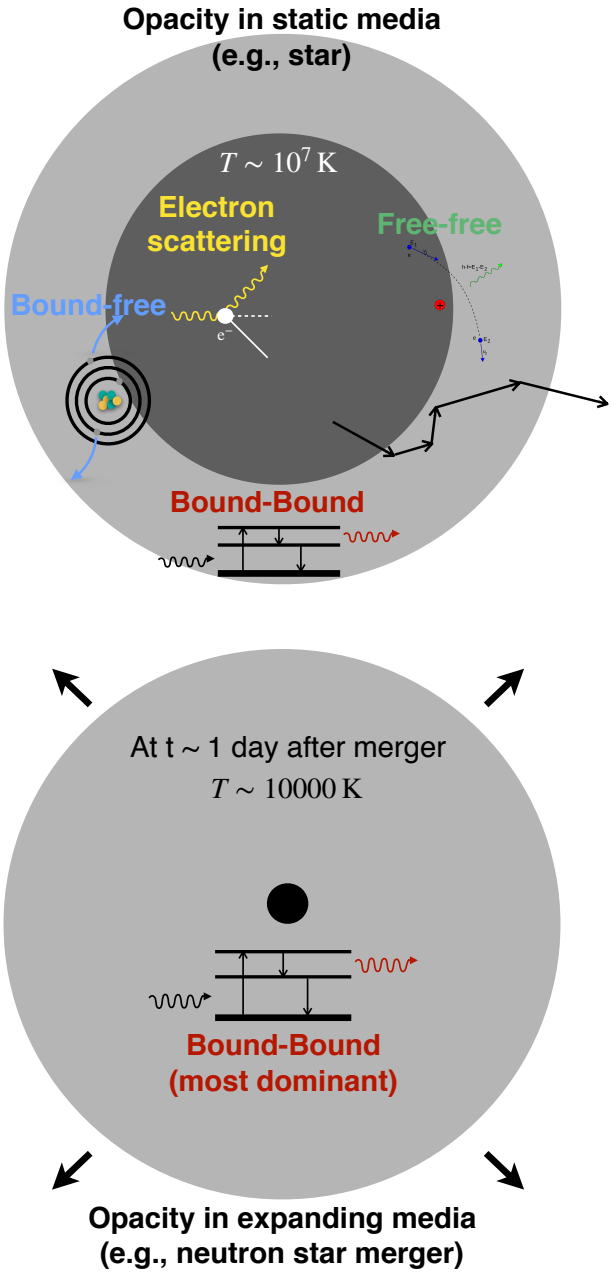

Figure 1.10: The sources of opacity in the stars (top) and in the expanding ejecta such as that in the supernova or in the neutron star mergers (bottom).

1.4 Aim and outline of the thesis

The origin of r-process heavy elements has puzzled astronomers for decades. The detection of the kilonovae from the neutron star merger has established the neutron star mergers to be the confirmed sites for the production of r-process nucleosynthesis. However, many questions are still unclear, for example:

- Can neutron star mergers reproduce solar abundance pattern?
  Are neutron star mergers the only source of heavy r-process elements?

This work is motivated to seek the answers to the above questions to understand *the origin of heavy elements*.

The abundance pattern in the neutron star merger ejecta leaves the signature on the light curve of kilonova and it is possible to study the abundance pattern by studying the kilonova light curve. Note that kilonova light curve from early to late time provides the information of outer to inner ejecta since the photons start to escape from the outermost layer of the ejecta. Therefore, it is important to understand the entire light curve for kilonova. However, the early kilonova (at $t < 1$ day) is not well understood (Arcavi, 2018), which thwarts us to extract the abundance information in the outer layer from the existing (kilonova associated with GW170817) and the near-future observations.

One of the biggest uncertainties in modelling the kilonova light curves comes from the opacity of the r-process elements, since the opacity determines the shape of the kilonova light curves (Equation (1.3) and Equation (1.4)). Therefore, the realistic light curve of kilonova requires the detailed opacity for the r-process elements.

Opacity provides the extent of the photon-matter interaction. The interaction can be in the form of the electron scattering, free-free, bound-free (or photo-ionization), and bound-bound transitions. Different mechanism can be dominant depending on the different environments. For example, inside a star, the core temperature is high ($T \sim 10^7$ K for a main sequence star) and the plasma in the core is completely ionized. Here the dominating process contributing to the stellar opacity is the electron scattering. On the other hand, the layers beyond stellar photosphere are relatively colder ($T \sim 10^4$ K for an A-type star) and the atoms are partially ionized, causing the bound-bound transitions dominating the photon transfer in stellar atmosphere (see Figure 1.10).

In supernovae or in the neutron star mergers, the dominant source of opacity is coming from the bound-bound opacity transitions (Figure 1.10). This is because in expanding media the temperature keeps on decreasing with time due to the adiabatic loss. The temperature in the neutron star mergers at about $t \sim 1$ day is $T \sim 10^4$ K, similar to the stellar atmosphere. Hence, the calculation of opacity in supernova or kilonova involves calculating the bound-bound opacity.

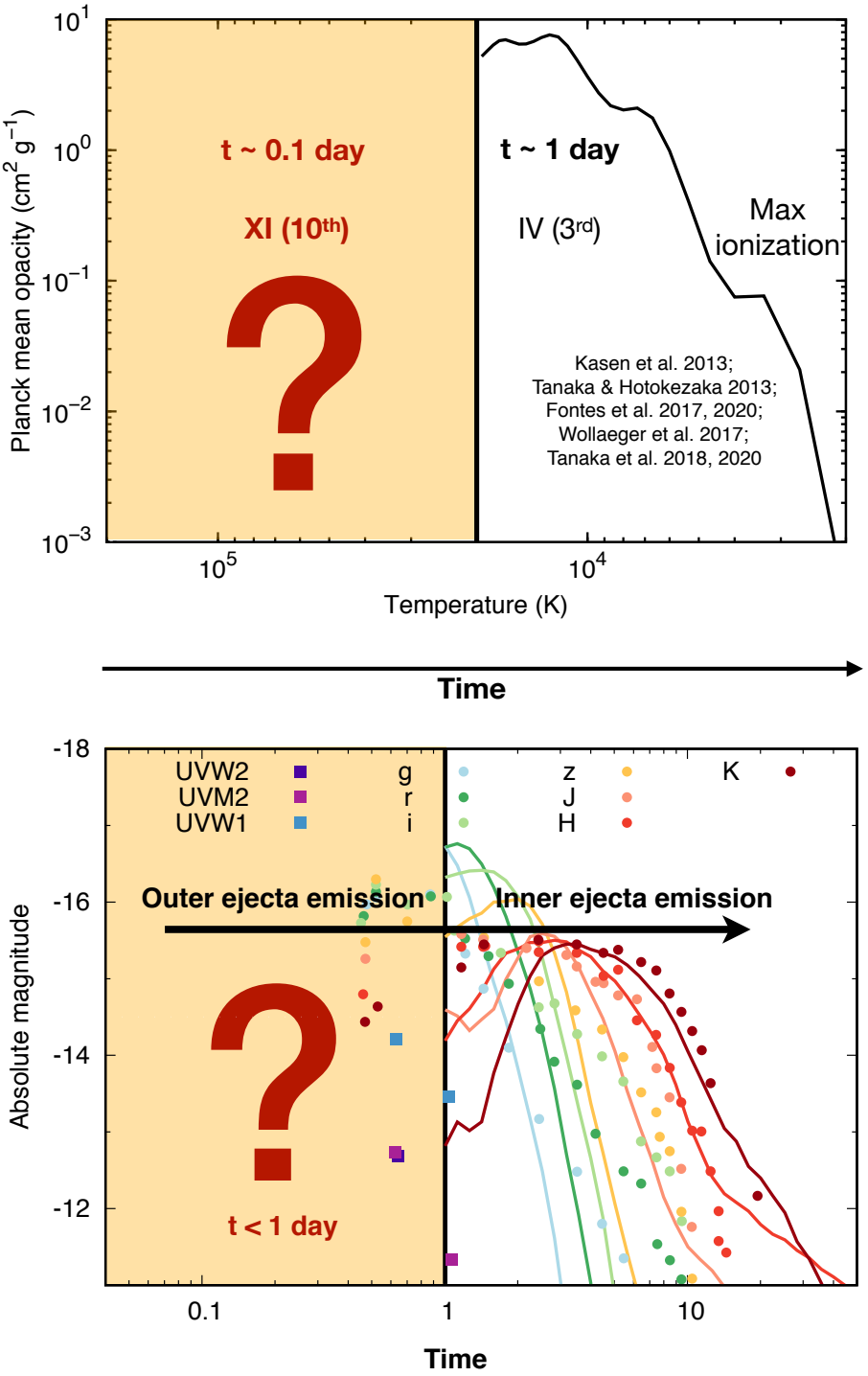

Figure 1.11: The status of the opacity (top) and light curve (bottom) calculations for kilonova from neutron star mergers (as of 2020).

Bound-bound opacity requires atomic data, for example, the energy levels and the transition information. These atomic data were largely unavailable for the r-process elements in the ejecta condition suitable for early time. This is because a few hours after the merger, the ejecta are still hot ($T \sim 10^5$ K), with r-process elements in the ejecta are highly ionized (maximum up to tenth or XI in spectroscopic notation, hereafter used in the thesis). Lack of such atomic data has been the bottleneck in determining the kilonova starting from an early time (Figure 1.11).

In the thesis, our aim is to provide the early kilonova light curve. Towards this purpose, we construct the detailed atomic opacity for the highly ionized (up to XI) r-process elements ($Z = 20 - 88$) in Chapter 2. Using the new atomic opacity, we determine the realistic light curve for kilonova starting from an early time ($t \sim$ a few hours) in Chapter 3. We discuss the application of our results to the early time data of kilonova associated with GW170817, as well as the future prospects in Chapter 4. Finally we provide concluding remarks in Chapter 5.

Our work will lead us to understanding the abundance pattern in the neutron star merger ejecta starting from the outermost layer together with the future observation. This, in turn, will contribute to progress towards the open questions such as whether the solar abundance pattern is reproduced in neutron star mergers. This will lead us towards *the origin of the heavy elements* (see Figure 1.12).

Our discussion and results in subsequent chapters are based on:

1. **Simulations of Early Kilonova Emission from Neutron Star Mergers**

   Banerjee S., Tanaka M., Kawaguchi K., Kato D., Gaigalas G., 2020, ApJ, 901, 29, doi : 10.3847/1538 − 4357/abae61.

2. **Opacity of the highly ionized lanthanides and the effect on the early kilonova**

   Banerjee S., Tanaka M., Kato D., Gaigalas G., Kawaguchi K., Domoto N., 2022, ApJ, in press.

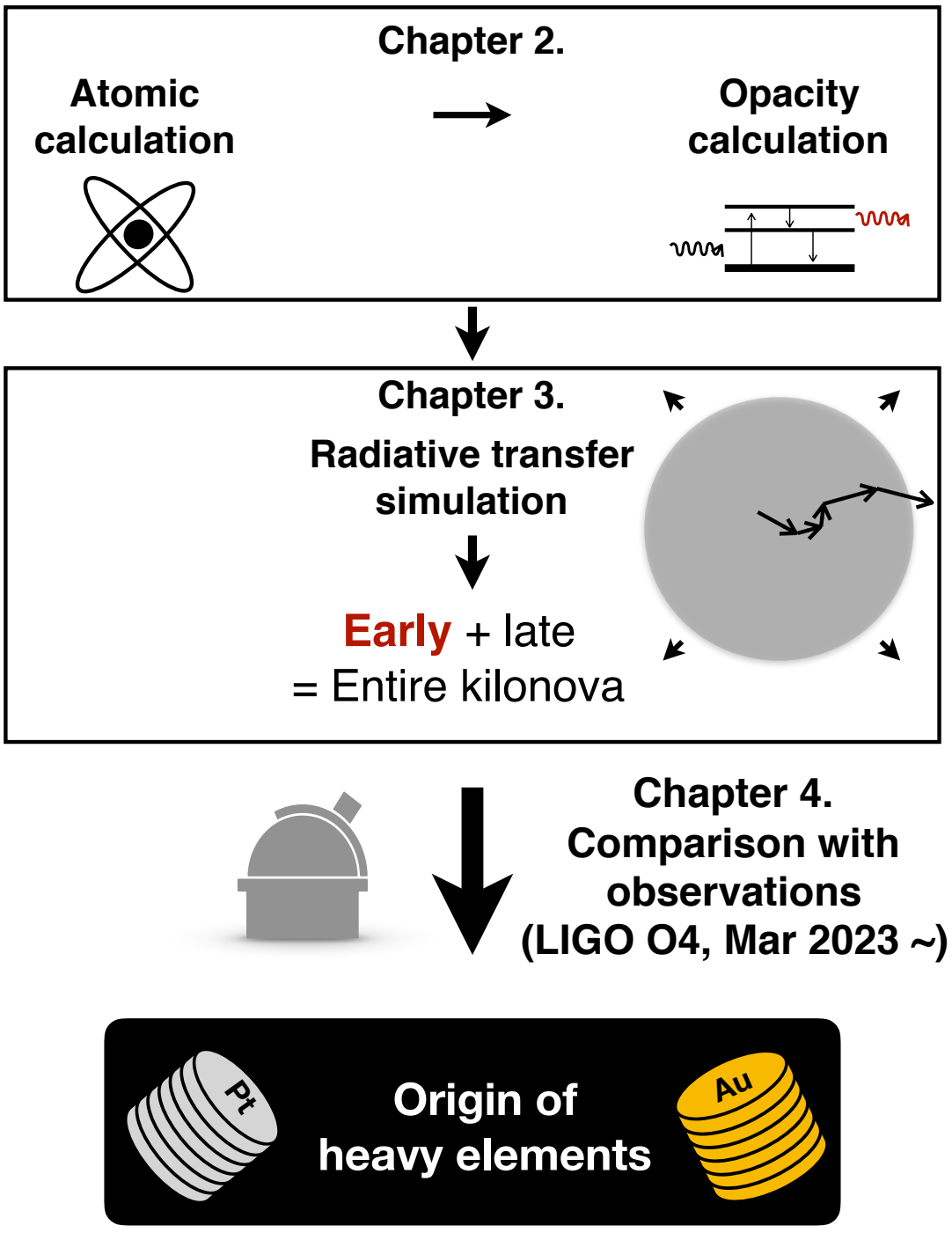

Figure 1.12: The chapter overview in the thesis.

Chapter 2

Opacity in neutron star mergers

2.1 Overview

In the neutron star mergers, the opacity of the ejecta is a key factor to determine the light curve. A change in the opacity by the factor of 10 changes the timescale by the same factor as that occurs by changing the ejecta mass by a factor of ~ 10 (Equation (1.3)). Simialr discussion can also be made for $L_{\rm peak}$ Equation (1.4)). Hence, correct opacity estimation is necessary for kilonova light curves.

In neutron star mergers, the main contribution to the opacity comes from the bound-bound transitions, calculation of which requires atomic calculation for the r-process elements (Chapter 1). In early 2000, no atomic data for the r-process elements were available and the kilonova calculations were performed by using the iron opacities (e.g., Metzger et al., 2010).

The first detailed calculation of atomic opacity for the r-process elements is performed by Kasen et al. (2013); Tanaka & Hotokezaka (2013). They find that the opacities for the r-process elements are much higher than the iron opacities. This is especially prominent if the open f-shell elements, lanthanides, are present in the ejecta. Getting motivated by the result, several groups have performed the opacity calculation for kilonova afterwards. In fact, Tanaka et al. (2020) derive the atomic opacity for all r-process elements ($Z = 31 - 88$). However, the maximum ionization considered in these works is IV, which is a reasonable assumption only for the condition in the neutron star merger ejecta around $t \geq 1$ day. Hence, none of these works are suitable for the calculation of the early kilonova,

We perform the first atomic opacity calculation for the highly ionized (up to XI) r-process elements ($Z = 20 - 88$), suitable for describing the ejecta conditions as early as $\sim$ hours after the neutron star merger.

2.2 Opacity components

Opacity provides the extent of photon-matter interaction in a medium and can be defined as the absorption cross-section per unit mass (also see Section 3.1.1). The photon-matter interaction can happen via several processes, such as, electron scattering, free-free, bound-free (or photo-ionization), and bound-bound transitions. Although the previous works suitable for the late time kilonova calculation (e.g.,

Kasen et al., 2013) show that the most significant contribution to opacity comes from the bound-bound transitions, we re-evaluate the contribution from individual physical processes since our work focuses on an early phase.

Electron scattering opacity

When the electro-magnetic wave passes through a medium with free electrons, it oscillates the electron (similar to a classical dipole), which causes the emission of a radiation in other direction. This is the electron scattering, which makes an important source of the opacity, specially in case of the highly ionized plasma. Such opacity can be measured for a single electron as the Thompson cross-section ($\sigma_{\rm Th} = 6.652 \times 10^{-25}\,{\rm cm}^2$). For a media with the electron density $n_{\rm e}$, the electron scattering opacity ($\kappa^{\rm es}$) is:

$$\kappa^{\rm es} = \frac{n_{\rm e}\sigma_{\rm Th}}{\rho}. \tag{2.1}$$

Note that the electron scattering opacity is wavelength independent and depends only on the electron density.

In the neutron star merger, a few hours after the merger, the ejecta temperature is high ($T \sim 10^5$ K) and the ejecta are highly ionized. Hence, the electron scattering might be an important source of the opacity at the early time. We estimate the electron scattering opacity by calculating the electron number density ($n_{\rm e}$) of the electrons in the single-element ejecta as:

$$n_{\rm e} = \frac{\rho}{A m_{\rm p}} j, \tag{2.2}$$

where A is the mass number, $m_{\rm p}$ is the mass of the proton, and j is the ionization degree of an element, e.g., $j = 5$ for ionization VI.

For the single-element ejecta with maximum ionization XI, i.e., for $j = 10$, the electron scattering opacity is estimated as $\kappa^{\rm es} = (3-10) \times 10^{-2}\,{\rm cm}^2\,{\rm g}^{-1}$ for elements $Z = 20 - 88$. The opacity is greater for the lower Z (and hence lower A) elements. For iron (Fe, $Z = 26$), the electron scattering opacity is $\sim 7 \times 10^{-2}\,{\rm cm}^2\,{\rm g}^{-1}$.

Free-free opacity

When an electron moves through the Coulomb field of an ion, it can emit or absorb a photon, known as free-free transition. The Free-free absorption can constitute another component of the total opacity ($\kappa^{\rm ff}_{i,j}(\lambda)$). For an element i at an ionization state j, this opacity component can be calculated as in Rybicki & Lightman (1986):

$$\kappa^{\rm ff}_{i,j}(\lambda) = \frac{4e^6\lambda^3}{3m_{\rm e}hc^4\rho}\left(\frac{2\pi}{3km_{\rm p}}\right)^{\frac{1}{2}} T_{\rm e}^{-\frac{1}{2}}(j-1)^2 n_{\rm e} n_{i,j} \times(1 - e^{-\frac{hc}{\lambda k T_{\rm e}}})\bar{g}_{\rm ff}, \tag{2.3}$$

where $T_{\rm e}$ is the electron temperature, and $\overline{g}_{\rm ff}$ is the velocity-averaged free-free Gaunt factor.

To estimate the free-free opacity in the neutron star merger, we calculate the ion density ($n_{i,j}$) following Tanaka & Hotokezaka (2013) as:

$$n_{i,j} = \frac{f_{i,j} X_i \rho}{A m_{\rm p}}. \tag{2.4}$$

Here X_i is the fractional abundance of the element i in the ejecta and $f_{i,j}$ is the fraction of the element i at an ionization state j. Velocity-averaged free-free Gaunt factor is taklen to be unity. To obtain an analytic estimate of the free-free opacity for ejecta with single-element abundance, the electron density is calculated from Equation (2.2), and the ion density is derived from Equation (2.4) by putting $f_{i,j} = 1$ and $X_i = 1$. We find that the free-free opacity of a single-element ejecta with temperature $T = 10^5$ K and density $\rho = 10^{-10}\,{\rm g\,cm^{-3}}$, is about $\kappa^{\rm ff}_{i,j} = (2-3) \times 10^{-4}\,{\rm cm^2\,g^{-1}}$ at a wavelength $\lambda = 1000$ Å for $Z = 20 - 88$. This opacity component is greater for lower Z elements. For Fe ($Z = 26$),$\kappa^{\rm ff}_{i,j} = 2.6 \times 10^{-4}\,{\rm cm^2\,g^{-1}}$. Therefore, even in the early time, the free-free opacity in the neutron star merger ejecta is relatively small.

Bound-free opacity

If the photon energy exceeds the ionization potential of the bound electrons, the photo-ionization or bound-free transition occurs, which contributes to the total opacity. Bound-free opacity is calculated as:

$$\kappa^{\rm bf}_{i,j}(\lambda) = \frac{n_{i,j}\sigma^{\rm bf}_{i,j}}{\rho}, \tag{2.5}$$

where $\sigma^{\rm bf}_{i,j}$ is the bound-free cross section for the the element i at the ionization state j. Calculation of such opacity requires careful consideration of atomic physics and hence is complicated.

In neutron star merger, the heavy r-process elements with atomic numbers $Z \geq 20$ are present. these elements can have a tenth ionization potential energy ~ 350 eV (Kramida et al., 2020), which corresponds to a wavelength of $\lambda \leq 50$ Å. The fraction of photon energy present at such a short wavelength range is $\sim 10^{-6}$, as predicted by the blackbody function at the temperature of $T = 10^5$ K. In fact, we find that the fraction never reaches beyond 10^{-4} by performing the same calculation for different ionization states of different elements in a temperature range of $T = 10^3 - 10^5$ K. Hence, we conclude that although the photo-ionization cross-section itself is high, the number of photons with energy greater than the ionization potential is negligible. Therefore, bound-free opacity does not make significant contribution to the total opacity.

Bound-bound opacity

One of the important sources of the opacity in the partially ionized plasma is the bound-bound transitions between the atomic energy levels. Bound-bound transitions can occur at particular line transition frequencies. However, in most cases, the atomic line profiles are broadened via processes such as thermal motion, which makes

the process occuring over a wavelength range rather than at a particular wavelength. Calculation of such opacity requires the information of the atomic bound states and the transition probabilities and hence is complicated.

Calculation of the bound-bound opacity for the neutron star merger ejecta requires atomic data for heavy r-process elements. Since complete atomic data calibrated with experiments are not available, we first perform the atomic structure calculations to construct the linelist (Section 2.3). Using these atomic data, we evaluate the bound-bound opacities for neutron star mergers.

2.3 Atomic Calculations

2.3.1 Theory of atomic calculation

We use the HULLAC (Hebrew University Lawrence Livermore Atomic Code, Bar-Shalom et al., 2001) for atomic calculations. First, we describe the essence of the theoretical background of our calculations. HULLAC uses fully relativistic orbitals to calculate the energy levels and radiative transition probabilities. The orbital functions are the solution to the single electron Dirac equation with a central field potential, which includes both the nuclear field and electron-electron interaction. The single electron four-component solution can be given by solving:

$$H(r)\phi_{nljm}(\mathbf{r}) = \epsilon_{nljm}\phi_{nljm}(\mathbf{r}). \tag{2.6}$$

The Hamiltonian in the above equation is constructed as a sum of the single particle kinetic Dirac hamiltonian and the effective central field potential as seen by the last electron. The Poisson equation is solved to get this central field potential for the electron charge distribution. The potential is considered to converge to $(Z-q)/r$ at $r=\infty$ for an element with atomic number Z and the number of the electrons q. The nuclear charge is considered to be a point one, i.e., $Z\delta(r)$. And the charge density distribution of the electrons is expressed as (Bar-Shalom et al., 2001):

$$\rho(r) = -4\pi r^2 q N[r^{l+1}\exp(-\alpha r/2)]^2, \tag{2.7}$$

where N is the normalization operator and α is the free parameter representing the average radii of the Slater type orbital. Here the free parameter α is obtained by the minimization of the first order configuration average energies of the selected configurations. We summarize the method described in Figure 2.1.

The N-electron zero-order solution or the configuration state function (CSF) is the anti-symmetrized products of the orbitals in the chosen coupling scheme (jj coupling for HULLAC). After constructing the zero-order wave function, the magnetic and the retardation effect of the interaction from the other electrons (Breit term) and the quantum electrodynamic (QED) energy correction are taken into account. Finally, the atomic wave function is constructed using the linear combination of the CSFs.

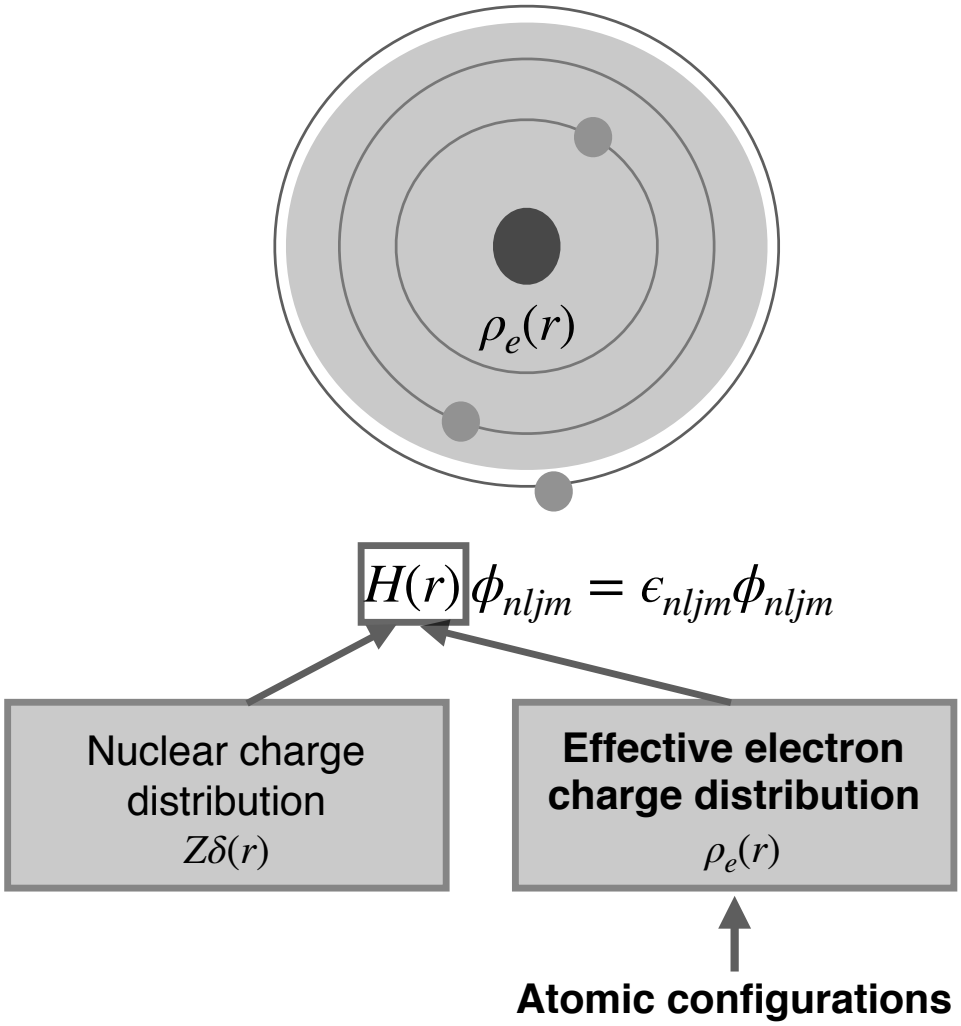

Figure 2.1: Calculation details for HULLAC which solves the single electron Dirac equation with a central potential to calculate the orbital functions. The central potential consists of both the nuclear field and electron-electron interaction. Atomic ground configurations are needed for atomic calculations including excited levels.

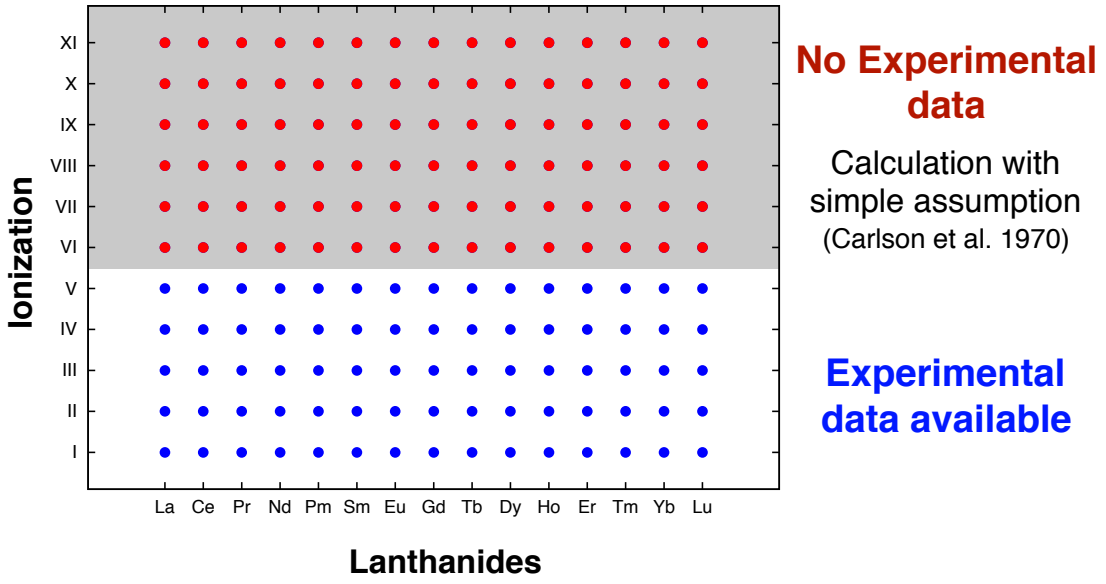

Figure 2.2: The summary of the experimental data available in Kramida et al. (2020) for lanthanides ionized up to XI.

2.3.2 Ground configurations

Atomic calculations including excited levels require information of ground configurations. The ground configuration for the low ionized r-process elements (I - IV) are relatively well established. Take for example, the lower ionized lanthanides, which can be firmly verified with the paramagnetic resonance and optical spectra for multi-valent ions in solids. For such free ions, the ground state configurations are experimentally verified from emission spectra in discharge experiments up to the ionization IV or V (see the latest compilation published by NIST, Martin et al., 1978). Hence, the previous atomic calculations including excited levels for low charge states use the ground configurations compiled in the NIST database (Kramida et al., 2020).

For highly ionized ions, the ground configurations are not well established for several elements. This problem is severe especially in the case of highly ionized lanthanides. NIST database (Kramida et al., 2020) provides the ground state configurations of all the lanthanide ions from the previous theoretical works (summarized in Table 2.1). However, all of these works are based on the different approximations or relatively simplified theoretical calculations (Carlson et al., 1970; Rodrigues et al., 2004; Sugar & Kaufman, 1975; Martin et al., 1978; hereafter we call all these references the NIST ASD).

It is important to understand the ground configurations for elements for accurate estimate of opacity. Since the lanthanide elements play important role to determine the bound-bound opacity, we calculate the ground configurations for the highly ionized (V $-$ XI) lanthanides from Pr ($Z = 59$) to Lu ($Z = 71$). For this purpose, we perform the systematic atomic structure calculations by solving fully relativistic equations for individual ions including electron correlation to construct the multi-electron wavefunction.

Table 2.1: Ground configurations as provided in the NIST ASD (Kramida et al., 2020)

Ion	La	Ce	Pr	Nd	Pm	Sm	Eu	Gd	Tb	Dy	Ho	Er	Tm	Yb	Lu
V[a,c]	$5p^5$	$5p^6$	$4f^15p^6$	$4f^25p^6$	$4f^35p^6$	$4f^45p^6$	$4f^55p^6$	$4f^65p^6$	$4f^75p^6$	$4f^85p^6$	$4f^95p^6$	$4f^{10}5p^6$	$4f^{11}5p^6$	$4f^{12}5p^6$	$4f^{13}5p^6$
VI[b]	$5p^4$	$5p^5$	$5p^6$	$4f^25p^5$	$4f^35p^5$	$4f^35p^6$	$4f^55p^5$	$4f^65p^5$	$4f^75p^5$	$4f^85p^5$	$4f^95p^5$	$4f^{10}5p^5$	$4f^{11}5p^5$	$4f^{12}5p^5$	$4f^{12}5p^6$
VII[b]	$5p^3$	$5p^4$	$4f^15p^4$	$4f^25p^4$	$4f^35p^4$	$4f^45p^4$	$4f^55p^4$	$4f^65p^4$	$4f^85p^3$	$4f^85p^4$	$4f^95p^4$	$4f^{10}5p^4$	$4f^{11}5p^4$	$4f^{12}5p^4$	$4f^{13}5p^4$
VIII[b]	$5p^2$	$5p^3$	$4f^15p^3$	$4f^25p^3$	$4f^35p^3$	$4f^45p^3$	$4f^55p^3$	$4f^65p^3$	$4f^75p^3$	$4f^95p^2$	$4f^95p^3$	$4f^{10}5p^3$	$4f^{11}5p^3$	$4f^{12}5p^3$	$4f^{13}5p^3$
IX[b]	$5p^1$	$5p^2$	$4f^15p^2$	$4f^25p^2$	$4f^35p^2$	$4f^45p^2$	$4f^55p^2$	$4f^65p^2$	$4f^75p^2$	$4f^85p^2$	$4f^{10}5p^1$	$4f^{10}5p^2$	$4f^{11}5p^2$	$4f^{12}5p^2$	$4f^{13}5p^2$
X[b]	$5s^2$	$5p^1$	$4f^2$	$4f^25p^1$	$4f^35p^1$	$4f^45p^1$	$4f^55p^1$	$4f^55p^2$	$4f^65p^2$	$4f^85p^1$	$4f^95p^1$	$4f^{10}5p^1$	$4f^{11}5p^1$	$4f^{12}5p^1$	$4f^{12}5p^2$
XI[b,d]	$5s^1$	$5s^2$	$5p^1$	$4f^2$	$4f^35s^2$	$4f^45s^2$	$4f^55s^2$	$4f^55p^1$	$4f^65p^1$	$4f^85s^2$	$4f^95s^2$	$4f^{10}5s^2$	$4f^{11}5s^2$	$4f^{12}5s^2$	$4f^{12}5p^1$

[a] Sugar (1975)
[b] Carlson et al. (1970)
[c] Martin et al. (1978)
[d] Rodrigues et al. (2004)

Table 2.2: Summary of ground configuration calculations for Gd ($Z = 64$) for ionization V − XI

Ionization	$\mathbf{5p^6}$	$\mathbf{5p^5}$	$\mathbf{5p^4}$	$\mathbf{5p^3}$	$\mathbf{5p^2}$	$\mathbf{5p^1}$
V	$\mathbf{4f^6\,5p^6}$	$4f^7\,5p^5$				
VI	$\mathbf{4f^5\,5p^6}$	$4f^6\,5p^5$				
VII	$4f^4\,5p^6$	$\mathbf{4f^5\,5p^5}$				
VIII		$4f^4\,5p^5$	$\mathbf{4f^5\,5p^4}$			
IX			$4f^4\,5p^4$	$\mathbf{4f^5\,5p^3}$		
X				$4f^4\,5p^3$	$\mathbf{4f^5\,5p^2}$	
XI					$4f^4\,5p^2$	$\mathbf{4f^5\,5p^1}$

Ground configurations are shown in bold for each ionization.

Table 2.3: The list of configurations used in different strategies for Gd ($Z = 64$) V

Cases	Potential felt by last electron	Minimization	Ground configuration
A	$4f^6\,5p^5$	$4f^6\,5p^6$	$4f^6\,5p^6$
B	$4f^5\,5p^6$	$--''--$	$4f^6\,5p^6$
C	$4f^7\,5p^4$	$4f^7\,5p^5$	$4f^6\,5p^6$
D	$4f^6\,5p^5$	$--''--$	$4f^6\,5p^6$

The energy levels are calculated for the configurations $4f^6\,5p^6$ and $4f^7\,5p^5$.

Table 2.4: The list of configurations used in different strategies for Gd ($Z = 64$) VII

Cases	Potential felt by last electron	Minimization	Ground configuration
A	$4f^4\,5p^5$	$4f^4\,5p^6$	$4f^4\,5p^6$
B	$4f^3\,5p^6$	$--''--$	$4f^4\,5p^6$
C	$4f^5\,5p^4$	$4f^5\,5p^5$	$4f^5\,5p^5$
D	$4f^4\,5p^5$	$--''--$	$4f^5\,5p^5$
A′	$4f^4\,5p^5$	$4f^4\,5p^6$ $4f^5\,5p^5$	$4f^5\,5p^5$
B′	$4f^3\,5p^6$	$--''--$	$4f^5\,5p^5$
C′	$4f^5\,5p^4$	$--''--$	$4f^5\,5p^5$

The energy levels are calculated for the configurations $4f^4\,5p^6$ and $4f^5\,5p^5$.

Note that we also perform calculations to find the ground configurations for the post-lanthanide elements and our results for the post-lanthanides have confirmed the ground configurations provided in NIST database (Kramida et al., 2020). Here we do not mention such results for elements other than lanthanides.

Strategy of calculation

We discuss the strategy we develop to evaluate the ground configurations of lanthanides, which are the complex ions with open $4f$ shells. We design our strategy based on the fact that for the highly ionized ($\geq$ V) lanthanides, the outermost electrons are in the $4f$ and $5p$ orbitals. Hence, we check whether the removal of $4f$- or $5p$- electron is necessary for the further ionization.

First, we construct several cases of the atomic calculations by (1) changing the electron distribution in $4f$ and $5p$ orbitals, and consequently changing the central potential; and by (2) using different configurations for energy minimization. For each case, we identify a CSF with the largest mixing coefficient for the lowest energy level. Then the configuration generating the CSF is taken to be the ground configuration. If a certain configuration gives the ground configuration for all the different cases, we regard it as the ground configuration for the particular ion.

Example calculation

We explain the strategy we devise with the help of examples. Let us consider the ground configuration calculation for the Gd ($Z = 64$). The configurations used are summarized in Table 2.2). First we focus on Gd V ion (Table 2.3). According to the NIST ASD, the ground configuration for Gd IV is $4f^7\,5p^6$, which is experimentally verified. We test whether the ground configuration of Gd V is also the same as provided in the NIST ASD ($4f^6\,5p^6$). We include two possible candidates for the ground configuration for Gd V: $4f^6\,5p^6$ (as in the NIST ASD) and $4f^7\,5p^5$, corresponding to the $4f$ and $5p$ electron removal from the ionization Gd IV. We calculate the energy levels for these two configurations.

As the total number of electrons in $4f$ and $5p$ orbitals is 12, the effective potential is constructed based on the distribution of 11 electrons by removing one electron. Hence, for the configuration $4f^6\,5p^6$, the potentials can be constructed based on either $4f^6\,5p^5$ or $4f^5\,5p^6$, after removal of one electron. Then we optimize the potential for $4f^6\,5p^6$. We denote these two cases as Case A and Case B in Table 2.3. Similarly, in the case of configuration $4f^7\,5p^5$, the central potential construction can be made either by $4f^7\,5p^4$ or $4f^6\,5p^5$, and optimized for $4f^7\,5p^5$. These are denoted as Case C and Case D. The atomic calculations with these four different cases show that the ground configuration always belongs to the configuration $4f^6\,5p^6$. Hence, we regard $4f^6\,5p^6$ as the ground configuration for Gd V.

We perform the similar calculations for the other ions of Gd (Table 2.2). We find that different ions of Gd show the convergence for the ground configurations for most case (shown in bold in Table 2.2). However, in few cases, such as Gd VII, the results of the four cases do not show convergence. In such a case, we perform another set of calculation employing both candidate configurations for the energy minimization to determine the potential (Cases A$'$, B$'$, and C$'$ in Table 2.4). If

the ground configurations converge in these cases (A′, B′, and C′), we assume that configuration as the ground one. In the case of Gd VII, $4f^5\,5p^5$ always gives the ground configuration in Cases A′, B′, and C′, and hence, it is regarded as the ground configuration.

The same strategy is applied to evaluate ground configurations of other highly ionized lanthanides from Pr ($Z = 59$) to Lu ($Z = 71$). As summarized in Table 2.5, almost all the ions reach convergence either after Cases A − D or Cases A′, B′, and C′. Only the exceptions are Er VIII and Lu VIII, where the ground configuration is not confirmed even after energy minimization with the two configurations (Cases A′, B′, and C′). For these cases, the ground configuration candidates of the next ion (Er IX and Lu IX) involve three configurations. For instance, the ground configuration for Er VIII is not converged between $4f^7\,5p^6$ and $4f^8\,5p^5$. Then, the possible configurations for Er IX are $4f^7\,5p^5$, $4f^6\,5p^6$ and $4f^8\,5p^4$, corresponding to the $4f$ or $5p$ electron removal from the two candidate configurations of Er VIII. We proceed calculations taking two configurations at a time. Finally, all the different cases converge to the ground configuration of $4f^8\,5p^4$. The ground configuration of Lu IX is calculated in a similar way. In this case, we also get the converged ground configuration ($4f^{11}\,5p^4$).

Results of ground configurations

Results of our calculations are summarized in Table 2.5. The configuration for La ($Z = 57$) and Ce ($Z = 58$) provided in the NIST ASD are also shown for the sake of completion. When the ground state configurations of the ions are different from those in the NIST ASD, they are shown in bold. The ions that require minimizing the energy with the two configurations to reach convergence (Cases A′, B′, and C′) are shown with an asterisk. We give two configurations in the two exceptional cases (Er VIII and Lu VIII), where the convergence is not reached even after the Cases A′, B′, and C′.

Comparison with NIST ASD

The ground configurations obtained from HULLAC are different from those in the NIST ASD for most of the ions (written in bold in Table 2.5). Our results show that $4f$ electron removal occurs for further ionization from the ionization V. For the ionization VI and VII, either $5p$ or $4f$ electron is removed depending on the elements. Beyond the ionization VIII, the higher ionization happens only by $5p$ electron removal. These results are in contrast with those in the NIST ASD (mainly Carlson et al. 1970), which shows the removal of $5p$ electron starts from ionization V. This trend is visualized in Figure 2.3, which shows the number of $5p$ electrons in the lanthanide ions.

For ionization V, the NIST ASD values are obtained from the works by Sugar (1975) and Martin & Sugar (1973). Sugar (1975) considers that the ground configuration of the ionization V of lanthanides coincides with the limit of the $4f^{N-1}\,ns$ (the Rydberg series), where N is the number of electrons in the IV ion, and n runs from $6 - \infty$. For Pr V, experimental data exist as reported in Martin & Sugar (1973). Our results agree well with these results for all the elements.

Table 2.5: The results of ground configuration obtained from the HULLAC calculation

Ion	La	Ce	Pr	Nd	Pm	Sm	Eu	Gd	Tb	Dy	Ho	Er	Tm	Yb	Lu
V	$5p^5$	$5p^6$	$4f^15p^6$	$4f^25p^6$	$4f^35p^6$	$4f^45p^6$	$4f^55p^6$	$4f^65p^6$	$4f^75p^6$	$4f^85p^6$	$4f^95p^6$	$4f^{10}5p^6$	$4f^{11}5p^6$	$4f^{12}5p^6$	$4f^{13}5p^6$
VI	$5p^4$	$5p^5$	$5p^6$	$\mathbf{4f^15p^6}$	$\mathbf{4f^25p^6}$	$4f^35p^6$	$\mathbf{4f^45p^6}$	$\mathbf{4f^55p^6}$	$\mathbf{4f^65p^6}$	$\mathbf{4f^75p^6}$	$\mathbf{4f^85p^6}$	$\mathbf{4f^95p^6}$	$\mathbf{4f^{10}5p^6}$	$\mathbf{4f^{11}5p^6}$	$4f^{12}5p^6$
VII	$5p^3$	$5p^4$	$\mathbf{5p^5}$	$\mathbf{5p^6}$	$\mathbf{4f^25p^{5*}}$	$\mathbf{4f^35p^{5*}}$	$\mathbf{4f^45p^{5*}}$	$\mathbf{4f^55p^{5*}}$	$\mathbf{4f^65p^{5*}}$	$\mathbf{4f^75p^{5*}}$	$\mathbf{4f^75p^6}$	$\mathbf{4f^85p^6}$	$\mathbf{4f^95p^6}$	$\mathbf{4f^{10}5p^6}$	$\mathbf{4f^{11}5p^6}$
VIII	$5p^2$	$5p^3$	$\mathbf{5p^4}$	$\mathbf{4f^15p^{4*}}$	$\mathbf{4f^25p^{4*}}$	$\mathbf{4f^35p^4}$	$\mathbf{4f^45p^4}$	$\mathbf{4f^55p^4}$	$\mathbf{4f^65p^4}$	$\mathbf{4f^75p^4}$	$\mathbf{4f^75p^5}$	$\mathbf{4f^75p^6}$ $\mathbf{4f^85p^5}$	$\mathbf{4f^95p^{5*}}$	$\mathbf{4f^{10}5p^{5*}}$	$\mathbf{4f^{10}5p^6}$ $\mathbf{4f^{11}5p^5}$
IX	$5p^1$	$5p^2$	$\mathbf{5p^3}$	$\mathbf{4f^15p^3}$	$\mathbf{4f^25p^3}$	$\mathbf{4f^35p^3}$	$\mathbf{4f^45p^3}$	$\mathbf{4f^55p^3}$	$\mathbf{4f^65p^3}$	$\mathbf{4f^75p^3}$	$\mathbf{4f^75p^4}$	$\mathbf{4f^85p^{4*}}$	$\mathbf{4f^95p^4}$	$\mathbf{4f^{10}5p^4}$	$\mathbf{4f^{11}5p^{4*}}$
X	$5s^2$	$5p^1$	$\mathbf{5p^2}$	$\mathbf{4f^15p^2}$	$\mathbf{4f^25p^2}$	$\mathbf{4f^35p^2}$	$\mathbf{4f^45p^2}$	$4f^55p^2$	$4f^65p^2$	$\mathbf{4f^75p^2}$	$\mathbf{4f^75p^{3*}}$	$\mathbf{4f^85p^3}$	$\mathbf{4f^95p^3}$	$\mathbf{4f^{10}5p^3}$	$\mathbf{4f^{11}5p^3}$
XI	$5s^1$	$5s^2$	$5p^1$	$\mathbf{4f^15p^1}$	$\mathbf{4f^25p^1}$	$\mathbf{4f^35p^1}$	$\mathbf{4f^45p^1}$	$4f^55p^1$	$4f^65p^1$	$\mathbf{4f^75p^1}$	$\mathbf{4f^75p^2}$	$\mathbf{4f^85p^2}$	$\mathbf{4f^95p^2}$	$\mathbf{4f^{10}5p^2}$	$\mathbf{4f^{11}5p^2}$

The configurations written in bold are different from those in the NIST ASD.
The configurations with asterix require energy minimization with two configurations.

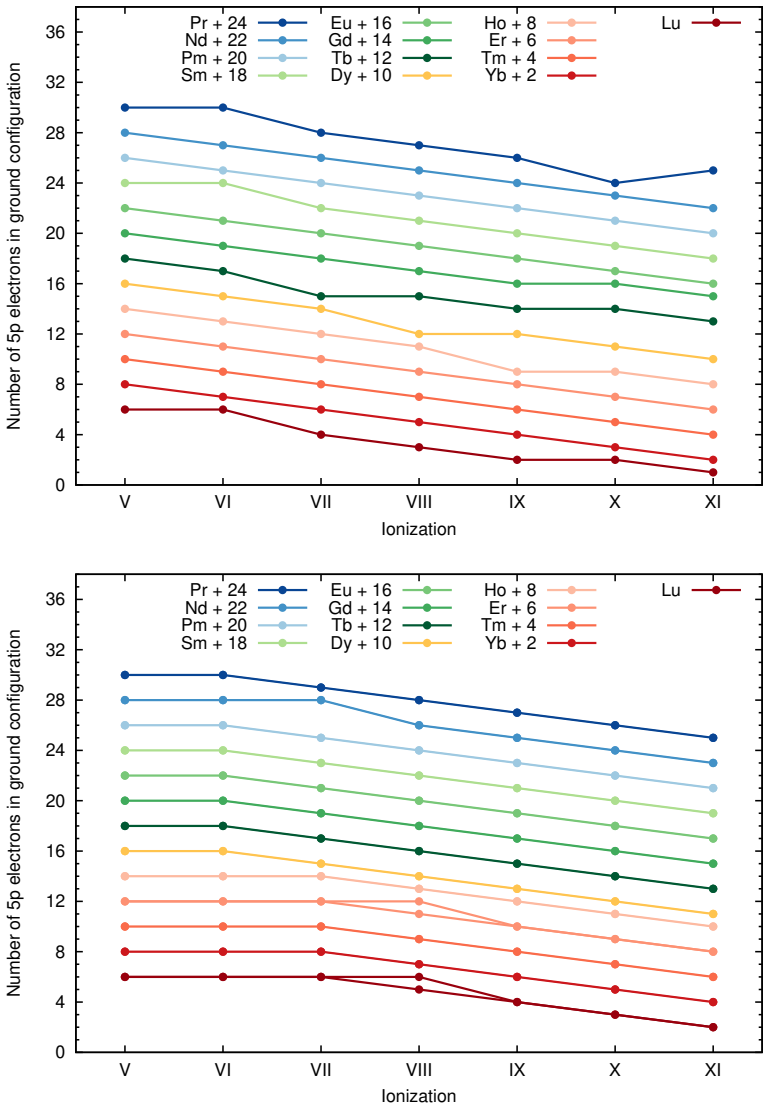

Figure 2.3: The number of $5p$ electrons as a function of ionization degree as provided in the NIST ASD (top) and HULLAC results (bottom).

For ionization VI and higher, our results are different from those in the NIST ASD, which are taken from the theoretical calculations by Carlson et al. (1970). Carlson et al. (1970) calculates the ionization potential for all elements from $Z = 2 - 103$ based on an approximate scheme. Their calculations are based on the principle that, for each ion, the most loosely bound electron is removed for further ionization and the eigen energy of the shell gives the ionization potential. Instead of performing the atomic calculation for each ion, the most loosely bound orbital is determined from the solution of the relativistic Hartree-Fock wavefunction for the neutral atoms. By this scheme, the ground configuration of the consecutive elements is determined. On the other hand, we calculate atomic energy levels for each ion with the HULLAC by solving the Dirac equation for an effective central field potential by taking electron-electron interaction into account. Hence, we choose to use the ground configurations obtained from the HULLAC instead of the NIST ASD.

Using the ground configurations together with the excited configurations, we perform the atomic calculation for the opacity. All the configurations used are provided in Table D.1. The ground configurations and all the configurations used for minimization are shown in bold.

2.3.3 Potential energy

In this section, we provide the potential energy derived from our calculation for the ionization V - XI (Figure 2.4). The potential energy is calculated as the difference of the ground energy level of two consecutive ions. The potential energy shows an increasing trend toward higher Z for a particular ionization degree. The data provided in NIST ASD are shown by the red dotted line for reference. The dependence with the atomic number is weak around ionization V and VI but gets stronger at higher ionization degrees (Figure 2.4).

The potential calulated from HULLAC and NIST ASD shows overall good match except that for the lanthanides. This is not surprising because the potential energy for highly ionized lanthanides provided in NIST ASD is mostly based on the approximated calculations by Carlson et al. 1970. These authors calculate the ionization potential taking the assumption that the ionization potential of different ions is the eigen energies of the consecutively least bound electrons in neutral atoms. Our work is based on detailed atomic calculations for each ion and thus provides more reliable results.

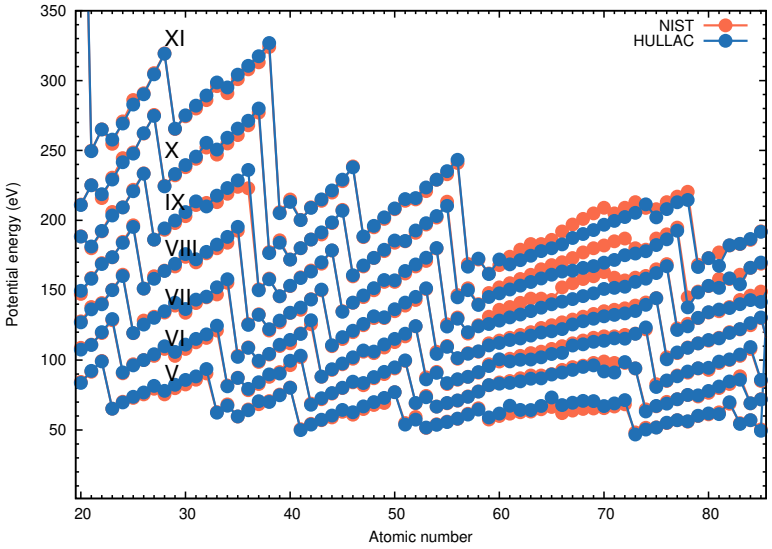

Figure 2.4: The potential energy obtained from the HULLAC calculations for ionization V - XI. The red dots show the data from the NIST ASD for reference.

2.3.4 Energy levels

We show the distribution of the energy levels as obtained from our atomic calculations for all the elements ($Z = 20 - 88$) in the Figure 2.5 to Figure 2.6 for different ionization. The color scale describes the density of the energy levels in the 0.2 eV energy bin. Since our main purpose is to calculate the bound-bound opacity, we show the energy levels only below the ionization threshold. Our calculation includes the elements from the different shells and hence, we discuss the energy level for different shell elements separately for clarity.

The main factors that determine the trend of energy levels for highly ionized ions are: half-closed shells have the highest complexity measure, and the increment in Z in a shell raises the energy distribution upwards (Tanaka et al., 2020). keeping this in mind, we will discuss the energy level trend for different elements.

f-shell elements

The f-shell elements, lanthanides, have the densest distribution of the energy levels among the r-process elements considered (Figure 2.5, Figure 2.6). Such behavior is seen over all the ionizations (e.g., for the low-ionized cases, see Tanaka et al., 2020). However, for higher ionization, the energy level density for lanthanides are much higher than that in the low ionized case.

For a particular ionization, the distribution of the energy levels varies depending on the elements. This is due to the difference in the number of f-electrons (Table D.1). For example, Eu IX has four f-electrons in the ground configuration ($4f^4\,5p^3$, Table D.1), whereas Nd IX has only one ($4f\,5p^3$, Table D.1). As a result, Eu IX shows a higher energy level density than Nd IX.

The energy distribution for lanthanides is the densest around the ionization of VII - IX. This is caused by the presence of the two open shells (f- and p-shell, see Table D.1) in highly ionized lanthanides.

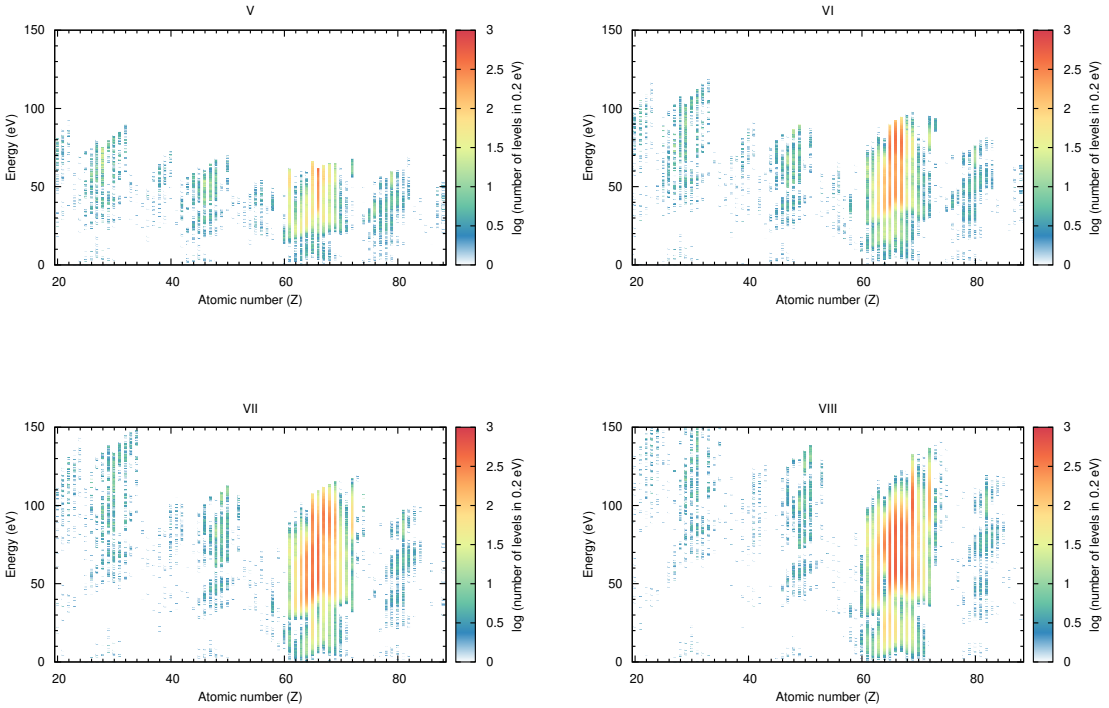

Figure 2.5: The distribution of the energy level for all elements below the ionization threshold. Different panels represent ionization from V - VIII.

d-shell elements

The *d*-shell elements show relatively low energy level density. This is different than the low ionized case, where the *d*-shell element have the most dense energy levels after *f*-shell elements (Tanaka et al., 2020). This is because at highly ionized state, *d*-shell elements resemble neutral *p*-shell elements, hence overall number density decreases. However, the situation is different in the *d*-shell elements Hf ($Z = 72$) and Ta ($Z = 73$) which show high energy density. This is because at high ionization, these elements resemble the lanthanide elements with open *f*-shell.

p- and *s*-shell elements

The *p*-shell elements show higher density in energy levels because they resemble elements with half-closed *d*-shells when highly ionized and *d*-shell electrons are removed. In fact, *p*-shell elements in the highly ionized state have the second highest energy level density after the *f*-shell elements (except for the *d*-group elements Hf and Ta). This behavior is different than the *p*-shell elements in low ionized case (see Tanaka et al., 2020).

The *s*-shell elements show low energy level density. This is because these elements resembles *p*-shell or almost filled *d*-shell elements when highly ionized. This result is the same as the lower ionized states, where the *s*-shell elements resembles the almost filled *p*-shell elements. In concusion, the *s*-shell elements show low energy level density at all ionization states.

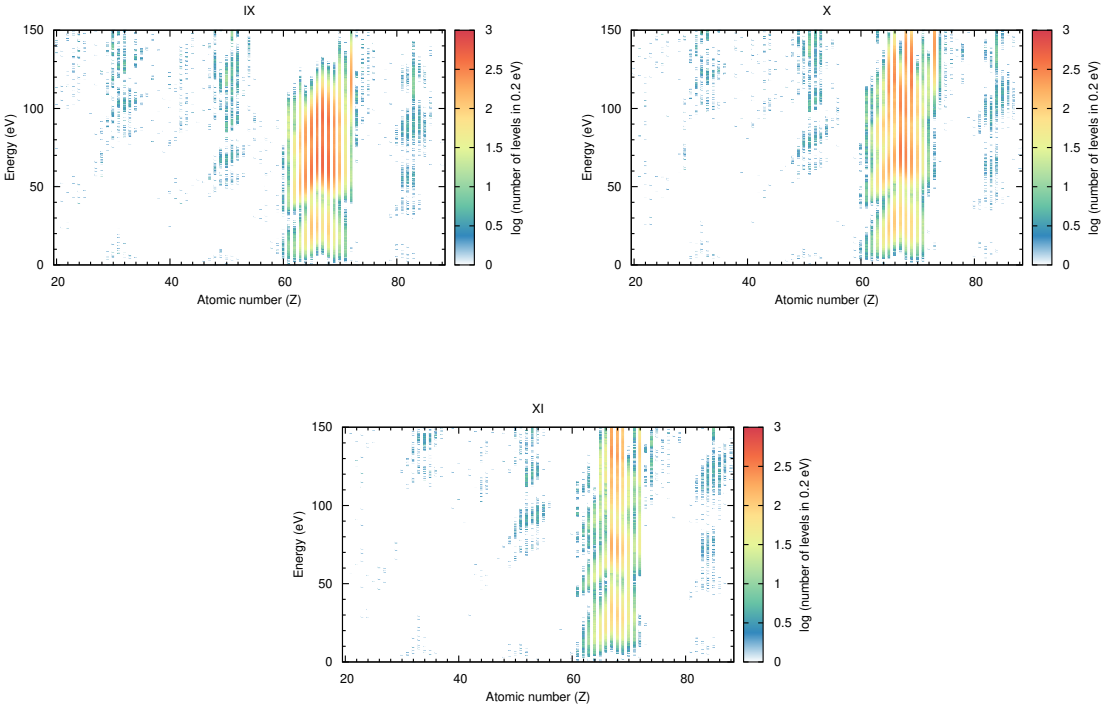

Figure 2.6: The distribution of the energy levels for all elements below the ionization threshold. Different panels represent ionization from IX - XI.

2.3.5 Transitions

The total number of transitions obtained from our atomic calculations for different elements in various ionization states (V - XI) is shown in Figure 2.7. The total number of transitions reflects the number density of the energy levels. The f-shell elements show the highest number of transitions ($N_{\rm tran} \sim 10^9$) with a peak around the ionization range $\sim$ VII - IX. For d-group elements, total number of transitions are low ($N_{\rm tran} \sim 10^4$), except that for Hf and Ta, where the transitions can be as high as the number of transitions in the first half of the lanthanides ($N_{\rm tran} \sim 10^7$). This is due to the fact that at highly ionized condition, these elements resemble the neutral lanthanides. The p-shell elements show relatively high number of transitions ($N \sim 10^6$). The number of transitions in s-shell elements are low ($N_{\rm tran} \sim 10^2 - 10^4$).

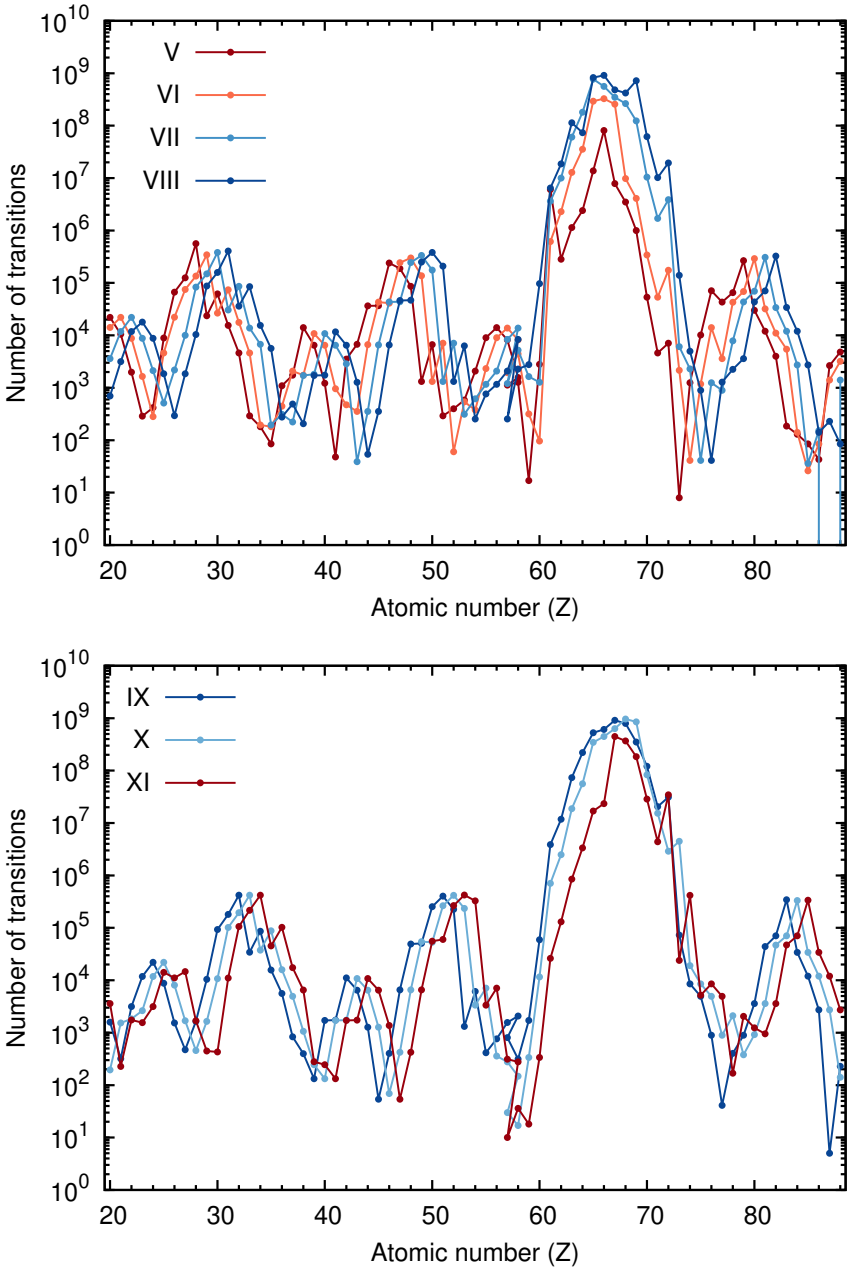

Figure 2.7: The total number of transitions for ionization V - VIII (top) and IX - XI (bottom) as calculated by HULLAC.

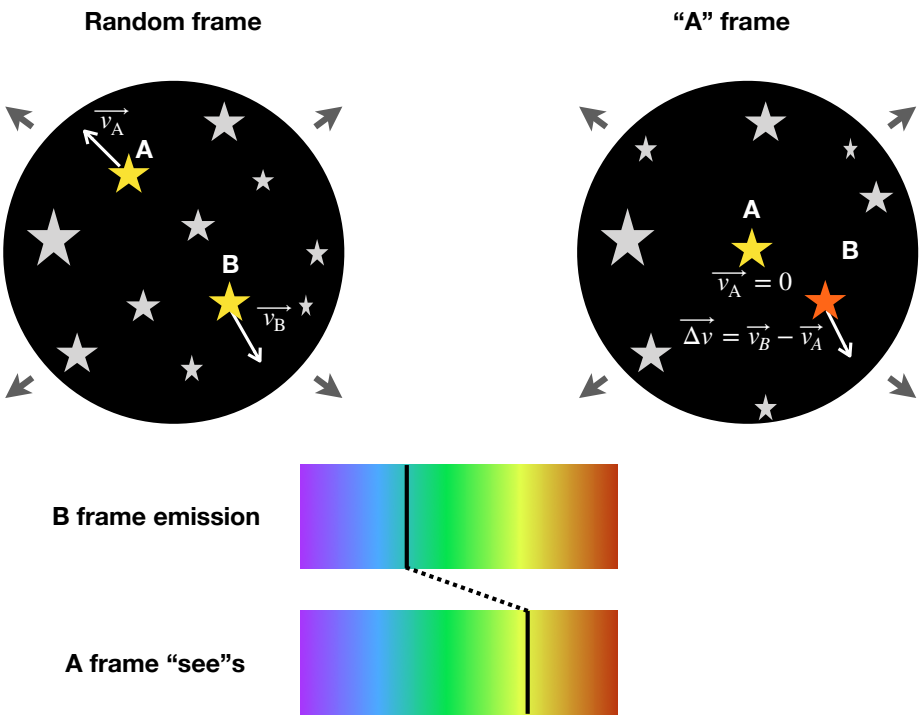

Figure 2.8: The redshift between two Galaxies A and B due to the expansion of the Universe. The situation is similar to the homologously expanding ejecta in supernova or kilonova ejecta if two different Galaxies are replaced by the two points in the ejecta.

2.4 Expansion opacity

2.4.1 Theory

With the new atomic data, we derive the bound-bound opacity. In supernova and kilonova, the ejecta are expanding homologously with a high velocity (a few percent of that of light in neutron star mergers) and at a high velocity gradient. In such media, the opacity is determined by adopting the expansion opacity formalism (Karp et al., 1977).

In expanding media, the photons are continuously redshifted in the comoving frame of the observer. The situation is similar to the case in the expanding Universe (see Figure 2.8). Take for example two stars belonging to two different Galaxies A and B, moving away from each other due to the expansion of the Universe. From the frame of A, it will always appear that B is moving away from A (note that, from B's frame, it will appear that A is moving away from B). Now if B emits a photon of wavelength λ_B, A will observe the photon wavelength to be redshifted at $\lambda_{obs,A} = \lambda_B(1 + |\vec{\Delta v}|/c)$. If we replace the moving Galaxies with two points in the expanding ejecta, the situation is similar.

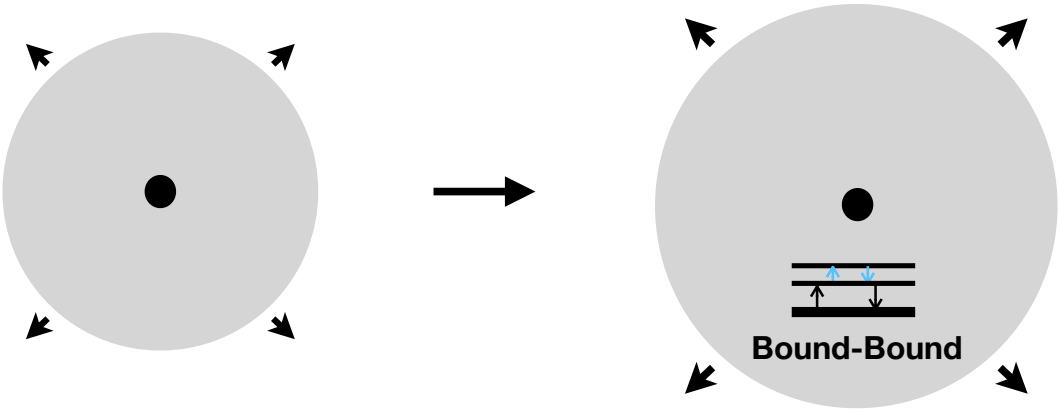

Figure 2.9: The continuous redshift in the photons in the expanding medium makes the photons to progressively coming into resonance with the lines. The wavelength average of the lines within a chosen wavelength bin ($\Delta\lambda$) gives the estimate of the expansion opacity (Karp et al., 1977).

The continuously redshifted photons in the expanding medium progressively come into resonance with different lines. Note that the resonance occurs over a certain wavelength range rather than at a particular wavelength. This is because the atomic lines are not infinitely thin, but have a width corresponding to the thermal motion. The thermal widths of the lines are negligible in comparison with the line spacing if the thermal velocity is much smaller than the expansion velocity. This is generally the case in supernova and in neutron star mergers, where thermal velocity $v_{\rm th} \sim 1{\rm km\,s^{-1}} << {\rm v_{ej}} \sim$ a few percent of the light speed. Under such condition, strength of each transition is evaluated by the Sobolev optical depth independent of any particular line profile function. We discuss more on the validity of the expansion opacity in Section 4.3.

When the Sobolev approximation is valid, the expansion opacity is calculated from the average mean free path between the lines within a reasonable wavelength bin. Suppose there are N strong lines inside an arbitrarily chosen wavelength bin of $\Delta\lambda$. In the homologously expanding ejecta, the velocity gradient required to redshift the photons from one line to another is:

$$\Delta v = c\frac{\Delta\lambda/N}{\lambda}. \tag{2.8}$$

Such a velocity gradient corresponds to a mean free path of Δvt at a time t. The corresponding absorption coefficient within the wavelength bin of λ to $\lambda + \Delta\lambda$ is written as (Kasen et al., 2013):

$$\alpha_{\rm exp}(\lambda) = \frac{1}{\Delta vt} = \frac{1}{ct}\frac{\lambda}{\Delta\lambda}N. \tag{2.9}$$

In this expression, only strong lines are considered. To include the contribution from the weak lines, a modified version derived by Eastman & Pinto (1993) is used:

$$\alpha_{\rm exp}(\lambda) = \frac{1}{ct}\sum_l \frac{\lambda_l}{\Delta\lambda}(1 - e^{-\tau_l}), \tag{2.10}$$

where λ_l is the transition wavelength in a chosen wavelength interval of $\Delta\lambda$. The Sobolev optical depth at the transition wavelength (τ_l) is calculated as

$$\tau_l = \frac{\pi e^2}{m_{\rm e}c} n_l \lambda_l f_l t, \tag{2.11}$$

where n_l is the number density of the lower level of the transition, and f_l is the oscillator strength of the transition. Then, we can calculate the expansion opacity as the absorption coefficient per unit mass density:

$$\kappa_{\rm exp}(\lambda) = \frac{\alpha_{\rm exp}(\lambda)}{\rho}. \tag{2.12}$$

We assume local thermodynamic equilibrium (LTE) to calculate the ionization fraction of the elements by solving the Saha ionization equation and to determine the population of the excited levels via Boltzmann statistics. The validity of LTE is discussed in Appendix A.

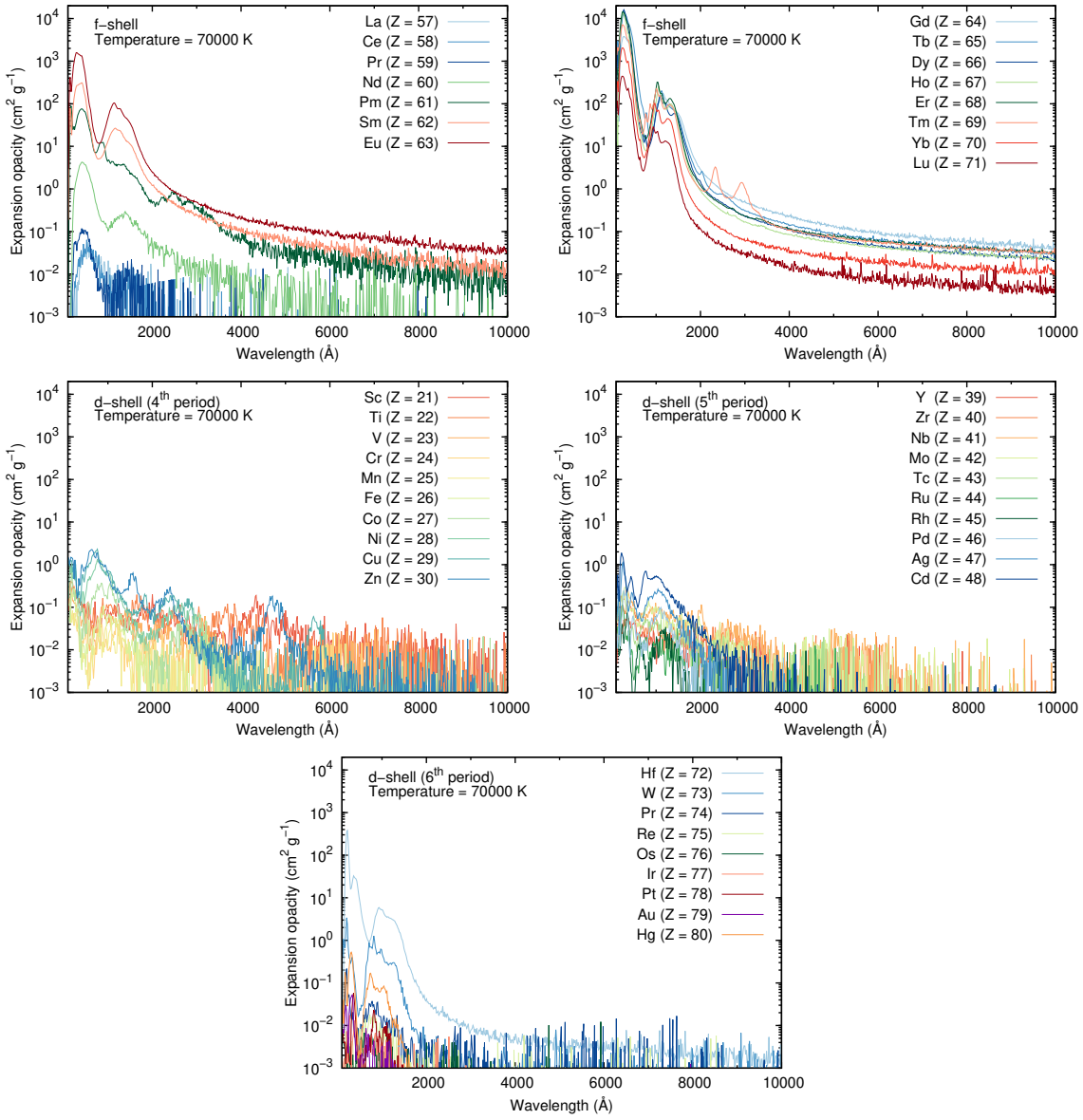

Figure 2.10: The expansion opacity as a function of wavelength at $T = 70000$ K, $\rho = 10^{-10}\,\mathrm{g\,cm^{-3}}$, and at $t = 0.1$ day for f-shell elements (top) and d-shell elements (middle and bottom). The middle panel is © AAS. Reproduced with permission.

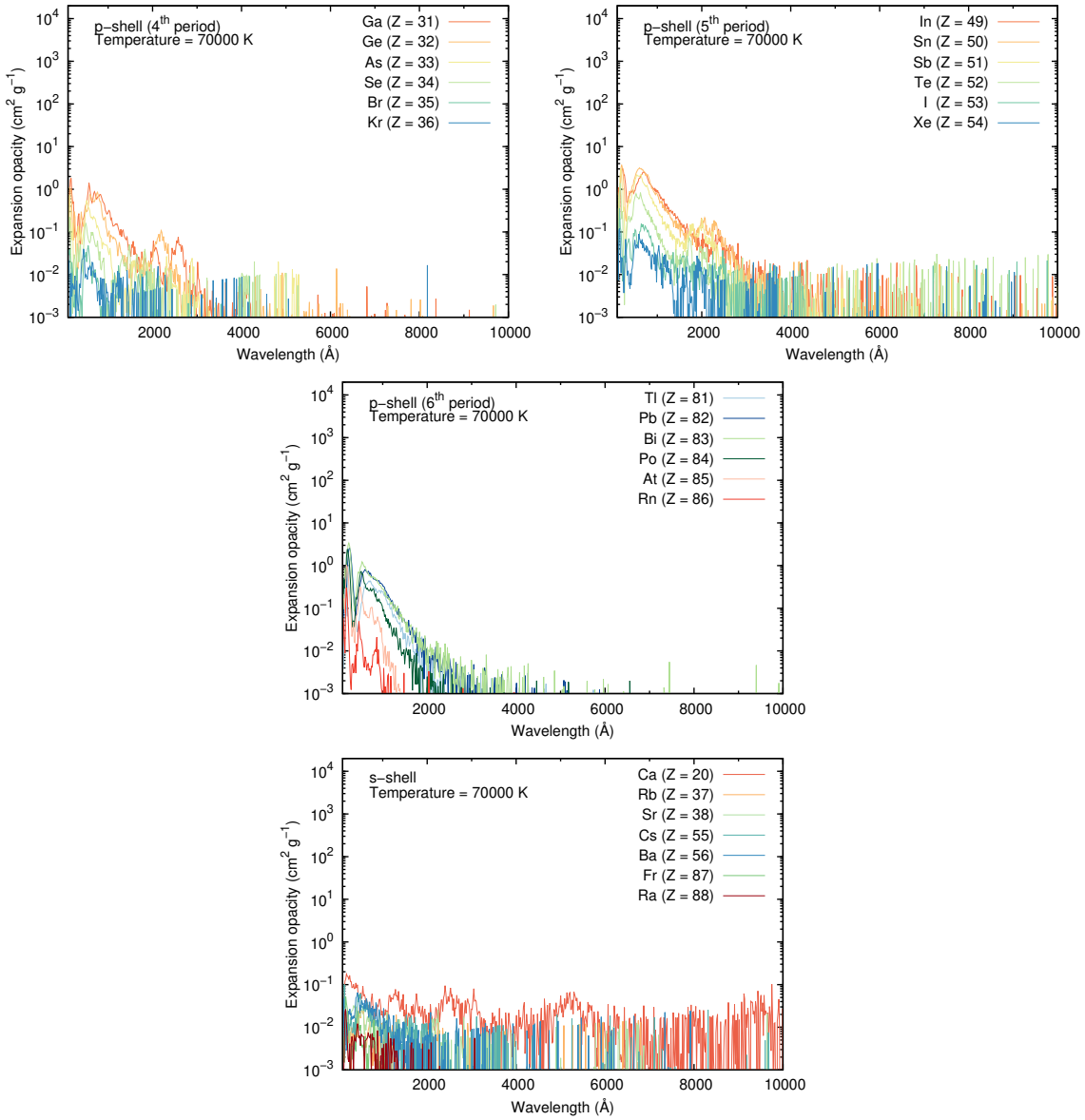

Figure 2.11: The expansion opacity as a function of wavelength at $T = 70000$ K, $\rho = 10^{-10}\,\mathrm{g\,cm^{-3}}$, and $t = 0.1$ day for p-shell elements (top and middle), and s-shell elements (bottom). The top panel is © AAS. Reproduced with permission.

2.4.2 Element-wise opacity

Using the expansion opacity formalism, we determine the opacity for a single element ejecta with the density $\rho = 10^{-10}\,\mathrm{g\,cm^{-3}}$ at $t \sim 0.1$ day for the elements with $Z = 20 - 88$.

Wavelength dependence of opacity

The expansion opacity in the neutron star merger shows a wide range of values ($\kappa_{\rm exp} = 0.001 - 1000\,\mathrm{cm^2\,g^{-1}}$ for s-shell elements to f-shell lanthanides (Figure 2.10, Figure 2.11). The expansion opacity for lanthanides are exceptionally high (Figure 2.10). For example, the expansion opacity at the peak reaches $\kappa_{\rm exp} \sim 1000\,\mathrm{cm^2\,g^{-1}}$ for Eu at $T \sim 70000$ K, whereas under the same condition, the light r-process element Cd reaches only up to $\kappa_{\rm exp} \sim 1\,\mathrm{cm^2\,g^{-1}}$. This is because of the fact that the significantly dense energy levels in the highly ionized lanthanides (Figure 2.5, Figure 2.6).

The expansion opacities show a strong wavelength dependence, with a higher value at shorter wavelengths. This is due to the higher number of transitions at the shorter wavelengths. Moreover, the lanthanide opacities show distinct peaks at short wavelengths, e.g., see $\lambda \sim 500\,\text{Å}$ and $\lambda \sim 1200\,\text{Å}$ in Figure 2.10 and Figure 2.11, which is due to the presence of many strong transitions at these wavelengths.

Temperature dependence of opacity

The temperature dependence of the expansion opacity is determined by convolving it with the blackbody function to calculate the Planck mean opacity. The Planck mean opacities for different elements show distinct peaks both at low and high temperatures, depending on elements (e.g., Figure 2.13, Figure 2.14). Here we mainly discuss about the behavior of opacity at high temperature (see Tanaka et al., 2020 for low temperature opacity).

At high temperature, the main factors that determine the trend of opacity peaks for the highly ionized ions are the following. The half-closed shells have the highest complexity measure, i.e., the number of energy levels are the highest for ions with half-closed shells. At moderate temperatures, the elements or ions with half-closed shells do not necessarily have the highest opacity since the Boltzmann statistics predicts that the lower energy levels are mostly populated and the transitions involving lower levels contribute the most to the opacity. However, at higher temperatures, higher energy levels can be populated. Hence, the opacities of the ions with half-closed shell, i.e., the ions with higher number of energy levels and transitions, are greater than other elements within the same shell.

The temperature variation of the mean opacity is different for elements with different shells. We discuss the temperature variation of the opacity across different shell elements. We first analyze the trend(s) for the representative element(s) in the shell (Figure 2.12) followed by the discussion on the general trends of the opacities in that shell.

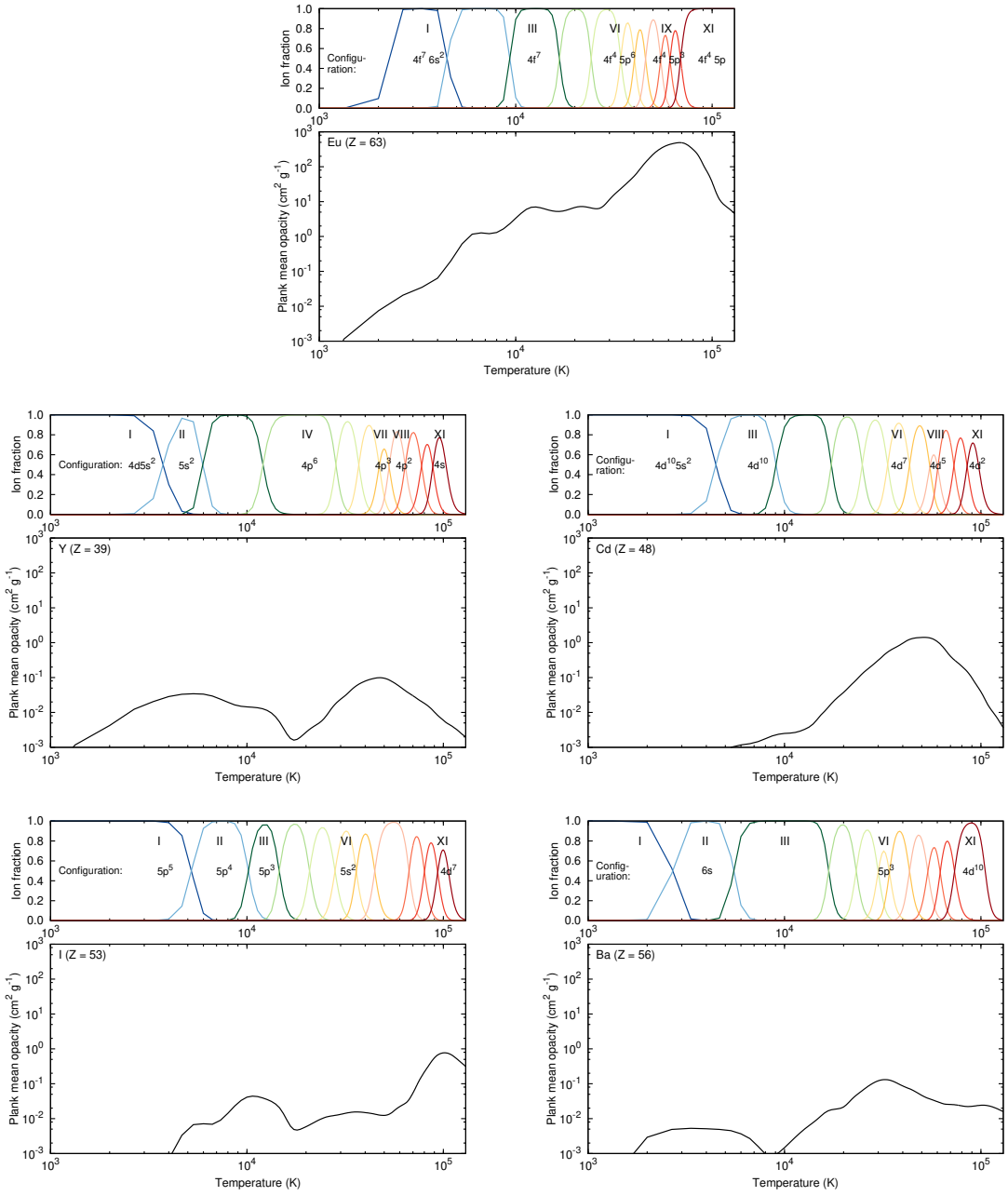

Figure 2.12: The change in the ion fraction and the variation of Planck mean opacity with temperature (top and bottom panel in each figure) for f-shell element Eu (top), d-shell element Y and Cd (middle), p-shell element I (bottom left), and s-shell element Ba (bottom right). The figures in the middle and bottom panel are

f-shell elements

We first discuss the temperature variation of Planck mean opacity for f-shell element Eu (Z = 63, top panel of Figure 2.12). The opacity shows a gradually increasing slope with temperature which becomes steeper at $T \geq 30000\,\mathrm{K}$. This is because Eu has open f-shell and for the ionization beyond Eu III, f-electrons are removed until ionization VI, starting from which, p-electron removal starts. Hence, starting from ionization VII, there are two open (p- and f-shell) shells (see Table D.1). Eu reaches $\sim$ VI ionization around $T \sim 30000\,\mathrm{K}$. Hence, the total number of the energy levels is increased starting from ionization VII (Figure 2.5, Figure 2.6) and hence, there is also a corresponding rise in the opacity.

The peak of the opacity appears at $T \geq 70000\,\mathrm{K}$, when Eu becomes IX ionized. This is because at this ionization, the open p-shell becomes half-filled (Table D.1). Since the half-filled shell show the maximum complexity, the number of energy levels and transitions also peak (Figure 2.6), and the opacity shows peak.

The variation of opacity in other f-shell elements can be understood in the same way (Figure 2.12). The opacities show steep increase at high temperature because of the presence of the two open shells in the highly ionized lanthanides and the peak appears when the p-shell becomes half-filled.

d-shell elements

As the ionization degree of d-shell element Y (Z = 39) increases with temperature, the Planck mean opacity evolves as shown in middle left panel of Figure 2.12. When Y is singly or doubly ionized (II $-$ III) at $T = 5000 - 10000$ K, it has a similar energy level distribution to the neutral s-shell elements Sr ($Z = 38$) and Rb ($Z = 37$). These elements contain only a few strong transitions. When Y becomes triply ionized (IV), it has a closed p-shell and the opacity decreases. As Y is ionized further, up to V $-$ VI, the shell configuration resembles neutral p-shell elements ($Z = 35 - 34$) with an energy level distribution at a higher energy. The opacity peaks when Y is sextuply ionized (VII) at $T \sim 50000$ K, at which it has a similar structure to neutral As ($Z = 33$), with a half-closed shell structure. Beyond this ionization (VIII $-$ XI), Y becomes similar to the neutral p- ($Z = 32 - 31$) and d- ($Z = 30 - 29$) shell elements. This leads to a decrease in the number of available energy levels, consequently reducing the opacity.

The behavior of another d-shell element Cd ($Z = 48$) is more straightforward (middle right panel of Figure 2.12). As the temperature increases, it loses d-shell electrons. When the d-shell has a half-closed structure, the element reaches peak opacity. Then, the opacity decreases as more d-shell electrons are lost at higher temperature.

The opacity evolution for other d-shell elements with temperature can be concluded in the same way, i.e., the opacity peaks when the element has half-closed p-shell or half-closed d-shell structures. The peak opacity is higher when the element has a half-closed d-shell structure ($\kappa_{\mathrm{mean}} \sim 1\,\mathrm{cm^2\,g^{-1}}$) rather than a half-closed p-shell structure ($\kappa_{\mathrm{mean}} \sim 0.1\,\mathrm{cm^2\,g^{-1}}$).

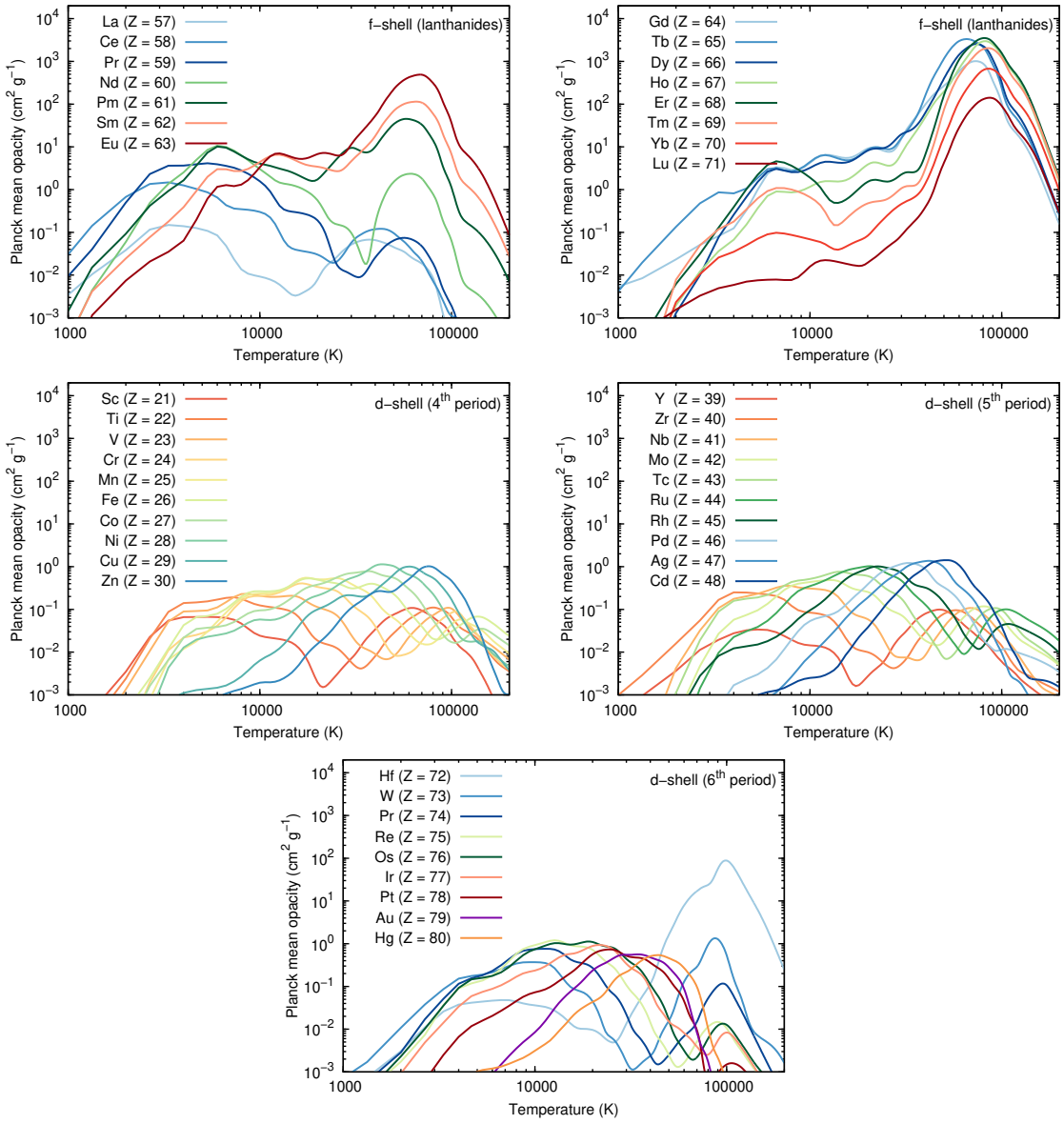

Figure 2.13: The Planck mean opacity as a function of temperature at $\rho = 10^{-10}\,\mathrm{g\,cm^{-3}}$ and $t = 0.1$ day for f-shell elements (top), d-shell elements (middle and bottom). The figures in the middle panel are © AAS. Reproduced with permission.

p-shell elements

The p-shell element I (Z = 53) has a complicated variation in opacity with the temperature but can be explained in a similar way (bottom left panel of Figure 2.12). The opacity is high when I resembles elements with half-closed shells. For instance, the opacity peaks at $T \sim 10^4$ K and at $T \sim 10^5$ K, when I has a similar structure to the neutral p-shell element Sb ($Z = 51$) and d-shell element Te ($Z = 43$) respectively, being doubly (III) and tenth (XI) ionized.

The trends in the other p-shell elements can be understood in the same way. Most of the p-shell elements have d-shell electrons at high ionization, with the opacity peaking at $\kappa_{\rm mean} \sim 1\,{\rm cm}^2\,{\rm g}^{-1}$. This is the reason why at early times (higher temperature), p-shell elements have a comparable opacity contributions to d-shell elements, which is different than the opacity at late time (see Tanaka et al., 2020).

s-shell elements

For the s-shell element Ba ($Z = 56$, bottom right panel of Figure 2.12), the opacity reaches a peak at $T \sim 4000$ K, when Ba is singly ionized (II) and has one neutral s-electron, similar to Cs ($Z = 55$). The opacity drops to a negligible value at $T \sim 8000$ K, when doubly ionized Ba (III) resembles the energy level distribution of neutral p-shell element Xe ($Z = 54$), which has a closed p-shell. Such ions have most of their energy levels distributed at higher energies, and thus fewer transitions take place as the Boltzmann statistics predicts most electrons exist in the lower-lying energy levels at this temperature range. The opacity rises to a higher value at $T \sim 30000$ K when the energy distribution is similar to the half-closed neutral p-shell element Sb ($Z = 51$). As the ionization degree increases, the opacity decreases again when Ba resembles the configuration of neutral d-shell elements with lower complexity.

The s-shell elements have comparatively lower opacity $\kappa_{\rm mean} \sim 0.001 - 0.1\,{\rm cm}^2\,{\rm g}^{-1}$. This lower opacity can be explained by s-shell elements never resembling neutral half d-shell elements at higher ionization. Note that they can be similar to neutral half p-shell elements.

In summary, the Planck mean opacity varies with temperature for different elements (Figure 2.13, Figure 2.14). With the increasing temperature and ionization, the effective shell structure of the ions change, the opacity varying accordingly. Highly ionized elements have the maximum bound-bound opacities when they have a half-closed shell structure.

Here we want to mention that the opacity is affected by the completeness of the atomic data since for the opacity at high temperatures, even energy levels lying at the higher energy are important. Hence, we investigate whether our atomic data include all the essential transitions (i.e., whether our atomic data are sufficiently complete). We find that the atomic data are nearly complete for opacity. For more details, see Appendix B.

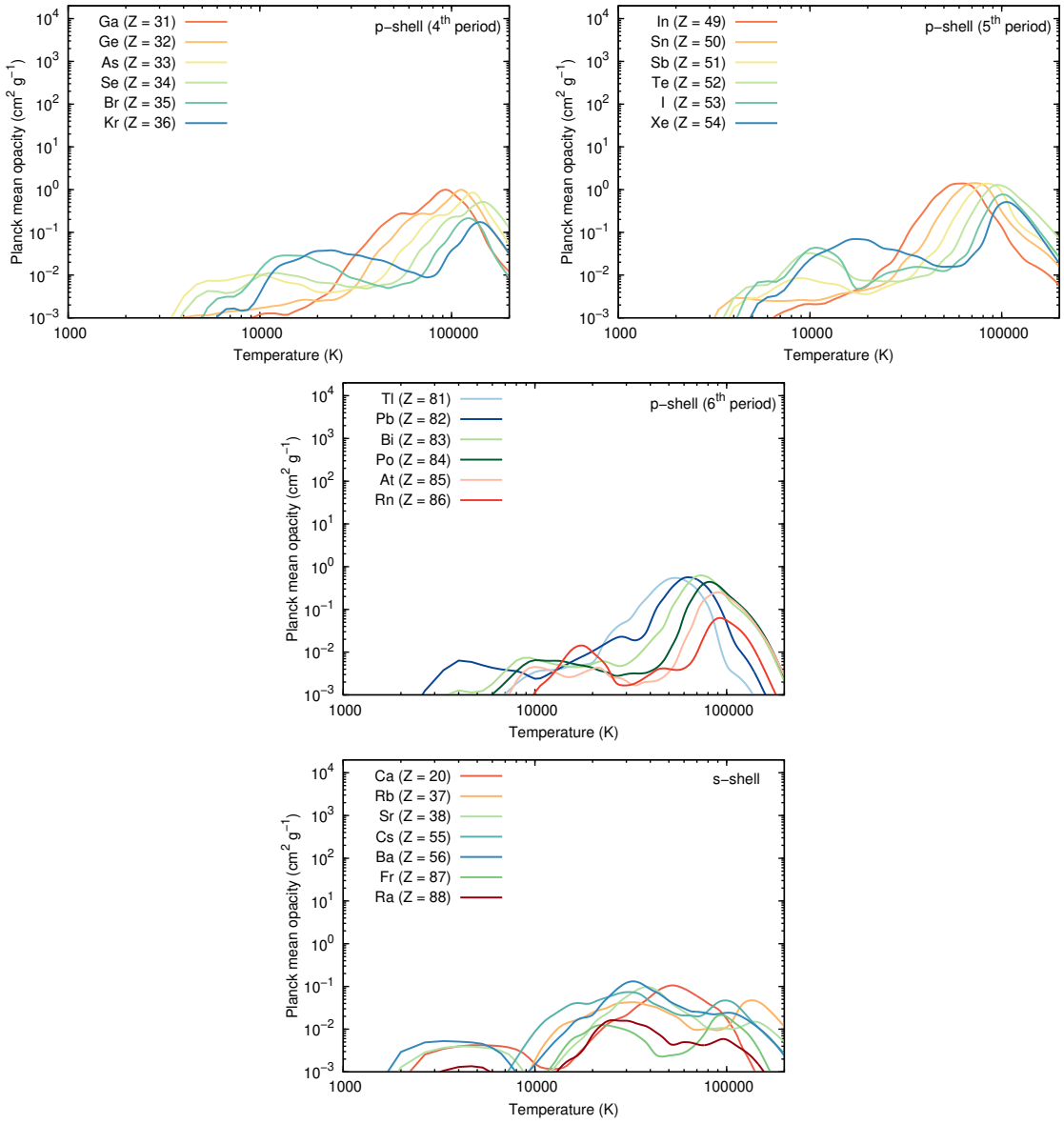

Figure 2.14: The Planck mean opacity as a function of temperature at $\rho = 10^{-10}\,\mathrm{g\,cm^{-3}}$ and $t = 0.1$ day for p-shell elements (top and middle), s-shell elements (bottom). The top panels are © AAS. Reproduced with permission.

2.4.3 Opacity for the mixture of elements

We discuss the opacity trends for the individual elements in Section 2.4.2. Nevertheless, neutron star merger ejecta consist of the mixture of elements. Hence, to calculate the realistic opacity for the neutron star merger ejecta, it is necessary to calculate the opacity for mixture of elements.

Depending on the electron fraction $Y_{\rm e}$, different abundance pattern is realized in the ejecta (see Figure 1.8). we calculate the opacity assuming two different abundances: (1) the ejecta containing only the light r-process elements corresponding to $Y_{\rm e} = 0.30 - 0.40$, which is suitable to estimate the bound-bound opacity for blue kilonova; (2) the ejecta containing lanthanides corresponding to $Y_{\rm e} = 0.10 - 0.20$, suitable to derive the bound-bound opacity for red kilonova (see Figure 1.9).

The abundance patterns are determined using the results from Wanajo et al. (2014) assuming that the mass distribution in the each $Y_{\rm e}$ bin is flat. We calculate the opacity for the element mixture at $t = 0.1$ and at $t = 1$ day. To model the typical conditions at these times, we set $\rho = 10^{-10}\,{\rm g\,cm^{-3}}$ for $t = 0.1$ day and $\rho = 10^{-13}\,{\rm g\,cm^{-3}}$ for $t = 1$ day.

Opacity for mixture at $Y_{\rm e} = 0.30 - 0.40$

The Planck mean opacity for ejecta with light r-process mixture shows an increase with time (top panel of Figure 2.15). The value of opacity is $\kappa_{\rm mean} \sim 0.5 - 1\,{\rm cm^2\,g^{-1}}$ for the typical conditions at $t = 0.1$ day, while the same at $t = 1$ day is $\kappa_{\rm mean} \sim 5 - 10\,{\rm cm^2\,g^{-1}}$. These results can be understood using Equation (2.12). Since the expansion opacity is inversely proportional to ρt, the change in ρt from $t \sim 0.1$ to 1 day increases the opacity by a factor of 100. Meanwhile, the Sobolev optical depth decreases with time, which reduces the contribution from the summation of $1 - e^{-\tau_l}$. As a result, the opacity increases by a factor of about 10 as time increases from $t = 0.1$ to 1 day.

The shape of the Planck mean opacity for an element mixture can be understood by individual element properties. At relatively low temperatures ($T < 20000$ K), the opacity increases with temperature. This is a property of d-shell elements that have the largest contribution to the opacity in this temperature range. The opacity displays some modulation by reflecting the behaviors of abundant individual elements. At high temperatures ($T > 20000$ K), the opacity evolves more smoothly with temperature because the contributions from p- and d-shell elements with different peak positions in the Planck mean opacity are averaged out.

Opacity for mixture at $Y_{\rm e} = 0.10 - 0.20$

The Planck mean opacities in presence of lanthanides show an increase with time at lower temperature (bottom panel of Figure 2.15). The value of opacity is $\kappa_{\rm mean} \sim 10\,{\rm cm^2\,g^{-1}}$ at $T \sim 10^4$ K for the typical conditions at $t = 0.1$ day, whereas the same at $t = 1$ day is $\kappa_{\rm mean} \sim 50\,{\rm cm^2\,g^{-1}}$. These results can be understood using Equation (2.12) similar to the case for $Y_{\rm e} = 0.30 - 0.40$.

The opacity value at higher temperature for lanthanide-rich ejecta can reach up to $\kappa \sim 5000\,{\rm cm^2\,g^{-1}}$ at $T = 60000$ K at $t \sim 1$ day and $T = 70000$ K at $t \sim 0.1$ day. The peak opacity value at $t = 0.1$ day does not show any difference with that at

$t = 1$ day, except for the fact that the opacity peak shifts to a lower temperature for the opacity at $t \sim 1$ day. This is because the opacity peak for lanthanides appears within a narrow ionization window of VII - IX. Ionization temperature shifts to the lower value for the lower density assumed for the ejecta at $t = 1$ day, which makes the elements ionized at relatively lower temperature than the condition at $t \sim 0.1$ day. Such a shift in ionization shifts the opacity peak to the lower temperature at $t = 1$ day.

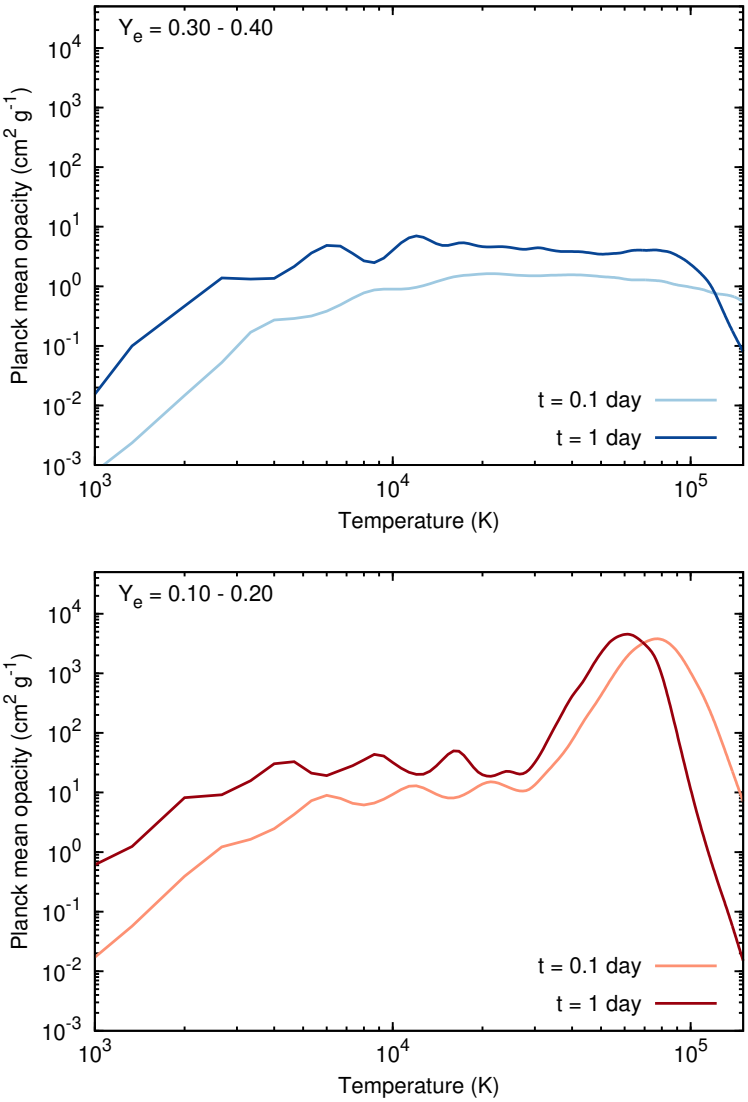

Figure 2.15: The Planck mean opacity as a function of temperature for the mixture of elements calculated at $t = 0.1$ day and $t = 1$ day at the fixed densities $\rho = 10^{-10}\,\mathrm{g\,cm^{-3}}$ and $\rho = 10^{-13}\,\mathrm{g\,cm^{-3}}$, respectively (light and deep shades of blue and red curves). The abundances are calculated according to the electron fraction $Y_\mathrm{e} = 0.30 - 0.40$ (top) and $Y_\mathrm{e} = 0.10 - 0.20$ (bottom). The top panels are © AAS. Reproduced with permission.

Chapter 3

Simulations of early kilonovae

3.1 Radiative transfer

3.1.1 Overview

Astronomy is the applied branch of physics. However, it is different in comparison to the other application fields, where the experiments can be performed in a laboratory to verify the theory. Much of what is known in astronomy today is from the photons from the cosmos. Hence, radiative transfer constitutes one of the central pillars of astronomy. In this chapter, we discuss the basics of radiative transfer and its specific use in the case of expanding ejecta, such as that in neutron star mergers.

When the light passes through a media, the specific intensity changes due to the absorption and the emission from the media (see Figure 3.1). The goal of the radiation transport is to calculate the monochromatic specific intensity I_ν (in units of erg cm^{-2} s^{-1} Hz^{-1} ster^{-1}) from a particular system by solving the radiative transfer equation:

$$\frac{dI_\nu}{ds} = -\alpha_\nu I_\nu + j_\nu, \tag{3.1}$$

where ds is the differential path length along the ray. j_ν is the monochromatic emission coefficient which is defined as the radiation energy emitted per unit volume per unit time per unit solid angle (in units of erg cm^{-3} s^{-1} Hz^{-1} ster^{-1}). α_ν is the monochromatic extinction coefficient (in units of cm^{-1}), which specifies the loss of intensity as the photon travels through a distance ds through absorption or scattering. For a medium of density ρ, the opacity κ_ν is related as α_ν/ρ. We can calculate the optical depth of the medium by integrating the extinction coefficient along the path of the photon:

$$\tau_\nu(s) = \int_{s_0}^{s} \alpha_\nu(s^{'})ds^{'} \tag{3.2}$$

The physical distance travelled in a homogeneous medium is defined as the mean free path which is calculated by $< \tau_\nu >= \alpha_\nu l_\nu = 1$. Hence the extinction coefficient and the mean free path of the homogeneous medium is related as

$$l_\nu = \frac{1}{\alpha_\nu} \tag{3.3}$$

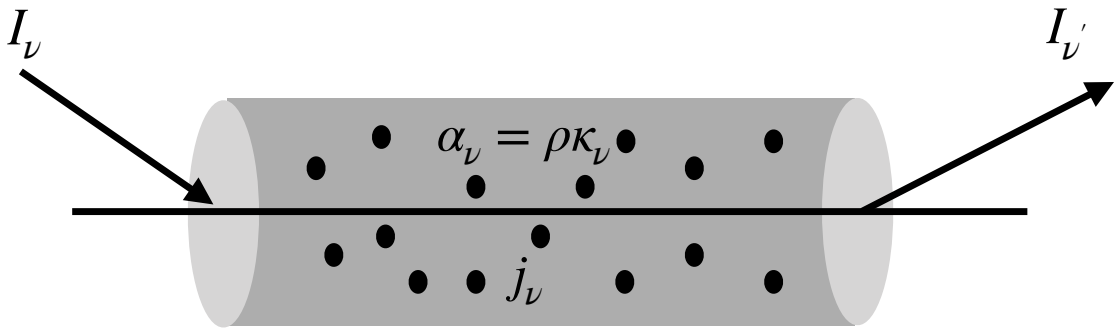

Figure 3.1: The light ray of intensity I_ν passing through a medium of emission and extinction coefficient j_ν and α_ν.

For a system in thermal equilibrium at a temperature T, the emission and extinction coefficient are related as

$$j_\nu = \alpha_\nu B_\nu(T). \tag{3.4}$$

More details on the basics of radiation transfer can be found from the classic textbooks (e.g., Rybicki & Lightman, 1986).

Provided with the extinction coefficient of any medium in thermal equilibrium, we can solve the Equation (3.1) by incorporating the Equation (3.4) to derive the specific intensity. However, in expanding media such as that in supernova or in the neutron star mergers, additional complications (and simplifications) are introduced due to its typical characteristics as we discuss in the next section.

3.1.2 Radiative transfer in expanding media

The photon transfer in the expanding media such as that in the neutron star mergers or supernova is different than that in the static media such as a star. The expansion of the media makes the photons to get continuously redshifted which should be properly treated to solve radiative transfer.

One important role of the progressive redshift is that the photons can escape through the lines unlike that in the static atmosphere in a star. For example, in the stars if a photon wavelength resonates with a line, then the photon can not escape. However, in expanding media, it is possible to escape through a resonant line since the photons are continuously redshifted.

At the same time, progressive redshift makes the problem of radiative transfer in the expanding media computationally challenging. The photon emitted at a particular wavelength comes in resonance with the huge number of lines with nearby wavelengths. Hence, determination of the extinction coefficient (or the opacity) involves the line transfer of many nearby lines. To tackle the problem computationally, the idea of the expansion opacity is introduced (Karp et al., 1977; Eastman & Pinto, 1993, also see Chapter 2).

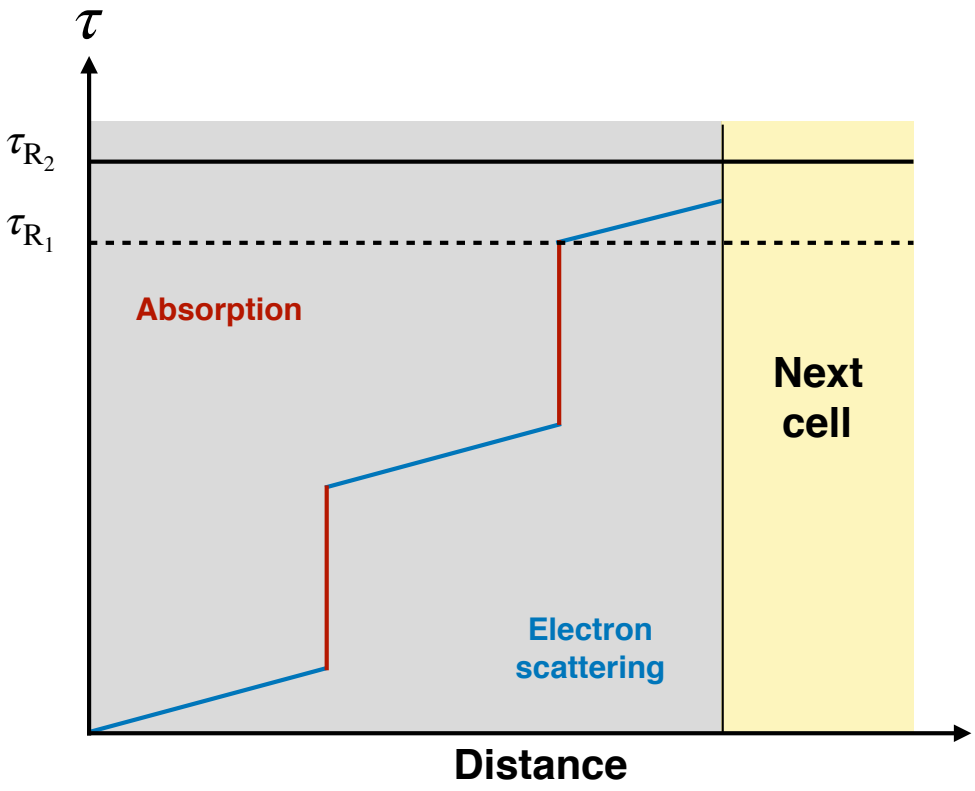

Figure 3.2: The procedure to sum up the optical depth in the Monte Carlo radiative transfer code. The optical depth increases continuously for the electron scattering and only at the resonance wavelength in case of the line transfer. If the optical depth reaches the cell boundary before reaching the threshold optical depth (see the case when the randomly chosen optical depth is $\tau_{\rm R2}$), the photon packet is moved to the next cell, otherwise, the photon is scattered (see the case when the randomly chosen optical depth is $\tau_{\rm R1}$). Note that this kind of photon transfer where the individual lines are treated separately are computationally expensive. Instead, our code treats the photon transfer by considering the total contribution from the electron scattering and absorption inside a chosen wavelength bin (the same as that chosen for the expansion opacity calculation).

Note that although several works have assumed the expansion opacity to model the light curves of supernova and kilonova, such assumption might fail to reproduce the true physical situation in presence of fluorescence (Pinto & Eastman, 2000) or if the number of lines are extremely high (see Chapter 4). Hence, several attempts to modify the expansion opacity is still on going (Fontes et al., 2015, 2017, 2020).

The expansion opacity approximation makes the radiative transfer in expanding media simpler than the line by line transfer. However, even under such assumption, solving the radiative transfer remains computationally infeasible. Instead, in this case, a technique called Monte Carlo method is introduced to solve the radiative transfer.

3.1.3 Monte carlo method

In Monte Carlo (MC) method, a large number of random experiments are performed (e.g., roll a dice to decide the outcome) to reach a solution instead of solving it in a detailed way. This method was first discovered by Stan Ulam while solving the neutron transport problem in 1946. Now the MC technique is widely used in several fields spanning from astronomy to finance. We will describe MC technique in context of the radiation transfer problem.

Let us consider the case of a static plane parallel isotropically scattering atmosphere (such as that in a star). Instead of solving the detailed radiative transfer equation, we roll a dice (use MC) to:

1. **Decide the direction of the photons.** First we choose a random number ξ between 0 to 1. Then the direction vector of the photon is calculated as: $\vec{r} = (1, \cos^{-1}(2\xi - 1), 2\pi(1 - \xi))$.

2. **Decide the propagation of the photon.** First we assume a random threshold optical depth as $\tau_{\rm R} = -\ln(1 - \xi)$ and the corresponding distance travelled (d) by the photon is determined. The photon positions are updated as $x = x + d\sin\theta\cos\phi$, $y = y + d\sin\theta\sin\phi$, $z = z + d\cos\theta$. Determination of d is the most computationally expensive and complicated part.

3. **Distribute / redistribute the wavelength of the scattered / absorbed photons.**

3.1.4 The MC radiative transfer code

We use a time- and wavelength-dependent MC radiative transfer code (Tanaka & Hotokezaka, 2013; Kawaguchi et al., 2018) which calculates the multi-color light curves and spectra for a given a density structure and abundance distribution assuming the homologously expanding motion of the ejecta.

In the code, the ejecta are divided into multiple cells for the computational convenience. The code assumes photon packet instead of the individual ray. First the photon packets are created according to the abundance and ejecta mass and distributed uniformly. The direction of the photons are assigned randomly (step 1) by MC method. Then the radiative transfer is solved by tracing the individual photon packets.

The photon transfer

When a photon packet enters a cell, there are a few possibilities. The photon packet can get scattered or absorbed (absorption includes bound-bound, bound-free and free-free processes), we define this as an event. Alternatively, the photon can move to the next cell or eventually escape the ejecta before any event occurs. Deciding whether the photon packet suffers an event and what happens afterwards are determined by MC (step 2).

We describe the procedure by following a photon packet moving through a cell. Since the event can occur at any point inside the cell, we choose a random threshold optical depth ($\tau_{\rm R}$). Then as the photon propagates through the cell, the extinction coefficient or the optical depth are incremented proportionally with the distance. Note that the code calculates the photon transfer by considering the total extinction coefficient ($\alpha^{\rm tot}(\lambda)$) where the contribution from electron-scattering, free-free, bound-free, and bound-bound transitions are included.

If the random threshold optical depth is reached before reaching to the next cell (for example, see the case when the randomly chosen optical depth is $\tau_{\rm R_1}$ in Figure 3.2), then the event is assumed to occur inside the cell. The distance travelled by photon to reach the random optical depth (d) is determined from the threshold optical depth and the opacity by $d = \tau_{\rm R_1}/\alpha^{\rm tot}(\lambda)$. Then the photon location is updated (step 2 is complete) and with the photon at the new location, a new MC game begins. Alternatively, if the next cell is reached before any event occurs (for example, the case $\tau_{\rm R_2}$ in Figure 3.2), the photon packet is transferred to the next cell and the new MC game begins.

So far, we did not mention about the wavelength of the photon packets. Such information is necessary to derive the spectra. While creating the photon packets, wavelengths are assigned randomly (step 3). After each event, the photon wavelength is updated if the event is absorption. After scattering the wavelength does not change in the comoving frame. However, this is not true in the rest frame. The wavelength or rather the frequency in the comoving frame of the packet is determined by:

$$\nu^{'} = \nu\gamma\left(1 - \mu\frac{v}{c}\right), \tag{3.5}$$

where the primed quantity denotes the comoving frame values, μ is the direction cosine between the path of the packet and the radial direction, and γ is the Lorentz factor given as:

$$\gamma = \left(1 - \mu\frac{v^2}{c^2}\right)^{-0.5}. \tag{3.6}$$

The energy also follows the relation given as:

$$\epsilon^{'} = \epsilon\left(\frac{\nu^{'}}{\nu}\right) \tag{3.7}$$

Note that in the case of absorption the wavelength and direction are updated even in the comoving frame. However, the corresponding rest frame quantities can be determined using the above formula in both absorption and scattering.

The energy must be conserved in the co-moving frame, i.e., $\epsilon^{'}_{\rm in} = \epsilon^{'}_{\rm out}$. Hence, by using Equation (3.7) and Equation (3.5), we get the energy of the packet in the

rest frame after the event:

$$\epsilon_{\rm out} = \epsilon_{\rm in} \frac{\left(1 - \mu_{\rm in}\frac{v}{c}\right)}{\left(1 - \mu_{\rm out}\frac{v}{c}\right)}, \tag{3.8}$$

where $\mu_{\rm in}$ aand $\mu_{\rm out}$ are the direction cosines of the incoming and the outgoing radiation in the rest frame. The frequency of the photon in the rest frame after the event is determined by

$$\nu_{\rm out} = \nu_{\rm in} \frac{\left(1 - \mu_{\rm in}\frac{v}{c}\right)}{\left(1 - \mu_{\rm out}\frac{v}{c}\right)} \tag{3.9}$$

Integrated moments

After the photon transfer, the photon flux in the each cell is calculated. The contribution of a photon packet to the cell's integrated moments are calculated when a photon crosses the mid point in a cell. The intensity in the rest frame can be calculated as

$$I_\nu \Delta\nu\Delta\Omega = \frac{n_{\rm ph}\epsilon}{\Delta t|\mu|}, \tag{3.10}$$

where $n_{\rm ph}$ is the number of photon packets propagating at a direction μ in the frequency range of $\Delta\nu$ crossing a unit area with solid angle Ω per unit time Δt.

Using the relation between the co-moving frame and the rest frame intensity as $I_\nu = (\nu/\nu^{'})^3 I_\nu^{'}$ and $\Delta\nu^{'}\Delta\Omega^{'} = (\nu/\nu^{'})\Delta\nu\Delta\Omega$ (Mihalas & Kunasz, 1978), we can also calculate the intensity in the comoving frame by:

$$I_{\nu^{'}}^{'}\Delta\nu^{'}\Delta\Omega^{'} = \frac{n_{\rm ph}\epsilon}{\Delta t|\mu|}\left(\frac{\nu^{'}}{\nu}\right)^2. \tag{3.11}$$

From the above relation, the estimators of the intensity moments such as the mean intensity (zeroth moment of the intensity) or the flux (first moment of the intensity) can be derived in either frame.

Temperature determination

One of the most important step in the code is to determine the temperature using the derived mean intensity. We obtain frequency dependent mean intensity by summing over all the photon packets that cross the unit area $\Delta\Omega$ and then by averaging over the area $4\pi r^2$ as

$$J_\nu^{'} = \frac{1}{\Delta 16\pi^2 r^2}\frac{1}{\Delta t}\sum\frac{\epsilon}{|\mu|}\left(\frac{\nu^{'}}{\nu}\right)^2. \tag{3.12}$$

Similarly the mean intensity in rest frame can be derived. Then the zeroth frequency moment of the mean intensity or the averaged mean intensity in the rest frame is determined as $J = \int J_\nu d\nu$. The radiation temperature is now determined straightforwardly from the Stephan-Boltzmann law

$$T = \left(\frac{\pi}{\sigma} < J > \right)^{1/4} \tag{3.13}$$

Note that the code assumes that the electron temperature is same as the radiation temperature following Kromer & Sim (2009). The code is tested enough on whether such assumption provides reasonable results for type Ia supernova (Tanaka & Hotokezaka, 2013).

Summary of the code structure

We summarize the overall algorithm and the structure of the code in the following. The schematic of code structure is shown in the Figure 3.3.

1. **Input:** The code requires the user defined density structure, the corresponding total ejecta mass, and the abundance pattern. A trial temperature structure is also given as an input.

2. **Algorithm:** The code calculates the total energy deposited in the ejecta according to the input ejecta mass and creates the photon packets by equally dividing the total radioactive energy into the packets. Then the level population and the ionization are calculated using the trial temperature structure. Now the corresponding extinction coefficient or the opacity can be calculated.

   The energy packets are propagated by interacting with the ejecta according to the extinction coefficient. By tracing the photon packets, the mean intensity of the radiation field is determined. The mean intensity of the photon field is used to determine the temperature structure and the process is reiterated.

   Note that the code starts with a trial temperature structure and the radiation field derived in the first simulation step is not correct. However, after a few iterations, the calculation becomes trustable even in the first step.

3. **Output:** By tracking the history of the photon packets, the code calculates the photon flux and provides with the spectrum and the light curve.

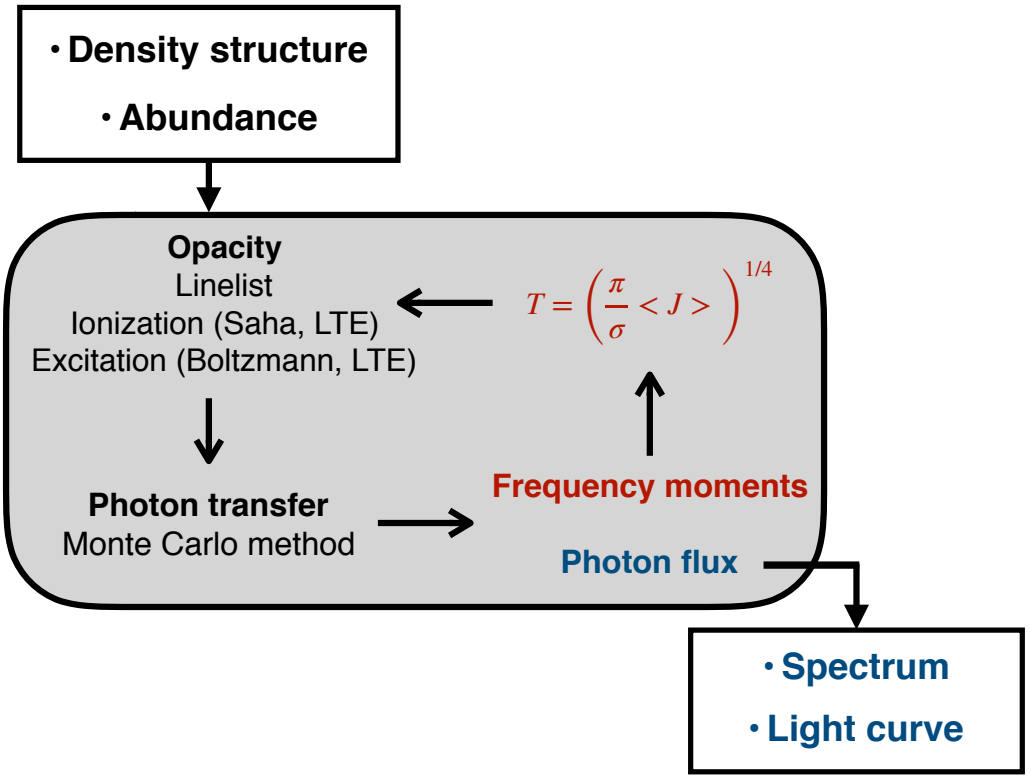

Figure 3.3: The algorithm for the Monte Carlo code (Tanaka & Hotokezaka, 2013).

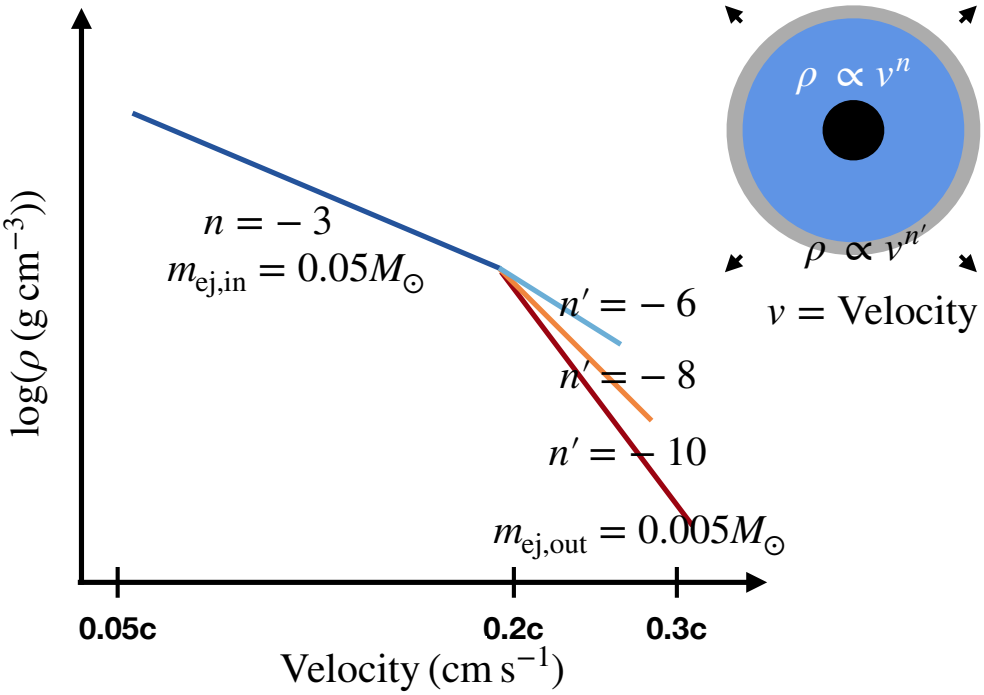

Figure 3.4: The simple spherical power law density structure considered as the fiducial model (navy blue curve) employed to calculate the light curve for the lanthanide-free and lanthanide-rich ejecta. For lanthanide-free ejecta, additional models with steeply declining outer layer are also included for calculation.

3.2 Ejecta model

We calculate the 1D kilonova light curves using the time- and wavelength-dependent radiative transfer code (Tanaka & Hotokezaka, 2013; Tanaka et al., 2014; Kawaguchi et al., 2018) using new atomic opacities. The new atomic opacity data enable us to calculate the radiation transfer starting around $\sim$ 1 hour after the merger.

Note that we use the total opacity in calculating the light curve. We consider the transitions in a wavelength range of $100 - 35000$ Å. There is no available bound-free cross section data for the elements with $Z > 26$, i.e., Fe. Following the method adopted by Tanaka & Hotokezaka (2013), we use the cross sections of Fe for elements with a higher Z in the radiative transfer simulation. This crude approximation does not alter the results since the bound-free transition opacity is not predominant (Section 2.2).

We use a simple homologously expanding spherical ejecta model (Metzger et al., 2010) with a total ejecta mass of $M_{\rm ej} = 0.05 M_\odot$. Thanks to the homologous expansion, we use the velocity as a spatial coordinate since $v = r/t$. We assume the ejecta have a power law density structure $\rho(v,t) \sim \rho_0 (v/v_0)^n (t/t_0)^{-3}$ from a velocity $v = 0.05$c to 0.2c (Metzger et al., 2010).

The radioactive heating rate of r-process nuclei is calculated according to $Y_{\rm e}$, using the results from Wanajo et al. (2014) assuming a flat distribution of mass for each value in the $Y_{\rm e}$ range. The time-dependent thermalization factor is adopted from Barnes et al. (2016). The radiative transfer calculation is performed using MC method, the details of which is already discussed in Section 3.1.4.

We calculate the light curves for (1) lanthanide-free and (2) lanthanide-rich ejecta from neutron star merger. Such cases represent the light curves observed from the polar and equatorial directions (see Chapter 1). For both cases, we assume $n = -3$ for our fiducial model motivated by the ejecta structure from the results of numerical simulations (e.g., Bauswein et al., 2013). The difference in these two cases is in the abundance patterns as described below.

Abundance for lanthanide-free kilonova:

The electron fraction is assumed to be in the range of $Y_{\rm e} = 0.30 - 0.40$ for the lanthanide-free kilonova. In such conditions, the main nucleosynthesis products are the light r-process elements (the blue curves in Figure 1.8, Wanajo et al., 2014). Throughout the ejecta, the same $Y_{\rm e}$ distribution, and hence homogeneous elemental abundance pattern, are assumed.

The velocity scale and the range of $Y_{\rm e}$ in our fiducial model are typical for the disk wind ejecta, particularly in the case of a relatively long-lived hypermassive neutron star (Perego et al., 2014; Metzger & Fernández, 2014; Lippuner et al., 2017; Siegel & Metzger, 2017; Fujibayashi et al., 2018; Fernández et al., 2019). In reality, the disk wind ejecta are enveloped inside a faster moving dynamical ejecta (Hotokezaka et al., 2013b). To study the effect of the dynamical ejecta, we further include models with a continuous thin outer layer at $v > 0.2c$ with a fixed mass of $M_{\rm out} = 0.005 M_\odot$. The layer has a steeper density structure $\rho(v,t) \sim \rho_0 (v/v_0)^{n'} (t/t_0)^{-3}$ where $n' = -6, -8$, and -10. According to the slope, the maximum outer velocity changes as $v \sim 0.24$c, 0.25c, and 0.33c, for $n' = -6, -8$, and -10, respectively. We assume the same $Y_{\rm e}$

range for these outer ejecta components.

Abundance for lanthanide-rich kilonova:

The elemental abundance in the ejecta is assumed to consist of the single lanthanide element (Nd, Sm, or Eu, considered as different models) with a mass fraction $X_{\rm La} = 0.1$. Such a fraction of lanthanide is obtained in an ejecta with $Y_{\rm e} = 0.20$ (the red curve in Figure 1.8), the typical value for electron fraction $Y_{\rm e}$ in the tidal dynamical ejecta. The remaining of the ejecta are assumed to consist of the light r-process abundance, where the abundance for the light r-process elements is calculated in the same way as that for the lanthanide-free kilonova. We renormalise the abundance to match the total mass fraction of the light r-process elements to be 0.9. Note that we consider the heating rate is entirely due to the light r-process elements. This assumption does not affect the result since including single lanthanide does not change the heating rate significantly.

Note that in case of the lanthanide-rich kilonova, we assume single lanthanide element (Nd, Sm, or Eu) can reproduce the opacity for the lanthanide mixture. One of the reasons behind this is that performing the radiative transfer simulation using the complete linelist is infeasible for the lanthanide-rich case since the number of transitions is extremely high. For instance, the number of lines in the linelist for Eu can be up to ~ 0.3 billion (Table D.1). On the other hand, the linelist for the light r-process abundance consists up to ~ 10 million lines. Note that we have used the elements from the first half of lanthanides, which have the lower opacity than the second half of the lanthanides (Figure 2.13). Nevertheless, our calculations provide a reasonable upper limit of the light curve in the presence of lanthanides.

Even with a single lanthanide, our radiative transfer simulation is infeasible with the original linelist with lanthanides. Hence, we make a reduced linelist for lanthanides with the ionization $>$ V. For this purpose, we randomly select the transitions from the original linelist by keeping the statistical properties the same. For more details and validity of the scheme, see Appendix C. Performing the radiative transfer using the complete linelist with all the lanthanides remains within the scope of future work.

3.3 Results

3.3.1 Lanthanide-free kilonova

Evolution of opacity

As the ejecta expand, the temperature and the density of the ejecta decrease. The opacity also evolves with time accordingly. Therefore, it is useful to study the time evolution of the opacities at a fixed position in the ejecta. Figure 3.5 shows the temperature, density and opacity evolution at the ejecta point $v = 0.1c$ for our fiducial model. The dominant component is the bound-bound opacity, followed by the electron-scattering, bound-free, and free-free opacity. The total opacity varies from $0.1 - 10\ {\rm cm^2\,g^{-1}}$ from $t \sim 0.1$ day to $t \sim 1$ day.

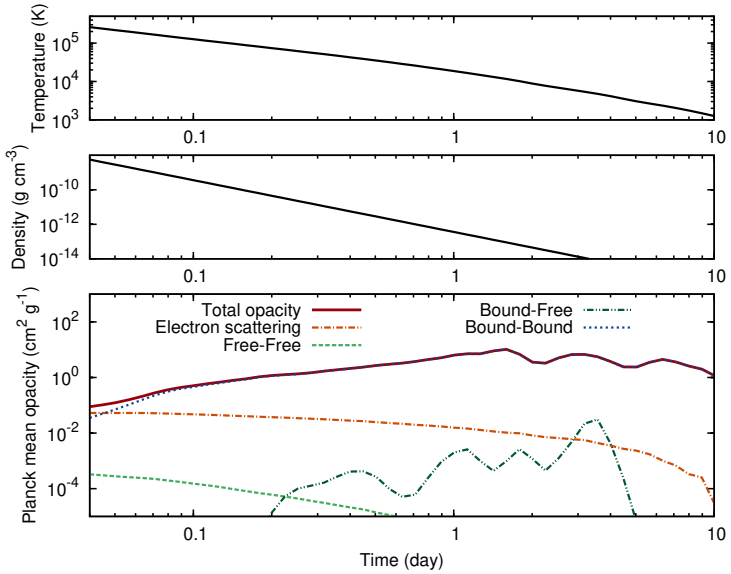

Figure 3.5: **Top:** The temperature evolution for the fiducial model with $M_{\rm ej} = 0.05 M_\odot$ and $Y_{\rm e} = 0.30 - 0.40$, at a fixed ejecta point $v = 0.1$c. **Middle:** The density evolution for the fiducial model at $v = 0.1$c. **Bottom:** The Planck mean opacity variation with time at $v = 0.1$c. The red line describes the total opacity. The blue line describes the bound-bound opacity, the component which contributes the most to the total opacity except for at around $t \sim 1$ hour. The orange, light green, and the dark green curves are the electron scattering, free-free, and bound-free opacity components, respectively.

The contribution of electron scattering to the total opacity is higher at earlier times, reaching a majority contribution, $> 50\,\%$, at $t \sim 1$ hour (Figure 3.5). This high electron scattering contribution occurs at an early time as high temperatures ($T > 10^5$ K) cause a high degree of ionization, which raises electron density. The electron scattering opacity decreases with time as the ejecta temperature decreases. Around $t \sim 6$ days, the electron scattering contribution drops steeply because most of the elements recombine to neutral atoms.

The free-free component remains small throughout the evolution of the total opacity. At $t \sim 0.1$ day, the opacity has a value of $\kappa^{\rm ff}_{\rm mean} \sim 10^{-4}\,{\rm cm^2\,g^{-1}}$; this value falls faster than the electron scattering opacity component as time increases. From Equation (2.3) and Equation (2.4), we can see that the free-free opacity varies as $\kappa^{\rm ff}_{i,j}(\lambda) \propto \rho T^{-\frac{1}{2}}(1 - e^{-\frac{hc}{\lambda k T}})$. Since the density decreases faster than temperature as time increases, the free-free opacity decreases with time.

The bound-free opacity varies with time but never becomes large enough to significantly contribute to the total opacity. As discussed in Section 2.2, although the photo-ionization cross section itself is high, the fraction of high energy photons is small, and thus, the Planck mean opacity is moderate. The bound-free opacity component shows an increasing trend, reaching its peak value of $\kappa^{\rm bf}_{\rm mean} \sim 0.04\,{\rm cm^2\,g^{-1}}$ a few days after the merger. This is as a result of the ionization degree decreasing with time, hence more photons are present beyond the potential energy of ions. It should be noted that the value of the bound-free opacity before $t = 0.2$ day is not

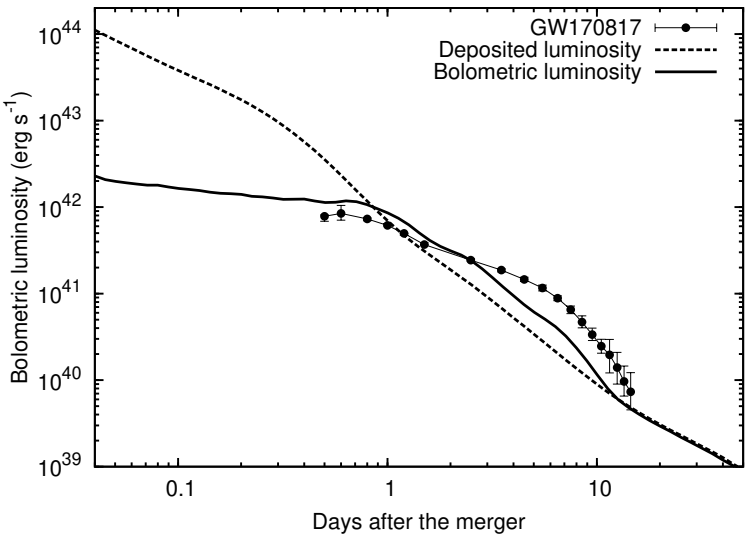

Figure 3.6: The bolometric light curve for the fiducial model with $M_{\rm ej} = 0.05 M_\odot$ and $Y_{\rm e} = 0.30 - 0.40$ and simple power law density structure (with slope $n = -3$). The black dots represent the bolometric light curve of GW170817 (Waxman et al., 2018). © AAS. Reproduced with permission.

correctly followed in the radiative transfer code, since the wavelength range beyond the ionization threshold is not covered by our wavelength grid (down to 100 Å).

The bound-bound opacity component evolves from $\kappa^{\rm bb}_{\rm mean} \sim 0.5$ to $5\,{\rm cm^2\,g^{-1}}$ from $t = 0.1$ to 1 day. Excluding the time around 1 hour, this component alone is representative of the total opacity. It is to be noted that most of the previous works have considered a fixed opacity value of 1 ${\rm cm^2\,g^{-1}}$ or less (Kasliwal et al., 2017; Villar et al., 2017; Piro & Kollmeier, 2018; Gottlieb & Loeb, 2020) to calculate blue kilonovae from GW170817 at $t < 1$ day. This assumption is not valid precisely, as the change in the opacity with time is quite large for even high $Y_{\rm e}$ ejecta.

Bolometric light curves

The bolometric luminosity for the fiducial model is shown in Figure 3.6. The luminosity deposited the ejecta (or thermalized radioactive luminosity) is shown by the dashed line for comparison. At $t < 1$ day, the observable bolometric luminosity is an order of magnitude lower than the deposition luminosity because the ejecta are optically thick, hence photons cannot escape from the ejecta. At $t > 1$ day, the previously stored radiation energy from $t < 1$ day starts to be released and the bolometric luminosity supersedes the deposition luminosity. Finally, the bolometric luminosity follows the thermalized radioactive emission at $t > 10$ days.

The bolometric light curve of GW170817 (Waxman et al., 2018) is shown for comparison. Our fiducial model with $M_{\rm ej} = 0.05 M_\odot$ gives a reasonable agreement with the observed data at early times. The required ejecta mass is consistent with the findings of previous works (Kasliwal et al., 2017; Waxman et al., 2018; Hotokezaka & Nakar, 2020).

The presence of a thin outer layer affects the light curves at an early time (Figure 3.7). The steeper slope of the outer ejecta makes the luminosity fainter at $t \leq 1$ day.

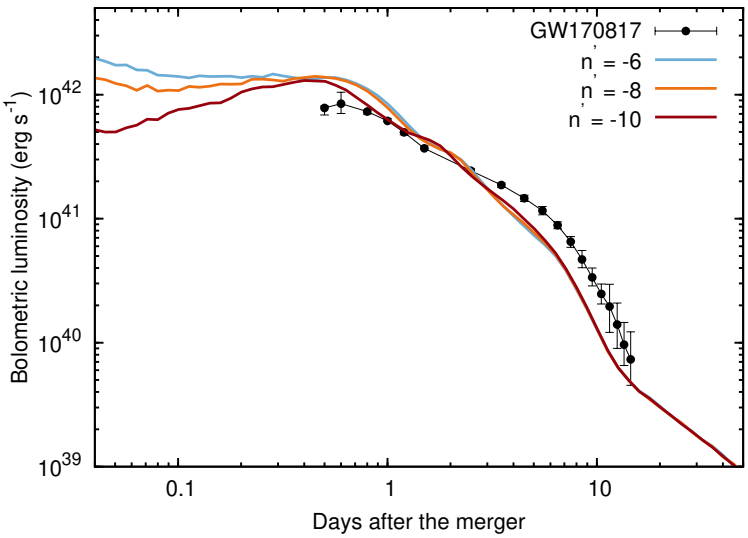

Figure 3.7: The bolometric light curves for models without and with a thin layer (with density slopes $n^{'} = -6, -8, -10$). The bolometric light curves of GW170817 (Waxman et al., 2018) are shown for reference. Presence of the thin outer layer makes the light curves fainter at early time ($t \sim 0.1$ day). The degree of faintness increases with the increase in the slope of the outer layer.

In the early time, the ejecta are optically thick and the emission from the outermost layer determines the light curve. Adding a thin outer layer to the ejecta changes the mass located outside of the diffusion sphere in the early time. Our fiducial model has a higher density at the diffusion sphere, producing a high luminosity in the early time (Figure 3.7). For the models with thin layers, the density at the diffusion sphere becomes lower. Since the model with a steeper slope has a lower density of the optically thin layer for a fixed mass of the outer ejecta, the model displays a fainter luminosity. After around $t > 1$ day, the thin layer has almost no effect on the light curve because thin ejecta are already optically thin and so do not contribute to the luminosity anymore.

Spectra

The spectra for the lanthanide-free model with no outer layer are plotted in absolute magnitude at $t = 0.1$, 1, and 10 days after the merger (Figure 3.8). The spectral shape shows a strong time evolution from UV ($t \leq 1$ day) to optical ($t \sim$ a few days) towards infrared wavelengths at later times ($t \sim$ a week). This is consistent with the expectation. The spectra is highly featureless. However, we do not attempt to discuss the individual elemental signature since the accuracy of our theoretically calculated atomic data are not enough for discussing the spectral features.

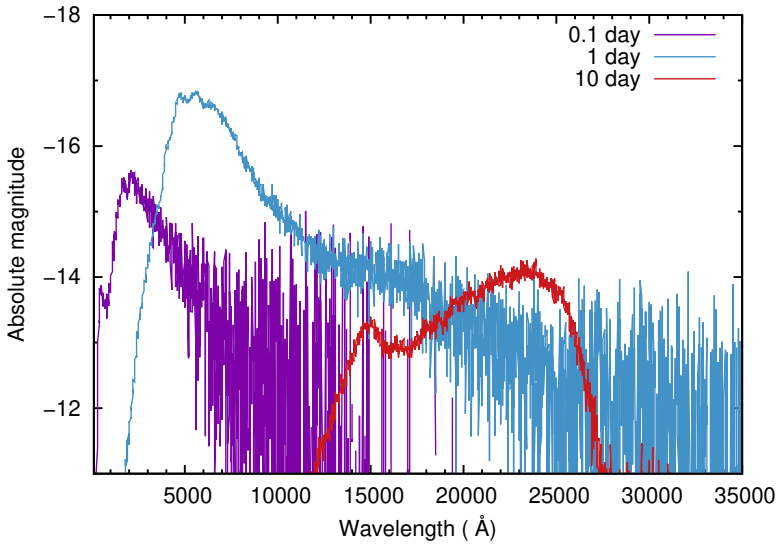

Figure 3.8: The spectra for the lanthanide-free model with no outer layer and $M_{\rm ej} = 0.05 M_\odot$ and $Y_{\rm e} = 0.30 - 0.40$ for an assumed simple power law density structure (with slope $n = -3$). The different colors represent different timescale. The spectra evolve from UV towards the NIR. © AAS. Reproduced with permission.

3.3.2 Lanthanide-rich kilonova

Evolution of opacity

Inclusion of the lanthanides in the ejecta mainly changes the bound-bound component of opacity. The other components are almost unchanged. Hence, we will only discuss the evolution of the bound-bound opacity in this section.

Figure 3.9 shows the bound-bound opacity evolution in the outermost layer in presence of lanthanides. A distinct peak in the opacity can be seen at $t \sim 0.1$ day, the opacity decreases and the value becomes almost equal to the opacity in lanthanide-free ejecta at $t \sim 0.4$ day, after which the opacity increases again to show an opacity peak at $t \sim 1$ day.

We can understand the peak opacity evolution by understanding the temperature and the ionization evolution in the ejecta. As the ejecta expand, the temperature and the corresponding ionization of the ejecta decrease. At $t = 0.1$ day, the temperature of the outermost layer provides the suitable condition ($T < 70000$ K) to reach the ionization range of VII - IX, where the opacity peaks appear for lanthanides (Figure 2.10).

As the ejecta expand further with time, the temperature and the ionization at outer layer of the ejecta decreases (Figure 3.9). As a result, the opacity decreases since the ejecta moves out of the ionization range (VII - IX) at which the opacity peak appears for lanthanides. At around $t \sim 0.4$ day, the opacity is essentially the same as that of the ejecta with no lanthanide. Finally, at $t \sim 1$ day, the outermost layer of the ejecta cools down enough ($T < 10000$ K) so that the peaks of the opacity of the low-ionized lanthanides appear.

The high temperature opacity peak for the ejecta containing Eu is orders of mag-

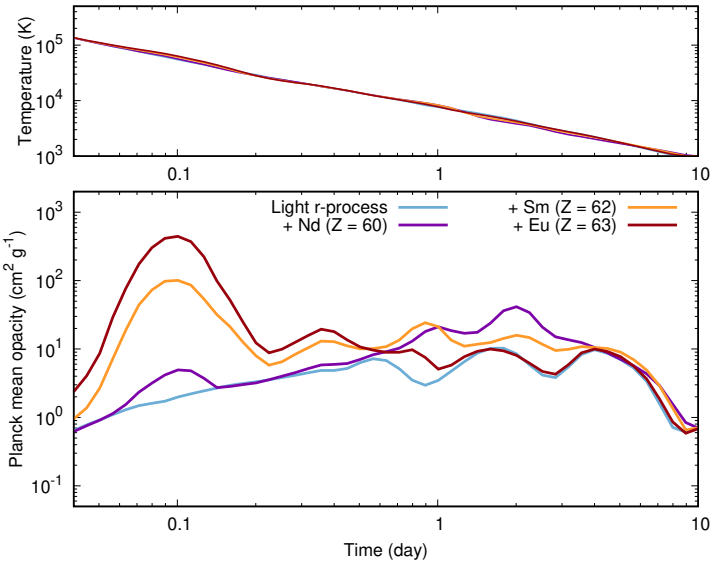

Figure 3.9: The time evolution of the temperature (upper panel) and the Planck mean opacity (lower panel) at outer layer of the ejecta ($v \sim 0.19$c). The ejecta are considered to consist of a single lanthanide (Nd or Sm or Eu with lanthanide fraction fized at $X_{\rm La} = 0.1$) together with the light r-process elements. The opacity evolution for the ejecta containing only the light r-process elements is also shown for purpose of comparison (blue curve). The presence of lanthanides increases the opacity a few orders of magnitude at $t \sim 0.1$ day. © AAS. Reproduced with permission.

nitude higher in comparison to the ejecta containing Nd ($500\,{\rm cm^2\,g^{-1}}$ and $5\,{\rm cm^2\,g^{-1}}$, respectively, for Eu and Nd). This is because the energy level density for the presence of Eu is much higher than Nd (Figure 2.5, Figure 2.6).

Bolometric light curves

At $t \sim 0.1$ day, the bolometric luminosities for the lanthanide-rich models is about $L_{\rm bol} \sim 0.5 - 1 \times 10^{42}\,{\rm erg\,s^{-1}}$ (different for different models, Figure 3.10). This luminosity is fainter than lanthanide-free ejecta ($L_{\rm bol} \sim 2 \times 10^{42}\,{\rm erg\,s^{-1}}$) by a factor of four to two, depending on different models. The light curves for lanthanide-rich ejecta rise afterwards and show no difference with that of lanthanide-free case at $t \sim 0.4$ day. Finally, the luminosities for lanthanide-rich models drop and show deviation again at around $t \sim 1$ day.

The shape of the bolometric light curve at early time is determined by the opacity in the outermost ejecta ($v \geq 0.19c$). This is because, in the early time, the photosphere lies at the outermost ejecta layer. The rise in the opacity in the outermost layer causes the luminosity to drop at $t \sim 0.1$ day.

As the ejecta expands further with time, the temperature in the outer layer decreases, crossing the temperature (and ionization) range where the opacities peak. This results in the opacity to decrease and correspondingly the luminosity to rise at $t \sim 0.4$ day. Finally, at around $t \sim 1$ day, the temperature of the outermost layer

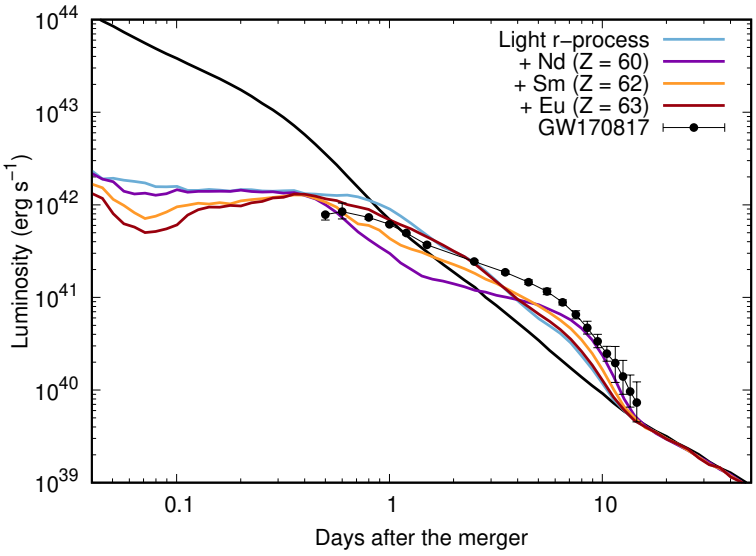

Figure 3.10: The deposited (black curve) and the bolometric luminosity (colored curves) for lanthanide-rich models. The early bolometric luminosity shows a drop in the presence of lanthanides.

of the ejecta drops enough ($T < 10000$ K) so that the peaks of the opacity for the lower-ionized lanthanides starts to appear (see left panel of Figure 3.10). Hence, the luminosities decreases again at $t \sim 1$ day. Therefore, we conclude that even though the opacities for the highly ionized lanthanides are extremely high, it affect the light curves only for a brief period of time ($t \leq 0.4$ day). This behavior indicates the rapid temperature evolution in the ejecta.

The ejecta containing different lanthanides show different extent of drops in the luminosity at different times. For example, the luminosity for the Eu-rich ejecta shows the maximum drop at $t = 0.1$ day, whereas the ejecta containing Nd shows the faintest light curve at $t = 1$ day. The faintness of the light curves are determined by the peak opacities for lanthanides at different temperatures (right panel of Figure 2.10). For instance, at high temperature, i.e., the condition at $t = 0.1$ day, the opacity is maximum for Eu. On the other hand, Nd has the maximum opacity at a low temperature, i.e., the condition at $t = 1$ day. This is why the light curve shapes are different in the presence of the different lanthanides.

The comparison of the bolometric light curve of GW170817 (Waxman et al., 2018) is also shown. The light curve near $t = 1$ day cannot be explained in presence of Nd and Sm in the ejecta. However, the bolometric luminosity in the presence of Eu does not show much difference from the lanthanide-free model. This is because of the different opacity evolution trend in presence of different lanthanides. Note that we have assumed the presence of single lanthanides. However, in the ejecta, the elements are co-produced and hence, the overall light curve will be on fainter side. Hence, the presence of lanthanide cannot explain the light curve of GW170817.

Spectra

We show the typical spectra in the presence of lanthanides at $t = 0.1$ and $t = 1$ days (Figure 3.11). Our result shows almost featureless spectra. Since our atomic data is not accurate to the spectroscopic level and we use the reduced linelist, which affects the detailed spectral feature, we do not attempt to discuss the individual signature of elements. Instead, we note that the spectra rapidly evolves from UV to the optical wavelengths from $t = 0.1$ to $t = 1$ days, which is consistent with the expectation. Such trend of rapid spectral evolution is common in all models.

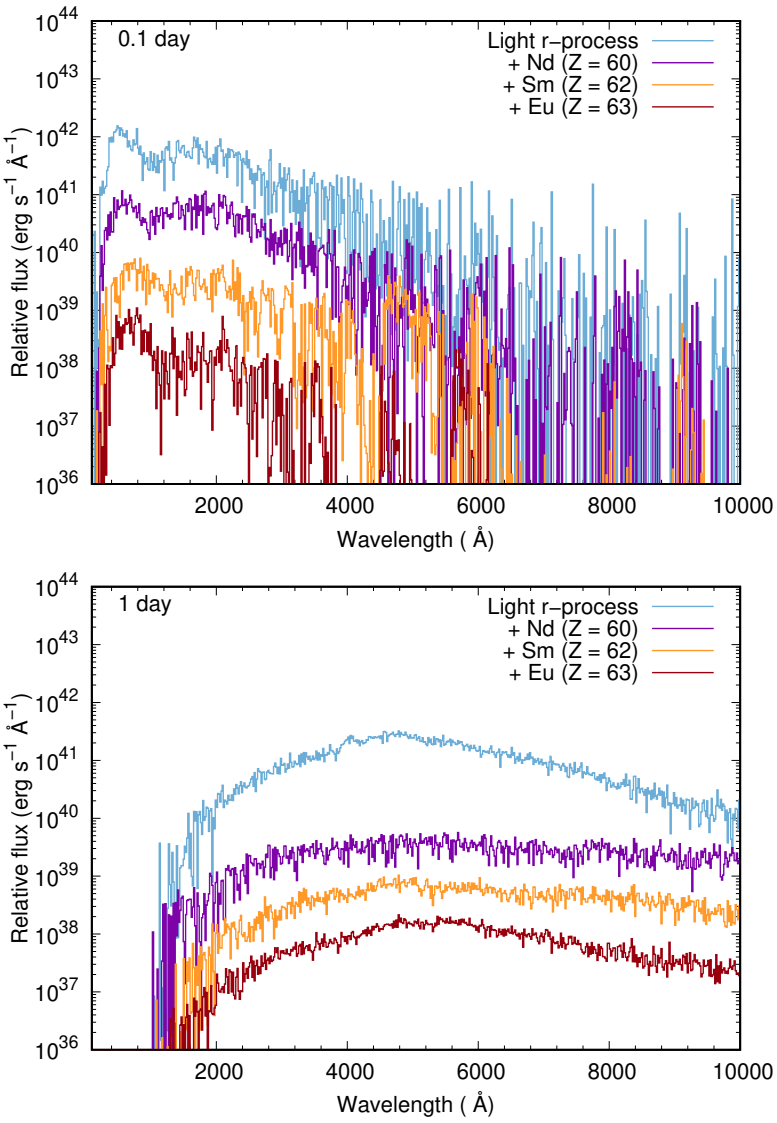

Figure 3.11: The scaled spectra for lanthanide-rich models at $t = 0.1$ day (upper panel) and at $t = 1$ day (bottom panel). The scaling factors are 1000, 100, 10, and 1 for lanthanide-free ejecta, ejecta containing Nd, Sm, and Eu, respectively. The spectra for the lanthanide-free model (cyan curve) are shown for comparison purpose.

Chapter 4

Discussion

We calculate the opacities for the highly ionized (up to XI) r-process elements ($Z = 20 - 88$) starting from the early time ($t \sim 0.1$ day). Using the new opacity, we determine the kilonovae for the lanthanide-rich and lanthanide-free ejecta from neutron star mergers. In this section, we test whether our models can explain the early light curve of GW170817. Moreover, we also discuss the future detection prospects for the kilonovae at early time. Finally, we discuss the validity of the expansion opacity used in our calculations.

4.1 Comparison with GW170817

We compare the multi-color light curves of GW170817 with our models. In the case of GW170817, the observation angle was near to the pole (Abbott et al., 2017a,b; Finstad et al., 2018). Hence, we mainly compare the light curves with our lanthanide-free model, suitable for the polar kilonova. Additionally, we also compare with our lanthanide-rich model to provide an upper limit of lanthanide abundance. Note that we discuss the comparison of early light curves only, which is the focus of the thesis. For discussion on the late kilonova from GW170817, see Kasen et al. (2017); Tanaka et al. (2017); Shibata et al. (2017); Perego et al. (2017); Rosswog et al. (2018); Kawaguchi et al. (2018).

4.1.1 Lanthanide-free model

The light curves for the simple spherical ejecta model with the light r-process abundance show reasonable agreement with the data (Figure 4.1), similar to the bolometric luminosity (Figure 3.6). Therefore, we conclude that the ejecta with only light r-process abundance, i.e., the high Y_e ejecta, can explain the bright UV and blue emission from GW170817 at the early-time.

The velocity range of our model ejecta is suitable for the disk wind ejecta (e.g., Miller et al., 2019a), which are expected to be surrounded by the faster moving dynamical ejecta. Hence, we compare the multi-color light curves for such a scenario with GW170817 data. For such purpose, we show the UV light curves for the fiducial model and the case where $n^{'} = -10$. The UV magnitudes become fainter and decline faster upon the inclusion of a thin layer outside the fiducial model ejecta (Figure

4.2). The UVW1 magnitude of the fiducial model without a thin layer peaks at an absolute magnitude of -16 mag at $t \sim 0.1$ days, whereas that of the model incorporating a thin layer with $n^{'} = -10$ is fainter and reaches a peak of -15.7 mag on a faster timescale ($t \sim 0.1$ days). Note that this has also been pointed out by Kasen et al. (2017).

Here we want to mention that our models assume that the abundance of the outer ejecta are lanthanide-free, same as that of the inner ejecta (the light r-process abundance for $Y_{\rm e} = 0.30 - 0.40$). If the lanthanides are present in the outer ejecta, the UV brightness can be suppressed further. In that case, the kilonova models might not be able to explain the observed early light curve of GW170817 and a heating source other than radioactive decays of r-process elements, such as, β decay luminosity from free neutrons (Metzger et al., 2015; Gottlieb & Loeb, 2020) or some other central power source (Metzger et al., 2008; Yu et al., 2013; Metzger & Fernández, 2014; Matsumoto et al., 2018; Metzger et al., 2018; Li et al., 2018; Wollaeger et al., 2019) might be necessary. Alternatively, the jet-ejecta interaction, which modifies the density structure in the ejecta, can also affect the light curve at early time (Klion et al., 2021; Nativi et al., 2021).

Although it is difficult to draw firm conclusions with the current model, our new atomic opacities create the foundation for the detailed study of the blue kilonova models at an early phase. Investigating the effect of thin layer containing lanthanides remain within the scope of future work.

Note that the earlier works that assumed a constant opacity for the lanthanide-free model also show good agreement for early UV and optical kilonova of GW170817 (Cowperthwaite et al., 2017; Drout et al., 2017; Kasen et al., 2017; Villar et al., 2017). However, we derive detailed atomic opacities, and hence, the opacity is not a free parameter in our work.

4.1.2 Lanthanide-rich model

Figure 4.4 shows the comparison of the light curves for the same simple spherical ejecta model but with the presence of lanthanides. Note that we consider single lanthanide abundance (Nd, Sm, or Eu) can represent the mixture of lanthanides. Our result shows that in presence of Eu, light curve are fainter at $t < 0.2$ days, whereas in presence of Nd, the light curves are not much different from the lanthanide-free model. On the other hand, the light curve is fainter for Nd-rich ejecta at $t \sim 1$ day, whereas Eu-rich ejecta is almost the same with the ejecta containing light r-process. This is similar to the conclusion for the bolometric light curves for different lanthanide-rich models (Figure 3.6) and can be understood from the evolution of the outer layer opacity in the presence of different lanthanides.

The distinguishing feature for lanthanide-rich model at around $t \sim 0.2$ day (for the high temperature opacity peak) cannot be verified with the current observation of GW170817 (optical observation started around $t \sim 0.458$ day). The observation near $t \sim 1$ day, which is mainly due to the low temperarure peak of the lanthanides, cannot be explained if lanthanides are present.

Here we want to mention that the lanthanides are co-produced in the ejecta and the second half of lanthanides ($Z = 64 - 71$) will be present together with the first half elements ($Z = 57 - 63$). Some of the second half lanthanides have higher

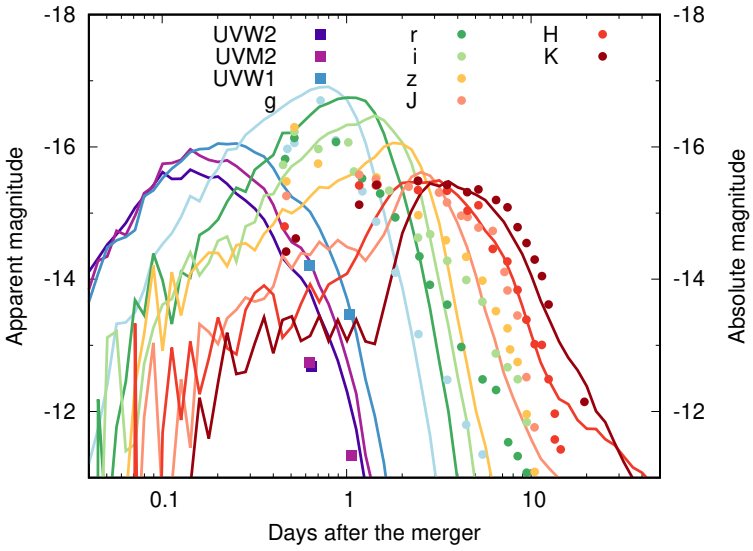

Figure 4.1: Comparison of the multi-color light curves of lanthanide-free model with GW170817. UV data are taken from Evans et al. (2017); Drout et al. (2017) and the other data are compiled by Villar et al. (2017). The GW170817 data are corrected for Galactic extinction with $E(B-V) = 0.1$. © AAS. Reproduced with permission.

complexity, and hence, the overall opacity will be higher in such case (Figure 2.13). Therefore, the overall light curve will be fainter than the model shown here and hence we can conclude that the presence of lanthanides with an amount $X_{\rm La} = 0.1$ can not reproduce the multi-color early light curve of GW170817. This is consistent with previous work (e.g., Kasen et al., 2017).

4.2 Future prospects

Here we discuss the prospects of observing the early kilonova emission as predicted from our results. First we discuss the UV magnitude for lanthanide-free and lanthanide-rich models as derived from our calculation and then we discuss the detectability in future.

Early UV magnitude of lanthanide-free kilonova

Figure 4.4 shows the magnitudes in the three different *Swift* UVOT filters (Roming et al., 2005) for a source at 100 Mpc for different models. The UV brightness of a source at 100 Mpc with lanthanide-free ejecta peaks at $t \sim 0.1$ day, reaching $\sim 19-19.5$ mag depending on different bands. The brightness decreases afterwards, reaching ≥ 22 mag after $t \sim 1$ day. Note that the first UV data of GW170817 are obtained at 16 hours, which is beyond the peak timescale of UV as predicted by our model.

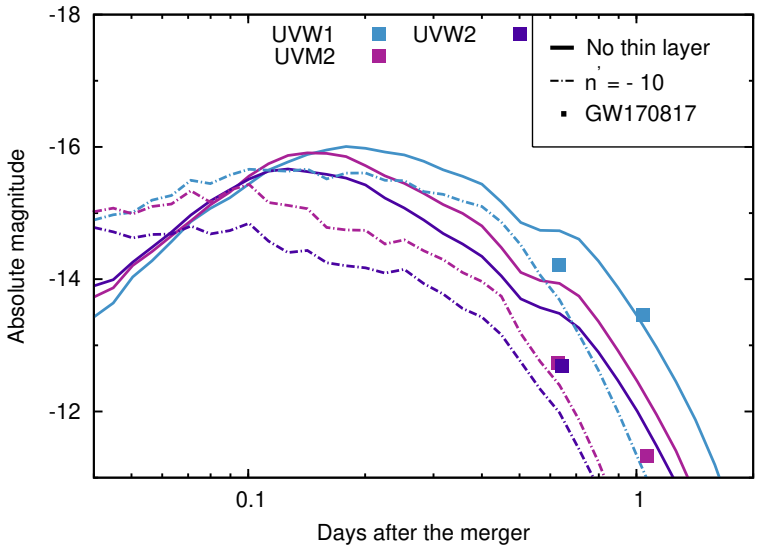

Figure 4.2: The comparison of UV magnitudes between the fiducial model ejecta with simple power law density structure (with a slope $n = -3$), total mass $M_{\rm ej} = 0.05 M_\odot$ with the model with a thin outer layer (with a steeper densit slope $n' = -10$) outside the fiducial ejecta. The abundances in both the outer and the inner layer are light r-process elements. The magnitude becomes fainter by including a thin outer layer. The data of GW170817 data (Evans et al., 2017; Drout et al., 2017) are shown for comparison. © AAS. Reproduced with permission.

Early UV magnitude of lanthanide-rich kilonova

Next we discuss the early UV magnitude for a source at 100 Mpc for lanthanide-rich ejecta. The UV brightness for lanthanide-rich ejecta drops at $t \sim 0.1$ day, reaching $\sim 21 - 22$ mag depending on models. The brightness increases afterwards, reaching ~ 19 mag at $t \sim 0.2$ day, which drops to > 22 mag after $t \sim 1$ day.

The extents of drop and the slope of the light curves are different for the different models. For instance, at $t \sim 0.1$ day, the magnitudes for Eu-rich ejecta are the faintest, whereas Nd-rich ejecta show faintest magnitudes at $t \sim 1$ day. Moreover, the presence of Eu makes the light curve rise faster at $t \sim 0.1$ day, whereas the presence of the Nd makes the light curve fall faster at $t \sim 1$ day. This is because of the differences in the opacity in the outermost layer in the presence of the different lanthanides, as discussed in Chapter 2.

Detectability of early kilonovae

The early UV signals for both lanthanide-free and lanthanide-rich ejecta are bright enough to be detected by *Swift* (with a limiting magnitude of ~ 21 mag for an exposure time of 1000 s, Brown et al., 2014), provided the kilonova is discovered early enough so that the prompt observation can be started. In the next decade, multiple UV missions are proposed, several of which are soon to be launched. For example, we can mention the upcoming wide-field UV satellite ULTRASAT (limiting magnitude of 22.4 mag for 900 s of integration time, Sagiv et al., 2014), DORADO (limiting magnitude of 20.5 mag for 600 s of integration time, Dorsman et al., 2022),

and UVEX (limiting magnitude of 24.5 mag for 900 s of integration time, Kulkarni et al., 2021). UV signal from kilonova at early time are good targets for such satellites.

Future detection of such a kilonova will provide us with the hints to the abundance patterns in the outer layer of the ejecta. This will put important constraints on the nucleosynthesis condition in the neutron star mergers.

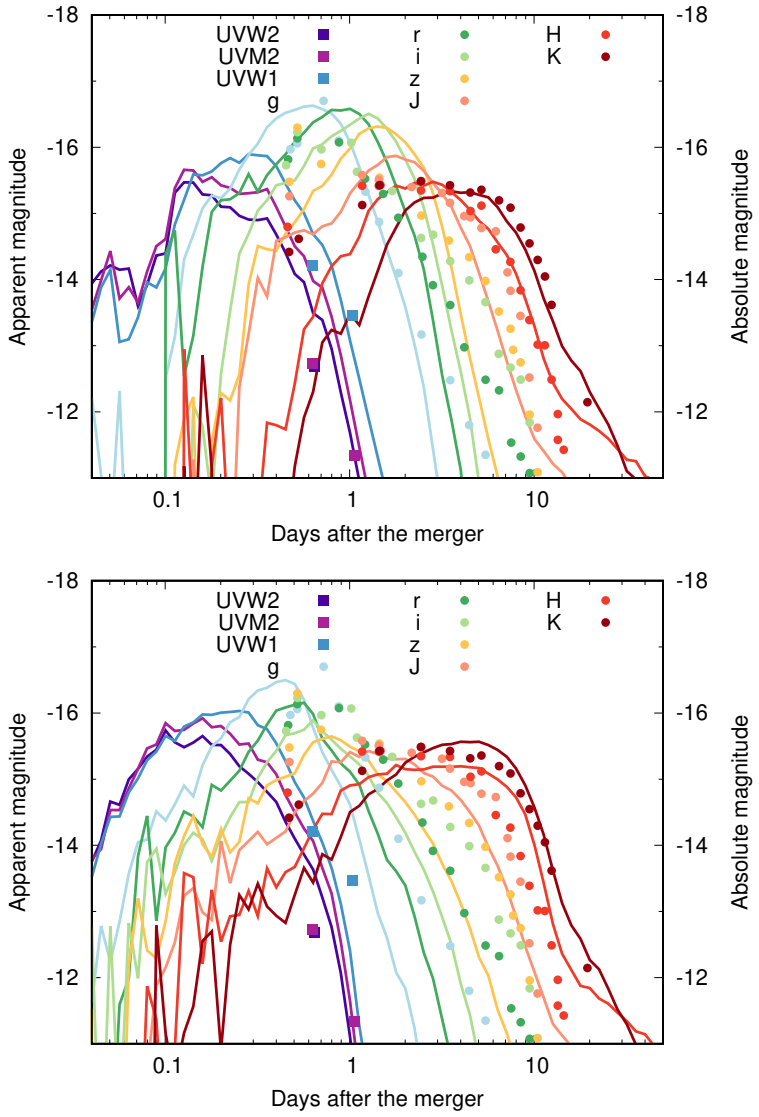

Figure 4.3: Comparison of the multi-color light curves of lanthanide-rich model with GW170817. Here Eu (top) or Nd (bottom) abundance are assumed to represent the mixture of lanthanide abundance in the ejecta. UV data are from Evans et al. (2017); Drout et al. (2017) and the other data are compiled by Villar et al. (2017). The GW170817 data are corrected for Galactic extinction with $E(B-V) = 0.1$.

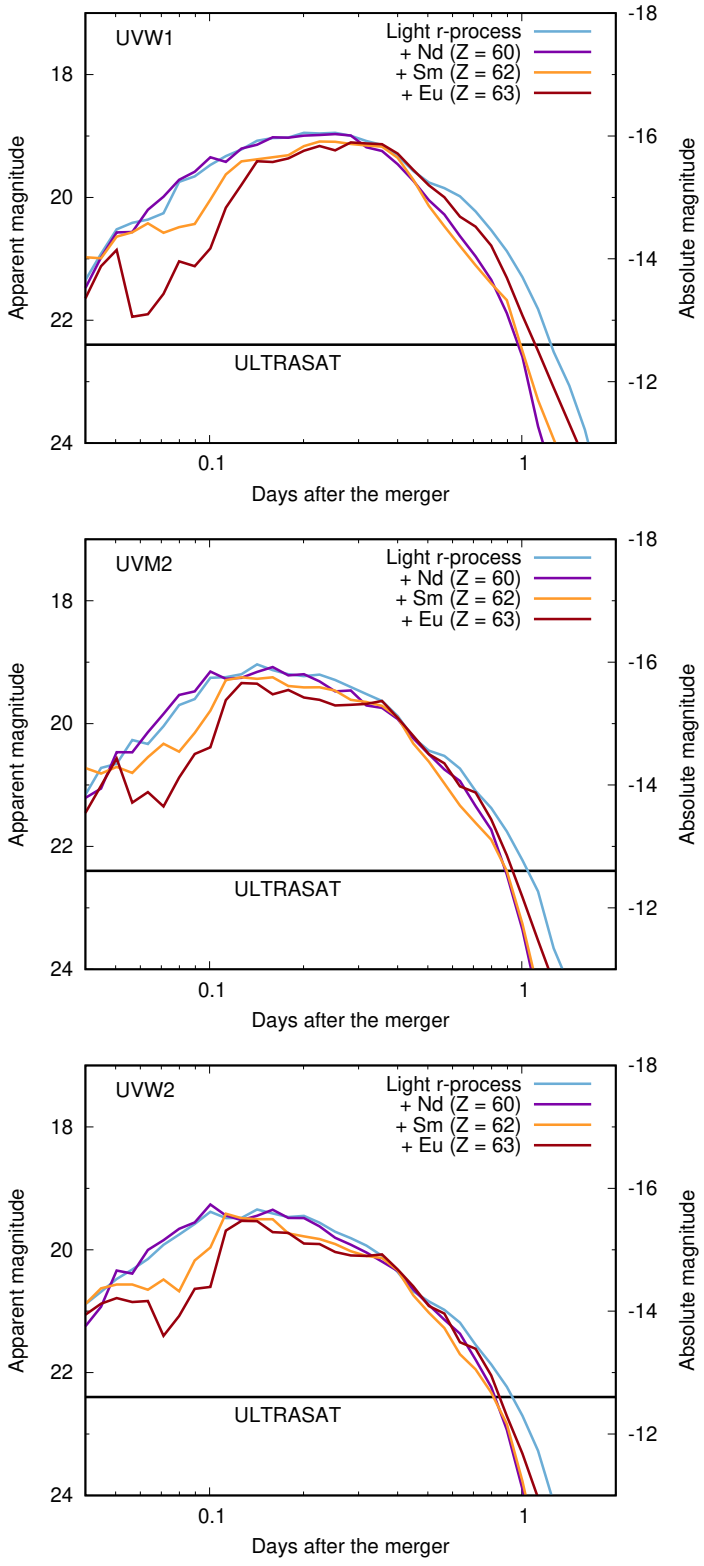

Figure 4.4: Comparison of UV magnitudes between different models for a source at a distance 100 Mpc. The magnitudes are shown for three *Swift* UVOT filters UVW1 (top), UVM2 (middle), and UVW2 (bottom) with the mean wavelengths 2140 Å, 2273 Å, and 2688 Å, respectively (Roming et al., 2005; Brown et al., 2014). The magnitudes drop at $t \sim 0.1$ day in presence of lanthanides.

4.3 Validity of the Sobolev approximation

The expansion opacity at the selected wavelength interval ($\Delta\lambda$) is calculated by taking the cumulative contribution from all the lines inside $\Delta\lambda$. Here it is assumed that the line spacing is greater than the line width. Note that the overlap of weak lines, the number of which is high for r-process elements, happens often. However, if the intrinsic line profiles for strong lines overlap, i.e., if the line spacing ($\Delta\lambda_{\rm line} = \Delta\lambda/N$ for N strong lines inside $\Delta\lambda$) is comparable to the thermal width of the line ($\Delta\lambda_{\rm th}$), the true opacity cannot be calculated using the expansion opacity formalism. Since our calculations show the high number of transitions caused by the high density of the lines (Section 2.3), we check whether the line profiles do not overlap and if the Sobolev approximation is valid.

We define a critical opacity when the thermal width of the line is equal to the line spacing, i.e., $\Delta\lambda_{\rm th} = \Delta\lambda/N = \Delta\lambda_{\rm line}$ by following Kasen et al. (2013). In such cases, the velocity required to redshift the photon between two consecutive lines (Equation (2.8)) can be given by the thermal velocity $v_{\rm th}$:

$$v_{\rm th} = c\frac{\Delta\lambda_{\rm th}}{\lambda} = c\frac{\Delta\lambda}{\lambda}\frac{1}{N}. \tag{4.1}$$

The value of the $v_{\rm th}$ is $\sim 4\,{\rm km\,s^{-1}}$ at the typical temperature $T \sim 10^5$ K at the time $t \sim 0.1$ day using an average atomic mass number of $A = 150$ for the r-process elements. Using Equation (4.1), Equation (2.10), and Equation (2.12), we estimate the critical opacity as follows:

$$\begin{aligned}\kappa_{\rm crit} &= \frac{1}{\rho v_{\rm th} t} \\ &\sim 3\,{\rm cm^2\,g^{-1}}\left(\frac{\rho}{10^{-10}\,{\rm g\,cm^{-3}}}\right)^{-1}\left(\frac{v_{\rm th}}{4\,{\rm km\,s^{-1}}}\right)^{-1}\left(\frac{t}{0.1\,{\rm d}}\right)^{-1}.\end{aligned} \tag{4.2}$$

The critical opacity is independent of the wavelength and it depends on the temperature and density of the ejecta at a particular time. If the expansion opacity exceeds the critical opacity, the intrinsic line spacing is smaller than the line width, i.e., the lines overlap with each other. Then the expansion opacity using the Sobolev approximation for the radiative transfer can not represent the true opacity in the expanding media.

At a time $t \sim 0.1$ day after the neutron star merger, for a density $\rho \sim 10^{-10}\,{\rm g\,cm^{-3}}$, and a temperature of $T \sim 70000$ K, $\kappa_{\rm crit} = 3\,{\rm cm^2\,g^{-1}}$ (Equation (4.2)). The expansion opacity, under the same condition, can reach up to $\kappa_{\rm exp} \sim 1000\,{\rm cm^2\,g^{-1}}$ at far-UV ($\lambda \leq 2000$ Å, Figure 2.10), exceeding the value of the critical opacity. Hence, using the expansion opacity at $t \sim 0.1$ day for lanthanides can not represent the true opacity at far-UV. Consequently, the light curves are possibly affected in the far-UV wavelengths. Nevertheless, our calculation is most likely to remain unaffected at $\lambda \geq 2000$ Å, which is the detection range of the existing UV instruments like *Swift* (Roming et al., 2005). The alternative treatment of opacity calculation and its implication to the early kilonova light curve will be discussed in future work.

Chapter 5

Conclusions

We investigate the early kilonova emission by calculating the atomic opacity for the highly ionized heavy elements. For the atomic calculation, we consider the ionization up to XI, which is the maximum ionization at a typical condition of $T \sim 10^5$ K at $t = 0.1$ day. Using the new opacity, we perform the radiative transfer simulations to calculate the early kilonova. Our work establishes the foundation for the more detailed analysis in future to understand the physics of the neutron star mergers.

Atomic opacity calculation:

Our results and achievements for opacity calculations (Chapter 2) with the new atomic data are summarized as follows:

- We construct the most systematic atomic opacity suitable for the early time for the r-process elements with atomic number of $Z = 20 - 88$.
- We find that the peak opacity for the lanthanide-free ejecta is $\kappa_{\rm exp} \sim 0.5 - 1\,{\rm cm^2\,g^{-1}}$ at $t = 0.1$ day, whereas the same for the lanthanide-rich ejecta can reach up to a high value of $\kappa_{\rm exp} \sim 5000\,{\rm cm^2\,g^{-1}}$.
- We show that the opacity at the photosphere of neutron star merger ejecta evolves quite fast from $t \sim 0.1$ day to $t \sim 1$ day owing to the fast temperature evolution. Hence, the constant opacity assumption in neutron star merger ejecta (used in many previous works for modelling the early kilonova) are not valid.

Kilonova light curves:

We calculate the kilonova light curve (Chapter 3) by considering two different ejecta abundances and performing the radiative transfer simulations, (1) lanthanide-free ejecta with light r-process elements abundance and (2) lanthanide-rich ejecta, where we assume the single lanthanide abundance (Nd, Sm, or Eu with a fraction of $X_{\rm La} = 0.1$) can represent the mixture of the lanthanides. Such lanthanide-free and lanthanide-rich kilonova may replicate the ejecta condition for a kilonova observed at the polar and the equatorial direction.

Our results for light curve calculations for the lanthanide-free ejecta are summarized as follows:

- The spherical ejecta model with an ejecta mass of $M_{\rm ej} = 0.05 M_{\odot}$ gives the bolometric luminosity of $\sim 2 \times 10^{42}\,{\rm erg\,s^{-1}}$ at $t \sim 0.1$ day.
- The expected early UV signals reach $19-19.5$ mag at $t \sim 0.1$ days for sources at 100 Mpc.
- Our model with lanthanide-free ejecta can explain the early blue kilonova observed in the case of the GW170817.

Our results for light curve calculations for the lanthanide-rich ejecta are summarized as follows:

- The bolometric luminosities for lanthanide-rich ejecta at $t \sim 0.1$ day is $L_{\rm bol} \sim 0.5-1\times10^{42}\,{\rm erg\,s^{-1}}$, which is fainter than the lanthanide-free ejecta by a factor of four to two, depending on the models.
- Our results show the UV brightness for lanthanide-rich ejecta drops at $t \sim 0.1$ day, reaching $\sim 21-22$ mag depending on models for a source at ~ 100 Mpc. The brightness increases afterwards, reaching the peak of ~ 19 mag at $t \sim 0.2$ day.
- Our results indicate that in the presence of lanthanides, the early bolometric and multi-color light curves show a brief period of luminosity drop at $t \sim 0.1$ day, which can be a unique detection signature for lanthanide-rich kilonova in future.

Future outlook

We show that it is possible to detect the early kilonovae in both lanthanide-rich and lanthanide-free cases by the existing UV satellite *Swift* (Roming et al., 2005), if the kilonova is discovered early enough (Chapter 4). Also, such kilonovae are good targets for the upcoming wide-field UV satellites like ULTRASAT (Sagiv et al., 2014), DORADO (Dorsman et al., 2022), and UVEX (Kulkarni et al., 2021). Detection of such kilonovae in the early time will provide the abundance pattern in the outer ejecta and can put constraints on the nucleosynthesis condition in the neutron star mergers. Hence, our work will contribute toward understanding *the origin of heavy elements* (see Figure 5.1).

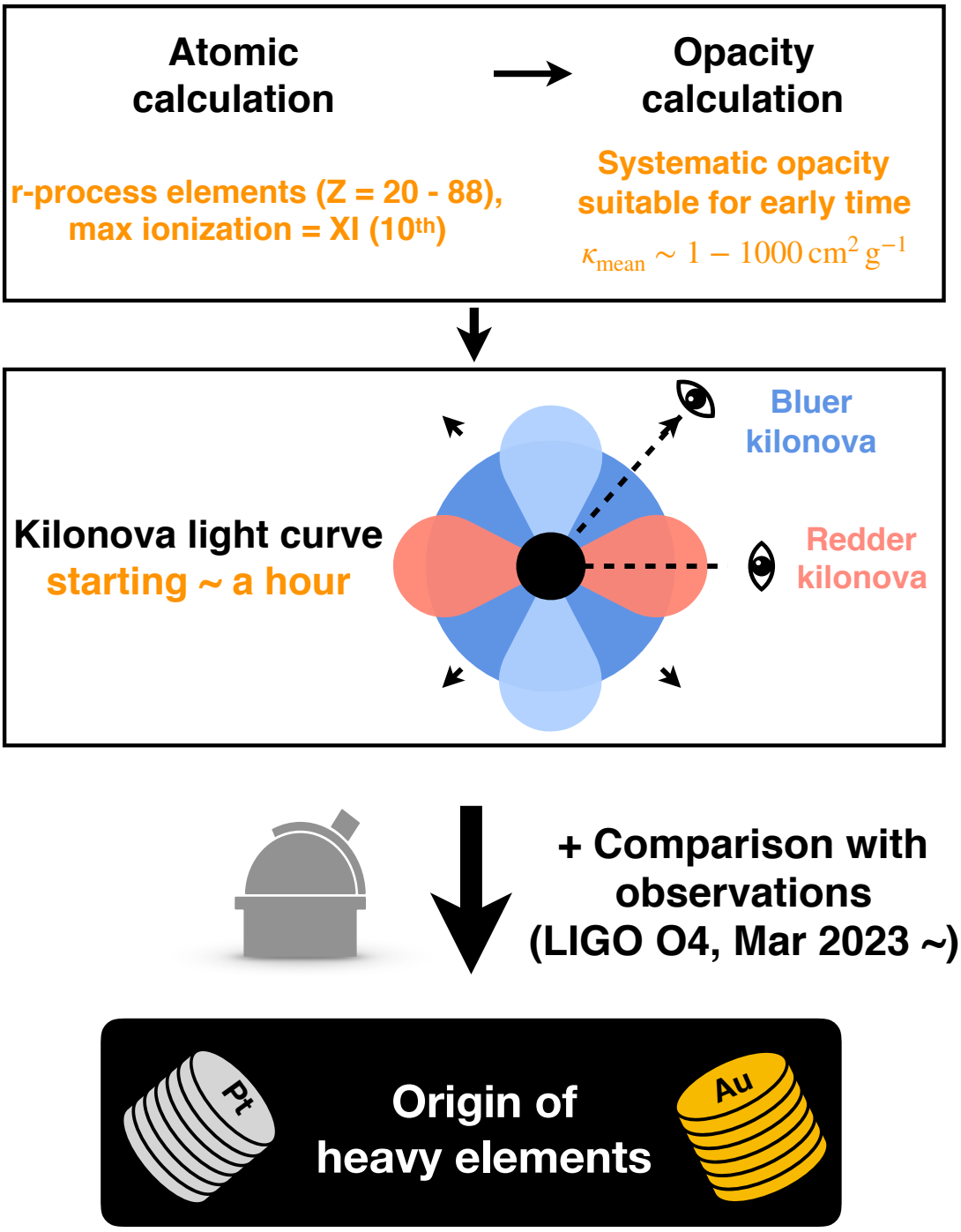

Figure 5.1: The summary of the work in the thesis.

Appendix A

Validity of assumption of local thermal equilibrium (LTE)

We assume the local thermal equillibrium (LTE) to calculate the ionization and excitation by using Saha ionization equation and Boltzmann equation. The neutron star merger ejecta have low density (e.g., $\rho \sim 10^{-10}\,\mathrm{g\,cm^{-3}}$ at $t \sim 0.1$ day after the merger). This low density is not enough to establish LTE via collisional processes alone. Nevertheless, LTE can be established via radiative transitions in the optically thick regions inside the photosphere. Hence, LTE is a valid assumption, especially in the early time when most of the ejecta are optically thick.

The approximation of LTE might be invalid if the ionization and excitation are significantly affected by the non-thermal processes from the radioactive decay, which continuously occur in the neutron star merger ejecta. Kasen et al. (2013) show that such processes do not significantly affect ionization and excitation at $t \geq 1$ day, when the radioactive power released per particle is $\sim 1\,\mathrm{eV\,s^{-1}}$. Since our work focuses on the early time, when the radioactive power release is even higher, we check if non-thermal processes significantly affect ionization and excitation in the early time.

We derive a ballpark estimate of the effect of the non-thermal excitation following Kasen et al. (2013). We assume the radioactive energy release per particle per unit time is $\dot{\epsilon}$ and f is the fraction of the energy that goes into the non-thermal excitation. Then the excitation rate at a transition energy ΔE is

$$R_{\mathrm{nt}} = \frac{f\dot{\epsilon}}{\Delta E}. \tag{A.1}$$

On the other hand, the radioactive excitation rate assuming a blackbody field at a temperature T is:

$$R_{\mathrm{BB}} = B_{12}B_{\nu}(T), \tag{A.2}$$

where B_{12} is the Einstein coefficient. The relative contribution of the two different mechanisms to the excitation can be calculated by using the Einstein relation:

$$\frac{R_{\mathrm{nt}}}{R_{\mathrm{BB}}} \sim \frac{f\dot{\epsilon}}{\Delta E A_{21}}(e^{\frac{\Delta E}{kT}} - 1). \tag{A.3}$$

By using Equation (A.3), we derive the ratio of the non-thermal to thermal excitation rate at $t \sim 0.1$ day by putting the radioactive power released per particle

$\dot{\epsilon}(t \sim 0.1\,\mathrm{day}) \sim 80\,\mathrm{eV\,s^{-1}}$ (Metzger et al., 2010) and the transition energy is $\Delta E \sim 10$ eV at the temperature $T \sim 10^5$ K. We find the ratio is $\leq 10^{-8}$. Similarly, we can derive the non-thermal ionization at the early time. Therefore, we conclude that the effect of non-thermal processes is not significant at the timescale of interest and the LTE approximation can be used. At a later time, when the ejecta expands to become less dense and more optically thin, larger deviation from LTE is expected. For discussion on non-LTE opacity, see Pognan et al., 2022.

Appendix B

Convergence test for opacity

It is important to know if our new atomic data are complete to produce the true estimate of opacity. To test the completeness of our new atomic data, we perform the convergence test on the opacity derived by using the atomic data corresponding to only a subset of configurations for IX ions of lanthanides (Figure B.1). We select the IX ion, which is one of the major contributors to the opacity at high temperatures ($\sim$ 70000 K). This is due to the fact that IX ions for lanthanides have highly dense energy levels. We show the energy level distribution for individual configurations (left panel of Figure B.1) and the Planck mean opacities calculated using a subset of atomic data (right panel of Figure B.1). The thick black curve shows the opacity using all the configurations mentioned in Table D.1 (hereafter called the default configuration set).

The opacities for Eu IX remain unaffected as long as the energy levels belonging to the configurations up to $4f^4\,5p^2\,6p$ are included. This implies that the transitions to or from the energy levels belonging to $4f^4\,5p^2\,7s$ do not have a significant impact on the Planck mean opacity, mostly due to the negligible population in these relatively high energy levels (e.g., the energy levels belonging to $4f^4\,5p^2\,7s$ are > 80 eV, left panel of Figure B.1). However, further removal of energy levels introduces about a factor of ~ 2 difference in the opacity for Eu IX. Similar trends are found for Sm IX. On the other hand, for the case of Nd IX, the opacities are affected up to a factor of ~ 2 if the energy levels belonging to the configurations up to $4f\,5p^2\,6p$ are not included. This is due to relatively low energy levels of the excited configurations in Nd. However, as the number density of the levels is not extremely high for Nd IX, the opacity itself is small, as compared with Eu IX and Sm IX. Hence, we come to the conclusion that our opacities are mostly converged, and further addition of excited configurations will not significantly affect the opacity.

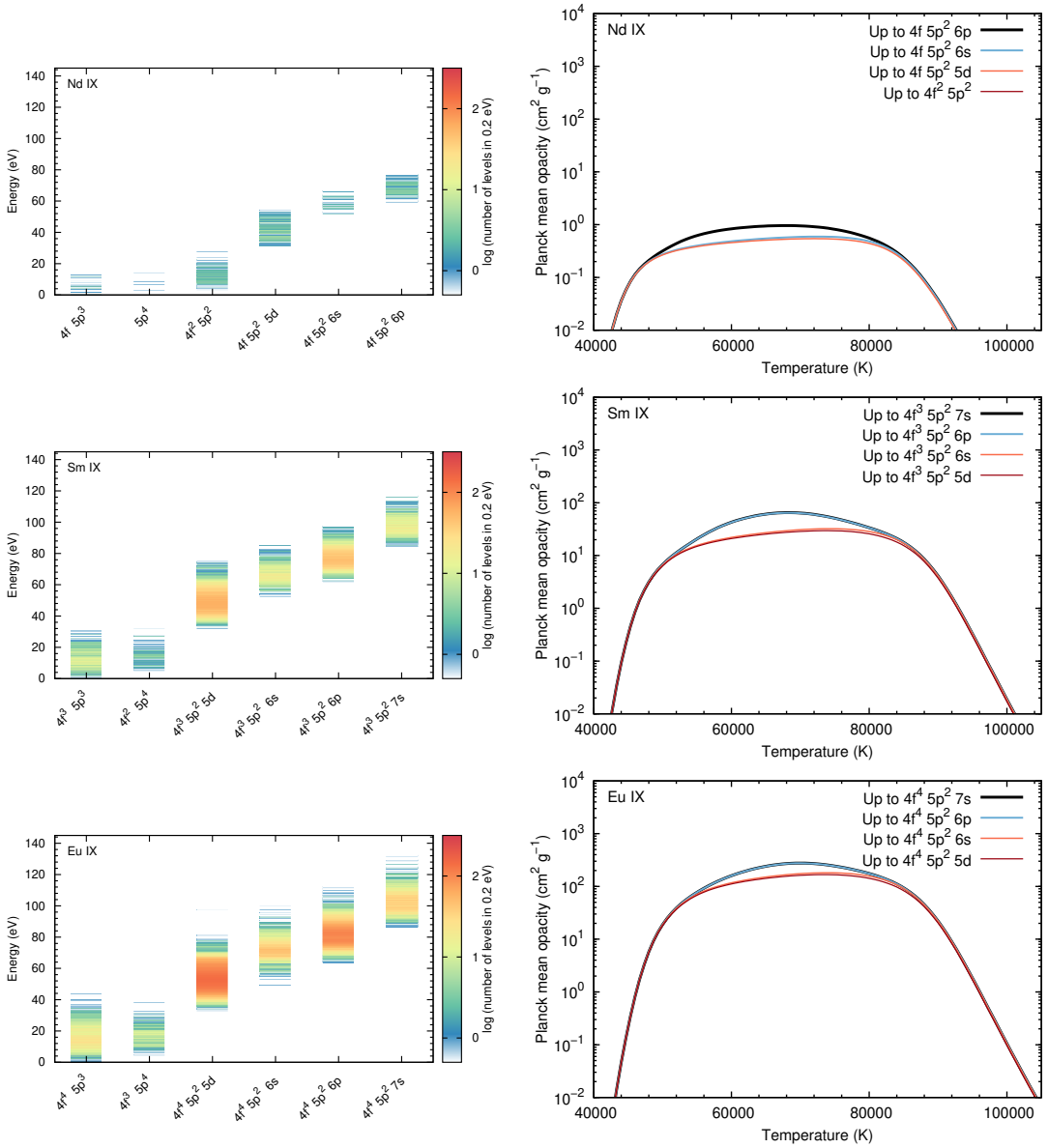

Figure B.1: The energy level distribution within the 0.2 eV energy bin for the individual configurations as obtained from HULLAC (left panel) and the corresponding Planck mean opacities (right panel) for Nd IX, Sm IX, and Eu IX ions (top to the bottom panels). Different colored curves in the right panel represent the opacities calculated by including different subsets of the configurations. See text for details.

Appendix C

Scheme for reduced linelist

The lanthanides in the highly ionized states (> V) have extremely dense energy levels (see Section 2.3). The numbers of transitions can reach as high as $\sim 10^8$ for a single ion in some cases (Table D.1). Such a large linelist makes it impossible to perform the radiative transfer. To make the radiative transfer feasible, we create a reduced linelist by randomly selecting one line out of a chosen ensemble of lines ($n_{\rm sample}$). Our criteria for using the reduced linelist to perform the radiative transfer simulation is that the reduced linelist preserves the statistical properties of the original linelist, i.e., the statistical distributions of the transition wavelengths, radiative transition probabilities, and the statistical weights of the energy levels are preserved. The opacity depends on such statistical properties. Hence, if such properties are conserved, the opacity with the reduced linelist can approximately reproduce the opacity with the full linelist, provided the contribution from the chosen lines is enhanced by a factor of $n_{\rm sample}$.

In our scheme, the expansion opacity with the reduced linelist can be derived as:

$$\kappa_{\rm exp}(\lambda) = \left[\frac{1}{\rho ct}\sum_{l}\frac{\lambda_l}{\Delta\lambda}(1-e^{-\tau_l})\right] \times n_{\rm sample}, \tag{C.1}$$

where the summation is taken over the reduced linelist and we adopt $n_{\rm sample} = 1000$ for the linelist, i.e., we select 1 out of 1000 lines to make the reduced linelist, which is 0.1% of the original linelist. The expansion opacity spectra show a good agreement with the original result, although the opacity becomes noisier at longer wavelengths because of random sampling (left panel of Figure C.1). Nevertheless, the Planck mean opacity shows a perfect match (right panel of Figure C.1). Hence, in conclusion, our reduced linelist preserves the full linelist, and therefore, can be used for the opacity calculation in radiative transfer simulations. Since the opacity spectra become noisier using the reduced linelist, the detailed features of the energy spectra are affected. However, the overall bolometric lightcurve and the broad-band magnitudes are not significantly affected since those are calculated by integrating the energy spectra over a wide wavelength range.

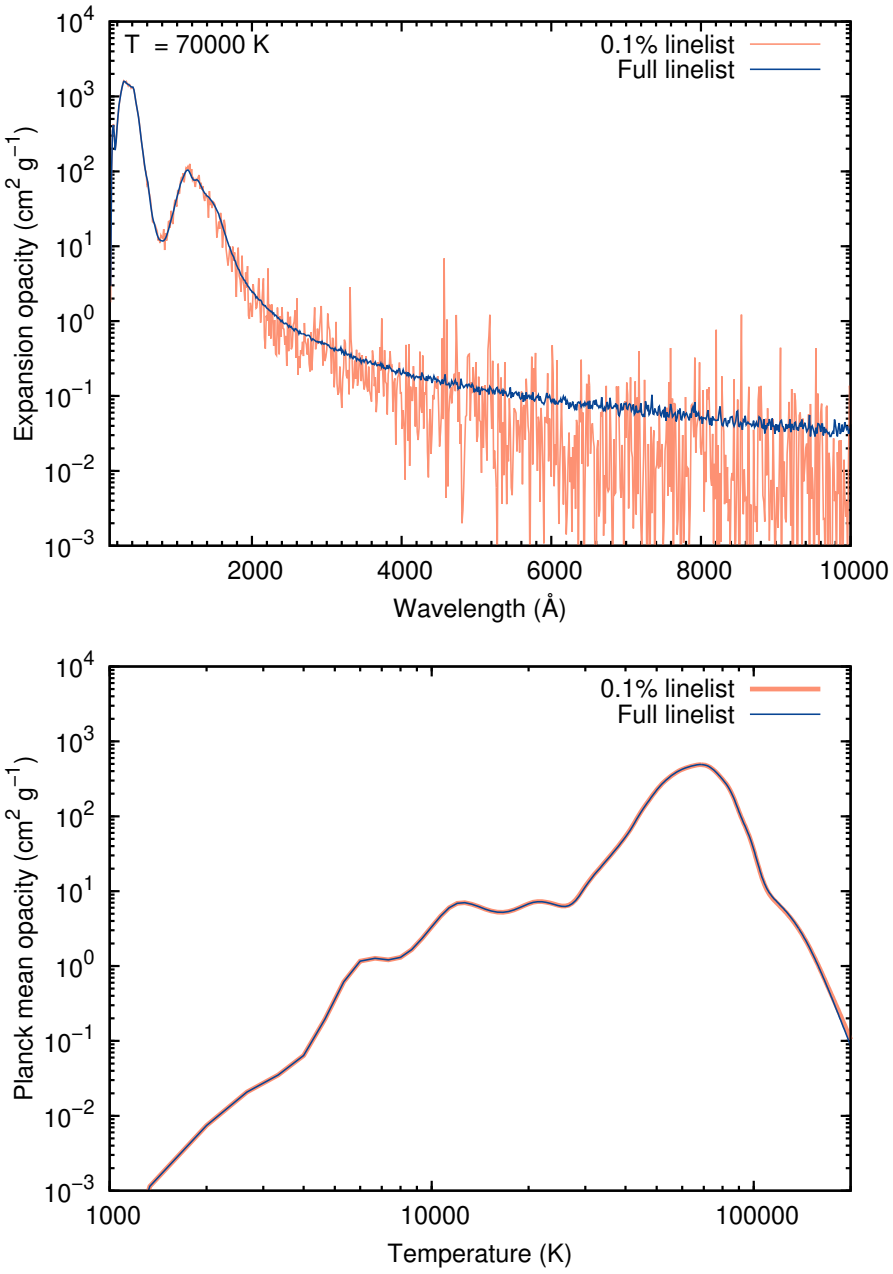

Figure C.1: Comparison between the expansion (left panel) and Planck mean opacities (right panel) derived by using the reduced and the full linelist for the lanthanide element Eu. © AAS. Reproduced with permission.

Appendix D

The configurations used for calculation

Table D.1: The configurations

Ion	Configurations	N_{level}	N_{line}	N^*_{line}
La I	$\mathbf{5d^26s^1}$, $5d^16s^2$, $5d^3$, $5d^16s^16p^1$, $4f^16s^2$, $6s^26p^1$, $5d^26p^1$, $4f^15d^16s^1$, $4f^16s^16p^1$, $5d^27s^1$, $5d^16s^17s^1$, $5d^26d^1$, $5d^27p^1$, $4f^15d^2$, $5d^16s^17p^1$, $6s^28p^1$	414	20619	8229
La II	$\mathbf{5d^2}$, $\mathbf{4f^16s^1}$, $\mathbf{4f^15d^1}$, $5d^16s^1$, $6s^2$, $5d^16p^1$, $6s^16p^1$, $4f^16p^1$	66	553	553
La III	$\mathbf{5p^65d^1}$, $\mathbf{5p^64f^1}$, $5p^66s^1$, $5p^66p^1$, $5p^67s^1$,$5p^66d^1$, $5p^65f^1$, $5p^67p^1$, $5p^68s^1$	15	36	36
La IV	$\mathbf{5p^6}$, $5p^54f^1$, $5p^55d^1$, $5p^56s^1$, $5p^56p^1$, $5p^56d^1$, $5p^57s^1$	55	422	422
La V	$\mathbf{5p^5}$, $5p^44f^1$, $5p^46s^1$, $5p^45d^1$, $5p^46p^1$	89	1124	1124
La VI	$\mathbf{5p^4}$, $5p^34f^1$, $5p^36s^1$, $5p^35d^1$, $5p^36p^1$	121	1937	1937
La VII	$\mathbf{5p^3}$, $5p^24f^1$, $5p^26s^1$, $5p^25d^1$, $5p^26p^1$	92	1208	1208
La VIII	$\mathbf{5p^2}$, $5p^14f^1$, $5p^16s^1$, $5p^15d^1$, $5p^16p^1$	43	254	254
La IX	$\mathbf{5p^15s^2}$, $5p^15s^14f^1$, $5p^15s^16s^1$, $5p^15s^15d^1$, $5p^15s^16p^1$	74	808	808
La X	$\mathbf{5s^2}$, $5s^14f^1$, $5s^16s^1$, $5s^15d^1$, $5s^16p^1$	15	30	30
La XI	$\mathbf{5s^14d^{10}}$, $4d^{10}4f^1$, $4d^{10}6s^1$, $4d^{10}5d^1$, $4d^{10}6p^1$	8	10	10
Ce I	$\mathbf{4f^26s^2}$, $4f^15d^16s^2$, $4f^15d^26s^1$, $4f^25d^16s^1$, $4f^15d^16s^16p^1$, $4f^15d^3$, $4f^16s^26p^1$, $4f^26s^16p^1$, $4f^15d^26p^1$, $4f^25d^2$	1920	293131	150839
Ce II	$\mathbf{5d^24f^1}$, $\mathbf{4f^26s^1}$, $\mathbf{4f^25d^1}$, $4f^15d^16s^1$, $4f^16s^2$, $4f^15d^16p^1$, $4f^26p^1$, $4f^16s^16p^1$	459	22375	22375
Ce III	$\mathbf{4f^2}$, $4f^15d^1$, $4f^16s^1$, $5d^2$, $4f^16p^1$, $5d^16s^1$, $4f^16d^1$, $4f^17s^1$, $5d^16p^1$, $4f^15f^1$, $4f^17p^1$, $4f^18s^1$, $4f^17d^1$, $4f^16f^1$, $4f^15g^1$, $6p^2$, $5d^16d^1$	237	6244	5556
Ce IV	$\mathbf{5p^64f^1}$, $5p^65d^1$, $5p^66s^1$, $5p^66p^1$, $5p^66d^1$, $5p^67s^1$, $5p^65f^1$, $5p^67d^1$	14	31	31

Continued on next page

Table D.1 – *Continued from previous page*

Ion	Configurations	N_{level}	N_{line}	N^*_{line}
Ce V	**5p^6**, $4f^2 5p^4$, $4f^1 5p^5$, $5p^5 6s^1$, $5p^5 6p^1$, $5p^5 5d^1$	210	1274	1274
Ce VI	**5p^5**, $4f^2 5p^3$, $4f^1 5p^4$, $5p^4 6s^1$, $5p^4 6p^1$, $5p^4 5d^1$	310	4420	4420
Ce VII	**5p^4**, $4f^2 5p^2$, $4f^1 5p^3$, $5p^3 6s^1$, $5p^3 6p^1$, $5p^3 5d^1$	292	5233	5233
Ce VIII	**5p^3**, $4f^2 5p^1$, $4f^1 5p^2$, $5p^2 6s^1$, $5p^2 6p^1$, $5p^2 5d^1$	161	2271	2271
Ce IX	**5p^2**, $4f^1 5p^1$, $5p^1 6s^1$, $5p^1 6p^1$, $5p^1 5d^1$, $5p^1 7s^1$	47	315	315
Ce X	**5p^{1}4d^{10}**, $4d^{10} 7s^1$, $4d^{10} 4f^1$, $4d^{10} 6s^1$, $4d^{10} 6p^1$, $4d^{10} 5d^1$	10	17	17
Ce XI	**4d^{10}5s^2**, $4d^{10} 5s^1 7s^1$, $4d^{10} 5s^1 4f^1$, $4d^{10} 5s^1 6s^1$, $4d^{10} 5s^1 6p^1$, $4d^{10} 5s^1 5d^1$	17	36	36
Pr I	**4f^{3}6s^2**, **4f^{3}6s^{1}5d^1**, **4f^{3}6s^{1}6p^1**, **4f^{3}6s^{1}7s^1**, **4f^{3}6s^{1}8s^1**, $4f^2 6s^2 5d^1$, $4f^2 6s^2 6p^1$, $4f^2 5d^2 6s^1$, $4f^2 5d^2 6p^1$, $4f^2 5d^1 6s^1 6p^1$	6516	2715879	663287
Pr II	**4f^{3}6s^1**, **4f^{3}5d^1**, $4f^2 5d^2$, $4f^2 5d^1 6s^1$, $4f^3 6p^1$, $4f^2 5d^1 6p^1$	2007	364325	346451
Pr III	**4f^3**, $4f^2 5d^1$, $4f^2 6s^1$, $4f^2 6p^1$, $4f^1 5d^2$, $4f^1 5d^1 6s^1$, $4f^2 7s^1$, $4f^2 6d^1$, $4f^2 5f^1$, $4f^2 8s^1$	653	42001	41920
Pr IV	**4f^2**, $4f^1 5d^1$, $4f^1 6s^1$, $4f^1 6p^1$, $5d^2$, $4f^1 6d^1$, $5d^1 6p^1$	90	926	926
Pr V	**4f^{1}5p^6**, $5p^6 7s^1$, $5p^6 7p^1$, $5p^6 6s^1$, $5p^6 6p^1$, $5p^6 5d^1$	10	17	17
Pr VI	**5p^6**, $5p^5 4f^1$, $5p^5 7p^1$, $5p^5 6s^1$, $5p^5 6p^1$, $5p^5 5d^1$	49	317	317
Pr VII	**5p^5**, $5p^4 4f^1$, $5p^4 7p^1$, $5p^4 6s^1$, $5p^4 6p^1$, $5p^4 5d^1$	110	1634	1634
Pr VIII	**5p^4**, $5p^3 4f^1$, $5p^3 7p^1$, $5p^3 6s^1$, $5p^3 6p^1$, $5p^3 5d^1$	149	2771	2771
Pr IX	**5p^3**, $5p^2 4f^1$, $5p^2 7p^1$, $5p^2 6s^1$, $5p^2 6p^1$, $5p^2 5d^1$	113	1718	1718
Pr X	**5p^2**, $4f^2$, $5p^1 4f^1$, $5p^1 6s^1$, $5p^1 6p^1$, $5p^1 5d^1$	56	337	337
Pr XI	**5p^{1}5s^2**, $5s^2 4f^1$, $5s^2 7p^1$, $5s^2 6s^1$, $5s^2 6p^1$, $5s^2 5d^1$	11	18	18
Nd I	**4f^{4}6s^2**, **4f^{4}6s^{1}5d^1**, **4f^{4}6s^{1}6p^1**, **4f^{4}6s^{1}7s^1**, **4f^{4}6s^{1}8s^1**, $4f^3 5d^1 6s^2$, $4f^3 5d^2 6s^1$, $4f^3 5d^1 6s^1 6p^1$	12215	11784660	37121
Nd II	**4f^{4}6s^1**, **4f^{4}5d^1**, $4f^3 5d^2$, $4f^3 5d^1 6s^1$, $4f^4 6p^1$, $4f^3 5d^1 6p^1$, $4f^3 6s^1 6p^1$	6888	3947992	2281283
Nd III	**4f^4**, $4f^3 5d^1$, $4f^3 6s^1$, $4f^3 6p^1$, $4f^2 5d^2$, $4f^2 5d^1 6s^1$, $4f^2 5d^1 6p^1$, $4f^2 6s^1 6p^1$	2252	458161	225413
Nd IV	**4f^3**, $4f^2 5d^1$, $4f^2 6s^1$, $4f^2 6p^1$, $4f^1 5d^2$, $4f^1 5d^1 6s^1$, $4f^1 5d^1 6p^1$	474	23864	15982
Nd V	**4f^{2}5p^6**, $4f^3 5p^5$, $4f^1 5p^6 7p^1$, $4f^1 5p^6 6s^1$, $4f^1 5p^6 6p^1$, $4f^1 5p^6 5d^1$	303	2811	2811
Nd VI	**4f^{1}5p^6**, $4f^2 5p^5$, $5p^6 7p^1$, $5p^6 6s^1$, $5p^6 6p^1$, $5p^6 5d^1$	78	96	96

Continued on next page

Table D.1 – *Continued from previous page*

Ion	Configurations	N_{level}	N_{line}	N^*_{line}
Nd VII	$\mathbf{5p^6}$, $5p^4 4f^2$, $5p^5 4f^1$, $5p^5 6s^1$, $5p^5 6p^1$, $5p^5 5d^1$	210	1274	1274
Nd VIII	$\mathbf{5p^5}$, $4f^1 5p^4$, $4f^2 5p^3$, $4f^1 5p^3 6s^1$, $4f^1 5p^3 6p^1$, $4f^1 5p^3 5d^1$	926	96706	96706
Nd IX	$\mathbf{4f^1 5p^3}$, $5p^4$, $5p^2 4f^2$, $4f^1 5p^2 6s^1$, $4f^1 5p^2 6p^1$, $4f^1 5p^2 5d^1$	730	59206	59206
Nd X	$\mathbf{4f^1 5p^2}$, $5p^3$, $4f^2 5p^1$, $4f^1 5p^1 6s^1$, $4f^1 5p^1 6p^1$, $4f^1 5p^1 5d^1$	312	11561	11561
Nd XI	$\mathbf{5p^1 4f^1}$, $5p^2$, $4f^2$, $5p^1 6s^1$, $5p^1 6p^1$, $5p^1 5d^1$	56	337	337
Pm I	$\mathbf{4f^5 6s^2}$, $\mathbf{4f^5 6s^1 5d^1}$, $\mathbf{4f^5 6s^1 6p^1}$, $\mathbf{4f^5 6s^1 7s^1}$, $4f^4 6s^2 5d^1$, $4f^4 6s^1 5d^2$	16294	17038373	321675
Pm II	$\mathbf{4f^5 6s^1}$, $4f^5 5d^1$, $4f^5 6p^1$, $4f^4 6s^1 6p^1$, $4f^4 6s^1 5d^1$, $4f^4 5d^1 6p^1$	12372	9176295	3243150
Pm III	$\mathbf{4f^5}$, $4f^4 5d^1$, $4f^4 6s^1$, $4f^4 6p^1$	1994	320633	317305
Pm IV	$\mathbf{4f^4}$, $4f^3 5d^1$, $4f^3 6s^1$, $4f^3 6p^1$	817	57765	57765
Pm V	$\mathbf{4f^3 5p^6}$, $4f^4 5p^5$, $4f^3 5p^5 5d^1$, $4f^3 5p^5 6s^1$, $4f^3 5p^5 6p^1$, $4f^3 5p^5 7p^1$, $4f^3 5p^5 7s^1$, $4f^3 5p^5 6d^1$	8856	6533898	6036921
Pm VI	$\mathbf{4f^2 5p^6}$, $4f^3 5p^5$, $4f^2 5p^5 5d^1$, $4f^2 5p^5 6s^1$, $4f^2 5p^5 6p^1$, $4f^2 5p^5 7p^1$, $4f^2 5p^5 7s^1$, $4f^2 5p^5 6d^1$	2583	613722	613722
Pm VII	$\mathbf{4f^2 5p^5}$, $4f^3 5p^4$, $4f^2 5p^4 5d^1$, $4f^2 5p^4 6s^1$, $4f^2 5p^4 6p^1$, $4f^2 5p^4 7p^1$, $4f^2 5p^4 7s^1$, $4f^2 5p^4 6d^1$	6286	3647090	3647090
Pm VIII	$\mathbf{4f^2 5p^4}$, $4f^3 5p^3$, $4f^2 5p^3 5d^1$, $4f^2 5p^3 6s^1$, $4f^2 5p^3 6p^1$, $4f^2 5p^3 7p^1$, $4f^2 5p^3 7s^1$, $4f^2 5p^3 6d^1$	8479	6488816	6488816
Pm IX	$\mathbf{4f^2 5p^3}$, $4f^3 5p^2$, $4f^2 5p^2 5d^1$, $4f^2 5p^2 6s^1$, $4f^2 5p^2 6p^1$, $4f^2 5p^2 7p^1$, $4f^2 5p^2 7s^1$, $4f^2 5p^2 6d^1$	6438	3865322	3865322
Pm X	$\mathbf{4f^2 5p^2}$, $4f^3 5p^1$, $4f^2 5p^1 5d^1$, $4f^2 5p^1 6s^1$, $4f^2 5p^1 6p^1$, $4f^2 5p^1 7p^1$, $4f^2 5p^1 7s^1$, $4f^2 5p^1 6d^1$	2741	706348	706348
Pm XI	$\mathbf{4f^2 5p^1}$, $4f^3$, $4f^2 5d^1$, $4f^2 6s^1$, $4f^2 6p^1$, $4f^2 7p^1$, $4f^2 7s^1$, $4f^2 6d^1$	510	26228	26228
Sm I	$\mathbf{4f^6 6s^2}$, $\mathbf{4f^6 6s^1 5d^1}$, $\mathbf{4f^6 6s^1 6p^1}$, $\mathbf{4f^6 6s^1 7s^1}$, $4f^5 5d^1 6s^2$, $4f^5 5d^2 6s^1$	28221	43903717	54329
Sm II	$\mathbf{4f^6 6s^1}$, $\mathbf{4f^7}$, $4f^6 5d^1$, $4f^6 6p^1$, $4f^5 5d^1 6s^1$	9030	5842197	1459980
Sm III	$\mathbf{4f^6}$, $4f^5 5d^1$, $4f^5 6s^1$, $4f^5 6p^1$	3737	1045697	985731
Sm IV	$\mathbf{4f^5}$, $4f^4 5d^1$, $4f^4 6s^1$, $4f^4 6p^1$	1994	320633	320091
Sm V	$\mathbf{4f^4 5p^6}$, $4f^5 5p^5$, $4f^3 5p^6 6s^1$, $4f^3 5p^6 6p^1$, $4f^3 5p^6 5d^1$, $4f^3 5p^6 7s^1$	2067	283093	283093
Sm VI	$\mathbf{4f^3 5p^6}$, $4f^4 5p^5$, $4f^3 5p^5 6s^1$, $4f^3 5p^5 6p^1$, $4f^3 5p^5 5d^1$, $4f^3 5p^5 7s^1$	5230	2288568	2288568
Sm VII	$\mathbf{4f^3 5p^5}$, $4f^2 5p^6$, $4f^3 5p^4 6s^1$, $4f^3 5p^4 6p^1$, $4f^3 5p^4 5d^1$, $4f^3 5p^4 7s^1$	11589	9998002	9998002
Sm VIII	$\mathbf{4f^3 5p^4}$, $4f^2 5p^5$, $4f^3 5p^3 6s^1$, $4f^3 5p^3 6p^1$, $4f^3 5p^3 5d^1$, $4f^3 5p^3 7s^1$	15567	18619221	18619221
Sm IX	$\mathbf{4f^3 5p^3}$, $4f^2 5p^4$, $4f^3 5p^2 6s^1$, $4f^3 5p^2 6p^1$, $4f^3 5p^2 5d^1$, $4f^3 5p^2 7s^1$	12293	11835344	11835344
Sm X	$\mathbf{4f^3 5p^2}$, $4f^2 5p^3$, $4f^3 5p^1 6s^1$, $4f^3 5p^1 6p^1$, $4f^3 5p^1 5d^1$, $4f^3 5p^1 7s^1$	5388	2497192	2497192

Continued on next page

Table D.1 – *Continued from previous page*

Ion	Configurations	N_{level}	N_{line}	N^*_{line}
Sm XI	**$4f^35p^1$**, $4f^25p^2$, $4f^36s^1$, $4f^36p^1$, $4f^35d^1$, $4f^37s^1$	1205	130432	130432
Eu I	**$4f^76s^2$**, $4f^75d^16s^1$, $4f^76s^16p^1$, $4f^65d^16s^2$, $4f^75d^16p^1$, $4f^76s^17s^1$, $4f^65d^26s^1$, $4f^75d^2$, $4f^76s^17p^1$, $4f^76s^16d^1$, $4f^76s^18s^1$, $4f^76s^15f^1$, $4f^76s^18p^1$, $4f^76s^17d^1$, $4f^76p^2$	103229	741430825	4101
Eu II	**$4f^76s^1$**, $4f^75d^1$, $4f^76p^1$, $4f^65d^16s^1$, $4f^65d^2$	22973	21396542	910949
Eu III	**$4f^7$**, $4f^65d^1$, $4f^66s^1$, $4f^66p^1$	5323	2073702	1651778
Eu IV	**$4f^6$**, $4f^55d^1$, $4f^56s^1$, $4f^56p^1$	3737	1045697	1045697
Eu V	**$4f^55p^6$**, $4f^65p^5$, $4f^45p^66s^1$, $4f^45p^66p^1$, $4f^45p^65d^1$, $4f^45p^67s^1$	3897	1140035	1137991
Eu VI	**$4f^45p^6$**, $4f^55p^5$, $4f^45p^56s^1$, $4f^45p^56p^1$, $4f^45p^55d^1$, $4f^45p^57s^1$	13065	12823350	12819025
Eu VII	**$4f^45p^5$**, $4f^35p^6$, $4f^45p^46s^1$, $4f^45p^46p^1$, $4f^45p^45d^1$, $4f^45p^47s^1$	29465	60643899	60636013
Eu VIII	**$4f^45p^4$**, $4f^35p^5$, $4f^45p^36s^1$, $4f^45p^36p^1$, $4f^45p^35d^1$, $4f^45p^37s^1$	40241	113753012	113745357
Eu IX	**$4f^45p^3$**, $4f^35p^4$, $4f^45p^26s^1$, $4f^45p^26p^1$, $4f^45p^25d^1$, $4f^45p^27s^1$	31393	73355941	73355941
Eu X	**$4f^45p^2$**, $4f^35p^3$, $4f^35p^26s^1$, $4f^35p^16s^2$, $4f^45p^16s^1$, $4f^45p^16p^1$, $4f^45p^15d^1$, $4f^45p^17s^1$	15515	18807502	18787178
Eu XI	**$4f^45p^1$**, $4f^35p^2$, $4f^46s^1$, $4f^46p^1$, $4f^45d^1$, $4f^47s^1$	3204	853861	853861
Gd I	**$4f^75d^16s^2$**, $4f^75d^26s^1$, $4f^86s^2$, $4f^76s^26p^1$, $4f^75d^16s^16p^1$, $4f^75d^3$	103013	703084537	31461
Gd II	**$4f^75d^16s^1$**, **$4f^76s^2$**, **$4f^75d^2$**, $4f^86s^1$, $4f^85d^1$, $4f^76s^16p^1$, $4f^75d^16p^1$, $4f^86p^1$	46733	158102968	4161867
Gd III	**$4f^8$**, $4f^75d^1$, $4f^76s^1$, $4f^76p^1$, $4f^77s^1$	6637	2999281	1547749
Gd IV	**$4f^7$**, $4f^65d^1$, $4f^66s^1$, $4f^66p^1$	5323	2073702	2023286
Gd V	**$4f^65p^6$**, $4f^75p^5$, $4f^55p^65d^1$, $4f^55p^66s^1$, $4f^55p^66p^1$	5665	2403983	2403983
Gd VI	**$4f^55p^6$**, $4f^65p^5$, $4f^55p^55d^1$, $4f^55p^56s^1$, $4f^55p^56p^1$	21926	35616475	35616475
Gd VII	**$4f^55p^5$**, $4f^45p^6$, $4f^55p^45d^1$, $4f^55p^46s^1$, $4f^55p^46p^1$	50969	180288431	180288431
Gd VIII	**$4f^55p^4$**, **$4f^45p^5$**, $4f^65p^3$, $4f^55p^36s^1$, $4f^55p^36p^1$	38760	73593381	73593381
Gd IX	**$4f^55p^3$**, $4f^45p^4$, $4f^55p^25d^1$, $4f^55p^26s^1$, $4f^55p^26p^1$	55029	220240570	220240570
Gd X	**$4f^45p^3$**, **$4f^55p^2$**, $4f^55p^15d^1$, $4f^55p^16s^1$, $4f^55p^16p^1$, $4f^55p^17s^1$	27187	55999215	55999215
Gd XI	**$4f^55p^1$**, $4f^45p^2$, $4f^55d^1$, $4f^56s^1$, $4f^56p^1$, $4f^35p^3$	6915	3359449	3359449
Tb I	**$4f^96s^2$**, $4f^85d^16s^2$, $4f^85d^26s^1$, $4f^86s^26p^1$, $4f^96s^16p^1$, $4f^85d^16s^16p^1$, $4f^95d^16s^1$	65817	312984119	492499
Tb II	**$4f^96s^1$**, $4f^85d^16s^1$, $4f^86s^2$, $4f^85d^2$, $4f^95d^1$	19854	11978694	3279198
Tb III	**$4f^9$**, $4f^85d^1$, $4f^86s^1$, $4f^86p^1$	5194	1943961	1516250
Tb IV	**$4f^8$**, $4f^75d^1$, $4f^76s^1$, $4f^76p^1$	5983	2545975	2330682
Tb V	**$4f^75p^6$**, **$4f^85p^5$**, $4f^65p^65d^1$, $4f^65p^66s^1$, $4f^65p^66p^1$, $4f^65p^66d^1$, $4f^65p^67s^1$, $4f^65p^67p^1$, $4f^95p^4$	14872	16965765	13717001
Tb VI	**$4f^65p^6$**, **$4f^75p^5$**, $4f^65p^55d^1$, $4f^65p^56s^1$, $4f^65p^56p^1$, $4f^65p^56d^1$, $4f^65p^57s^1$, $4f^65p^57p^1$, $4f^85p^4$	65376	308013551	292972426
Tb VII	**$4f^65p^5$**, **$4f^75p^4$**, $4f^65p^45d^1$, $4f^65p^46s^1$, $4f^65p^46p^1$, $4f^65p^47p^1$	103141	783718762	770562843

Continued on next page

Table D.1 – *Continued from previous page*

Ion	Configurations	N_{level}	N_{line}	N^*_{line}
Tb VIII	$\mathbf{4f^6 5p^4}$, $\mathbf{4f^5 5p^5}$, $4f^6 5p^3 5d^1$, $4f^6 5p^3 6s^1$, $4f^6 5p^3 6p^1$, $4f^7 5p^3 !2n^d t^{rial}$	108155	827860706	82782424
Tb IX	$\mathbf{4f^6 5p^3}$, $\mathbf{4f^5 5p^4}$, $4f^6 5p^2 5d^1$, $4f^6 5p^2 6s^1$, $4f^6 5p^2 6p^1$, $4f^7 5p^2$	85367	529201954	52910542
Tb X	$\mathbf{4f^6 5p^2}$, $\mathbf{4f^5 5p^3}$, $4f^6 5p^1 5d^1$, $4f^6 5p^1 6s^1$, $4f^6 5p^1 6p^1$, $4f^6 5p^1 7p^1$, $4f^6 5p^1 7s^1$, $4f^6 5p^1 6d^1$, $4f^7 5p^1$	68899	347094944	34706673
Tb XI	$\mathbf{4f^6 5p^1}$, $\mathbf{4f^5 5p^2}$, $4f^6 5d^1$, $4f^6 6s^1$, $4f^6 6p^1$, $4f^6 7p^1$, $4f^6 7s^1$, $4f^6 6d^1$, $4f^7$	14872	16982008	1698216
Dy I	$\mathbf{4f^{10} 6s^2}$, $4f^9 5d^1 6s^2$, $4f^{10} 6s^1 6p^1$, $4f^{10} 5d^1 6s^1$, $4f^9 5d^2 6s^1$, $4f^9 6s^2 6p^1$, $4f^9 5d^1 6s^1 6p^1$, $4f^{10} 6s^1 7s^1$	44669	145025639	19395
Dy II	$\mathbf{4f^{10} 6s^1}$, $\mathbf{4f^{10} 5d^1}$, $4f^9 5d^1 6s^1$, $4f^9 6s^2$, $4f^9 5d^2$, $4f^{10} 6p^1$, $4f^9 6s^1 6p^1$	16034	13700193	2227018
Dy III	$\mathbf{4f^{10}}$, $4f^9 5d^1$, $4f^9 6s^1$, $4f^9 6p^1$	3549	915339	829418
Dy IV	$\mathbf{4f^9}$, $4f^8 5d^1$, $4f^8 6s^1$, $4f^8 6p^1$	5194	1943961	1901856
Dy V	$\mathbf{4f^8 5p^6}$, $\mathbf{4f^9 5p^5}$, $4f^8 5p^5 6s^1$, $4f^8 5p^5 6p^1$, $4f^8 5p^5 5d^1$, $4f^8 5p^5 7s^1$, $4f^8 5p^5 7p^1$, $4f^8 5p^5 6d^1$, $4f^{10} 5p^4$	61924	268129383	80876994
Dy VI	$\mathbf{4f^7 5p^6}$, $\mathbf{4f^8 5p^5}$, $4f^7 5p^5 5d^1$, $4f^7 5p^5 6s^1$, $4f^7 5p^5 6p^1$, $4f^7 5p^5 7s^1$, $4f^7 5p^5 7p^1$, $4f^7 5p^5 6d^1$, $4f^9 5p^4$	71234	360956051	327573289
Dy VII	$\mathbf{4f^7 5p^5}$, $\mathbf{4f^6 5p^6}$, $4f^7 5p^4 5d^1$, $4f^7 5p^4 6p^1$, $4f^7 5p^4 6s^1$, $4f^7 5p^4 7s^1$	94015	566376534	56332605
Dy VIII	$\mathbf{4f^7 5p^4}$, $\mathbf{4f^6 5p^5}$, $4f^7 5p^3 5d^1$, $4f^7 5p^3 6s^1$, $4f^7 5p^3 6p^1$	115103	913738089	913738089
Dy IX	$\mathbf{4f^7 5p^3}$, $\mathbf{4f^6 5p^4}$, $4f^7 5p^2 6s^1$, $4f^7 5p^2 6p^1$, $4f^7 > 5p^2 5d^1$	92861	610943987	61108625
Dy X	$\mathbf{4f^7 5p^2}$, $\mathbf{4f^6 5p^3}$, $4f^7 5p^1 6s^1$, $4f^7 5p^1 6p^1$, $4f^7 5p^1 5d^1$, $4f^7 5p^1 7s^1$, $4f^7 5p^1 7p^1$, $4f^7 5p^1 6d^1$, $4f^8 5p^1$	78312	447640090	44771955
Dy XI	$\mathbf{4f^7 5p^1}$, $\mathbf{4f^6 5p^2}$, $4f^7 6s^1$, $4f^7 6p^1$, $4f^7 5d^1$, $4f^7 7s^1$, $4f^7 7p^1$, $4f^7 6d^1$, $4f^8$	17808	23445375	2345926
Ho I	$\mathbf{4f^{11} 6s^2}$, $4f^{10} 5d^1 6s^2$, $4f^{11} 6s^1 6p^1$, $4f^{10} 6s^2 6p^1$, $4f^{11} 5d^1 6s^1$, $4f^{10} 5d^2 6s^1$, $4f^{10} 5d^1 6s^1 6p^1$, $4f^{11} 6s^1 7s^1$, $4f^{11} 6s^1 7p^1$	23182	41903713	16173
Ho II	$\mathbf{4f^{11} 6s^1}$, $\mathbf{4f^{11} 5d^1}$, $4f^{11} 6p^1$, $4f^{10} 6s^1 6p^1$, $4f^{10} 6s^1 5d^1$, $4f^{10} 5d^1 6p^1$	9640	5254717	510917
Ho III	$\mathbf{4f^{11}}$, $4f^{10} 5d^1$, $4f^{10} 6s^1$, $4f^{10} 6p^1$	1837	259812	239785
Ho IV	$\mathbf{4f^{10}}$, $4f^9 5d^1$, $4f^9 6s^1$, $4f^9 6p^1$	3549	915339	897163
Ho V	$\mathbf{4f^9 5p^6}$, $\mathbf{4f^{10} 5p^5}$, $4f^8 5p^6 6s^1$, $4f^8 5p^6 6p^1$, $4f^8 5p^6 5d^1$, $4f^8 5p^6 7s^1$, $4f^8 5p^6 7p^1$, $4f^8 5p^6 6d^1$, $4f^{11} 5p^4$	11390	9922122	7864433
Ho VI	$\mathbf{4f^8 5p^6}$, $\mathbf{4f^9 5p^5}$, $4f^8 5p^5 6s^1$, $4f^8 5p^5 6p^1$, $4f^8 5p^5 5d^1$, $4f^8 5p^5 7s^1$, $4f^8 5p^5 7p^1$, $4f^8 5p^5 6d^1$, $4f^{10} 5p^4$	61924	268129383	256960118
Ho VII	$\mathbf{4f^7 5p^6}$, $\mathbf{4f^8 5p^5}$, $4f^7 5p^5 6s^1$, $4f^7 5p^5 6p^1$, $4f^7 5p^5 5d^1$, $4f^7 5p^5 7s^1$, $4f^7 5p^5 7p^1$, $4f^7 5p^5 6d^1$, $4f^9 5p^4$	71234	360956050	348425416
Ho VIII	$\mathbf{4f^7 5p^5}$, $\mathbf{4f^6 5p^6}$, $4f^7 5p^4 5d^1$, $4f^7 5p^4 6s^1$, $4f^7 5p^4 6p^1$	84567	481201997	48111620
Ho IX	$\mathbf{4f^7 5p^4}$, $\mathbf{4f^6 5p^5}$, $4f^7 5p^3 5d^1$, $4f^7 5p^3 6s^1$, $4f^7 5p^3 6p^1$	115103	913738088	913738088
Ho X	$\mathbf{4f^7 5p^3}$, $\mathbf{4f^6 5p^4}$, $4f^7 5p^2 5d^1$, $4f^7 5p^2 6s^1$, $4f^7 5p^2 6p^1$, $4f^5 5p^5$	94029	629847851	62984708
Ho XI		78312	447640089	44755094
Er I	$\mathbf{4f^{12} 6s^2}$, $\mathbf{4f^{12} 6s^1 6p^1}$, $\mathbf{4f^{12} 6s^1 7s^1}$, $\mathbf{4f^{12} 6s^1 6d^1}$, $\mathbf{4f^{12} 6s^1 8s^1}$, $4f^{11} 5d^1 6s^2$, $4f^{11} 6s^2 6p^1$, $4f^{12} 5d^1 6s^1$	1303	149737	11731
Er II	$\mathbf{6s^1 4f^{12}}$, $\mathbf{4f^{12} 6p^1}$, $\mathbf{4f^{12} 5d^1}$, $\mathbf{4f^{11} 6s^2}$, $\mathbf{4f^{11} 5d^1 6s^1}$, $\mathbf{4f^{11} 5d^2}$, $\mathbf{4f^{11} 6s^1 6p^1}$, $\mathbf{4f^{11} 5d^1 6p^1}$	5333	2432666	1269676
Er III	$\mathbf{4f^{12}}$, $4f^{11} 5d^1$, $4f^{11} 6s^1$, $4f^{11} 6p^1$	723	42671	40824

Continued on next page

Table D.1 – *Continued from previous page*

Ion	Configurations	$N_{\rm level}$	$N_{\rm line}$	$N^*_{\rm line}$
Er IV	$\mathbf{4f^{11}}$, $4f^{10}6s^1$, $4f^{10}6p^1$, $4f^{10}5d^1$	1837	259812	257750
Er V	$\mathbf{4f^{10}5p^6}$, $\mathbf{4f^{11}5p^5}$, $4f^9 5p^6 5d^1$, $4f^9 5p^6 6s^1$, $4f^9 5p^6 6p^1$, $4f^9 5p^6 7s^1$, $4f^9 5p^6 7p^1$, $4f^9 5p^6 6d^1$, $4f^{12}5p^4$	7404	4126324	3500857
Er VI	$\mathbf{4f^9 5p^6}$, $\mathbf{4f^{10}5p^5}$, $4f^8 5p^6 5d^1$, $4f^8 5p^6 6s^1$, $4f^8 5p^6 6p^1$, $4f^8 5p^6 7s^1$, $4f^8 5p^6 7p^1$, $4f^8 5p^6 6d^1$, $4f^{11}5p^4$	11390	9922122	9829677
Er VII	$\mathbf{4f^8 5p^6}$, $\mathbf{4f^9 5p^5}$, $4f^8 5p^5 5d^1$, $4f^8 5p^5 6s^1$, $4f^8 5p^5 6p^1$, $4f^8 5p^5 7s^1$, $4f^8 5p^5 7p^1$, $4f^8 5p^5 6d^1$, $4f^{10}5p^4$	61924	268129380	264770945
Er VIII	$\mathbf{4f^8 5p^5}$, $\mathbf{4f^7 5p^6}$, $4f^8 5p^4 5d^1$, $4f^8 5p^4 6s^1$, $4f^8 5p^4 6p^1$, $4f^9 5p^4$	77126	419766790	41973419
Er IX	$\mathbf{4f^8 5p^4}$, $\mathbf{4f^7 5p^5}$, $4f^8 5p^3 5d^1$, $4f^8 5p^3 6s^1$, $4f^8 5p^3 6p^1$, $4f^9 5p^3$	106425	793905120	793905120
Er X	$\mathbf{4f^8 5p^3}$, $4f^7 5p^4$, $4f^8 5p^2 5d^1$, $4f^8 5p^2 6s^1$, $4f^8 5p^2 6p^1$, $4f^8 5p^2 7s^1$, $4f^8 5p^2 7p^1$	115282	960990869	96106686
Er XI	$\mathbf{4f^8 5p^2}$, $\mathbf{4f^7 5p^3}$, $4f^8 5p^1 5d^1$, $4f^8 5p^1 6s^1$, $4f^8 5p^1 6p^1$, $4f^8 5p^1 7s^1$, $4f^8 5p^1 7p^1$, $4f^8 5p^1 6d^1$, $4f^9 5p^1$	70629	369445987	36941739
Tm I	$\mathbf{4f^{13}6s^2}$, $\mathbf{4f^{13}6s^1 6p^1}$, $\mathbf{4f^{13}5d^1 6s^1}$, $\mathbf{4f^{13}6s^1 7s^1}$, $\mathbf{4f^{13}6s^1 8s^1}$, $\mathbf{4f^{12}5d^1 6s^2}$, $\mathbf{4f^{12}6s^2 6p^1}$, $\mathbf{4f^{13}6s^1 7p^1}$, $\mathbf{4f^{13}5d^1 6p^1}$, $\mathbf{4f^{13}6s^1 6d^1}$, $4f^{12}5d^1 6s^1 6p^1$, $4f^{13}6p^2$, $4f^{13}6s^1 8p^1$	1716	172582	25853
Tm II	$\mathbf{4f^{13}6s^1}$, $\mathbf{4f^{12}6s^2}$, $\mathbf{4f^{13}5d^1}$, $\mathbf{4f^{13}6p^1}$, $\mathbf{4f^{12}5d^1 6s^1}$, $\mathbf{4f^{12}5d^2}$, $\mathbf{4f^{12}6s^1 6p^1}$, $\mathbf{4f^{12}5d^1 6p^1}$	1484	205258	158892
Tm III	$\mathbf{4f^{13}}$, $4f^{12}5d^1$, $4f^{12}6s^1$, $4f^{12}6p^1$, $4f^{11}5d^1 6s^1$, $4f^{11}5d^1 6p^1$, $4f^{11}6s^1 6p^1$	3666	824686	5582
Tm IV	$\mathbf{4f^{12}}$, $4f^{11}5d^1$, $4f^{11}6s^1$, $4f^{11}6p^1$	723	42671	42671
Tm V	$\mathbf{4f^{11}5p^6}$, $\mathbf{4f^{12}5p^5}$, $4f^{10}5p^6 5d^1$, $4f^{10}5p^6 6s^1$, $4f^{10}5p^6 6p^1$, $4f^{10}5p^6 7s^1$, $4f^{10}5p^6 7p^1$, $4f^{10}5p^6 6d^1$, $4f^{13}5p^4$	3732	1089456	1000581
Tm VI	$\mathbf{4f^{10}5p^6}$, $\mathbf{4f^{11}5p^5}$, $4f^9 5p^6 5d^1$, $4f^9 5p^6 6s^1$, $4f^9 5p^6 6p^1$, $4f^9 5p^6 7s^1$, $4f^9 5p^6 7p^1$, $4f^9 5p^6 6d^1$, $4f^{12}5p^4$	7404	4126324	4106920
Tm VII	$\mathbf{4f^9 5p^6}$, $\mathbf{4f^{10}5p^5}$, $4f^9 5p^5 5d^1$, $4f^9 5p^5 6s^1$, $4f^9 5p^5 6p^1$, $4f^9 5p^5 7s^1$, $4f^9 5p^5 7p^1$, $4f^9 5p^5 6d^1$, $4f^{11}5p^4$	41464	123981375	123401551
Tm VIII	$\mathbf{4f^9 5p^5}$, $\mathbf{4f^8 5p^6}$, $4f^9 5p^4 5d^1$, $4f^9 5p^4 6s^1$, $4f^9 5p^4 6p^1$, $4f^9 5p^4 7s^1$, $4f^9 5p^4 7p^1$, $4f^9 5p^4 6d^1$, $4f^{10}5p^4$	102368	725210231	721396552
Tm IX	$\mathbf{4f^9 5p^4}$, $\mathbf{4f^8 5p^5}$, $4f^9 5p^3 6s^1$, $4f^9 5p^3 6p^1$, $4f^9 5p^3 5d^1$	70095	351045169	35103643
Tm X	$\mathbf{4f^9 5p^3}$, $\mathbf{4f^8 5p^4}$, $4f^9 5p^2 5d^1$, $4f^9 5p^2 6s^1$, $4f^9 5p^2 6p^1$, $4f^9 5p^2 7s^1$, $4f^9 5p^2 7p^1$, $4f^9 5p^2 6d^1$, $4f^{10}5p^2$	108932	853007622	853007622
Tm XI	$\mathbf{4f^9 5p^2}$, $\mathbf{4f^8 5p^3}$, $4f^9 5p^1 5d^1$, $4f^9 5p^1 6s^1$, $4f^9 5p^1 6p^1$, $4f^9 5p^1 7s^1$, $4f^9 5p^1 7p^1$, $4f^9 5p^1 6d^1$, $4f^{10}5p^1$	49074	184983546	184983546
Yb I	$\mathbf{4f^{14}6s^2}$, $\mathbf{4f^{14}6s^1 6p^1}$, $\mathbf{4f^{14}6s^1 5d^1}$, $\mathbf{4f^{14}6s^1 7s^1}$, $\mathbf{4f^{14}6s^1 6d^1}$, $\mathbf{4f^{14}6s^1 7p^1}$, $\mathbf{4f^{14}6s^1 8s^1}$, $\mathbf{4f^{13}6s^2 5d^1}$, $4f^{13}6s^2 6p^1$, $4f^{13}6s^1 5d^2$, $4f^{13}5d^1 6s^1 6p^1$, $4f^{14}6p^2$	446	20948	2821
Yb II	$\mathbf{4f^{14}6s^1}$, $\mathbf{4f^{13}6s^2}$, $\mathbf{4f^{14}5d^1}$, $\mathbf{4f^{14}6p^1}$, $\mathbf{4f^{14}7s^1}$, $4f^{13}5d^1 6s^1$, $4f^{13}5d^2$, $4f^{13}6s^1 6p^1$, $4f^{13}5d^1 6p^1$	265	8109	8024
Yb III	$\mathbf{4f^{14}}$, $4f^{13}5d^1$, $4f^{13}6s^1$, $4f^{13}6p^1$, $4f^{13}7s^1$, $4f^{13}6d^1$, $4f^{12}5d^1 6s^1$, $4f^{12}5d^1 6p^1$, $4f^{12}6s^1 6p^1$	1039	71310	616
Yb IV	$\mathbf{4f^{13}}$, $4f^{12}5d^1$, $4f^{12}6s^1$, $4f^{12}6p^1$	202	3797	3797
Yb V	$\mathbf{4f^{12}5p^6}$, $4f^{13}5p^5$, $4f^{11}5p^6 5d^1$, $4f^{11}5p^6 6s^1$, $4f^{11}5p^6 6p^1$, $4f^{11}5p^6 7s^1$	817	53275	53275
Yb VI	$\mathbf{4f^{11}5p^6}$, $4f^{12}5p^5$, $4f^{10}5p^6 5d^1$, $4f^{10}5p^6 6s^1$, $4f^{10}5p^6 6p^1$, $4f^{10}5p^6 7s^1$	2114	340857	340857

Continued on next page

Table D.1 – *Continued from previous page*

Ion	Configurations	N_{level}	N_{line}	N^*_{line}
Yb VII	$\mathbf{4f^{10}5p^6}$, $4f^{11}5p^5$, $4f^{10}5p^55d^1$, $4f^{10}5p^56s^1$, $4f^{10}5p^56p^1$, $4f^{10}5p^57s^1$	12139	10457118	10455862
Yb VIII	$\mathbf{4f^{10}5p^5}$, $4f^95p^6$, $4f^{10}5p^45d^1$, $4f^{10}5p^46s^1$, $4f^{10}5p^46p^1$, $4f^{10}5p^47s^1$	29622	61593132	61585120
Yb IX	$\mathbf{4f^{10}5p^4}$, $4f^95p^5$, $4f^{10}5p^35d^1$, $4f^{10}5p^36s^1$, $4f^{10}5p^36p^1$, $4f^{10}5p^37s^1$	41167	121033516	121033516
Yb X	$\mathbf{4f^{10}5p^3}$, $4f^95p^4$, $4f^{10}5p^25d^1$, $4f^{10}5p^26s^1$, $4f^{10}5p^26p^1$, $4f^85p^5$	32376	83021204	83021204
Yb XI	$\mathbf{4f^{10}5p^2}$, $4f^95p^3$, $4f^{10}5p^15d^1$, $4f^{10}5p^16s^1$, $4f^{10}5p^16p^1$, $4f^85p^4$	20112	28733284	28733284
Lu I	$\mathbf{5d^16s^2}$, $6s^26p^1$, $5d^16s^16p^1$, $5d^26s^1$, $6s^27s^1$, $6s^26d^1$, $6s^28s^1$, $6s^27p^1$, $6s^16p^2$, $6s^25f^1$, $6s^27d^1$	61	602	391
Lu II	$\mathbf{4f^{14}6s^2}$, $4f^{14}5d^16s^1$, $4f^{14}6s^16p^1$, $4f^{14}5d^2$, $4f^{14}5d^16p^1$, $4f^{14}6s^17s^1$, $4f^{14}6s^16d^1$, $4f^{14}5d^17s^1$, $4f^{14}5d^16d^1$	58	400	335
Lu III	$\mathbf{4f^{14}6s^1}$, $4f^{14}5d^1$, $4f^{14}6p^1$, $4f^{14}7s^1$, $4f^{14}6d^1$, $4f^{13}5d^16s^1$, $4f^{13}5d^16p^1$, $4f^{13}6s^16p^1$	184	2784	1603
Lu IV	$\mathbf{4f^{14}}$, $4f^{13}5d^1$, $4f^{13}6s^1$, $4f^{13}6p^1$, $4f^{13}6d^1$, $4f^{13}7s^1$	61	338	338
Lu V	$\mathbf{4f^{13}5p^6}$, $4f^{14}5p^5$, $4f^{12}5p^65d^1$, $4f^{12}5p^66s^1$, $4f^{12}5p^66p^1$, $4f^{12}5p^67s^1$	228	4611	4611
Lu VI	$\mathbf{4f^{12}5p^6}$, $4f^{13}5p^5$, $4f^{11}5p^65d^1$, $4f^{11}5p^66s^1$, $4f^{11}5p^66p^1$, $4f^{11}5p^67s^1$	817	53275	53275
¿Lu VII	$\mathbf{4f^{11}5p^6}$, $4f^{12}5p^5$, $4f^{11}5p^55d^1$, $4f^{11}5p^56s^1$, $4f^{11}5p^56p^1$, $4f^{11}5p^57s^1$	4688	1700280	1700280
Lu VIII	$\mathbf{4f^{11}5p^5}$, $\mathbf{4f^{10}5p^6}$, $4f^{11}5p^45d^1$, $4f^{11}5p^46s^1$, $4f^{11}5p^46p^1$, $4f^{11}5p^47s^1$	11683	10247264	10247264
Lu IX	$\mathbf{4f^{11}5p^4}$, $\mathbf{4f^{10}5p^5}$, $4f^{11}5p^35d^1$, $4f^{11}5p^36s^1$, $4f^{11}5p^36p^1$, $4f^{11}5p^37s^1$	16109	20510918	20510918
Lu X	$\mathbf{4f^{11}5p^3}$, $4f^{10}5p^4$, $4f^{11}5p^25d^1$, $4f^{11}5p^26s^1$, $4f^{11}5p^26p^1$, $4f^{11}5p^27s^1$	13639	15335633	15335633
Lu XI	$\mathbf{4f^{11}5p^2}$, $4f^{10}5p^3$, $4f^{11}5p^15d^1$, $4f^{11}5p^16s^1$, $4f^{11}5p^16p^1$, $4f^{11}5p^17s^1$	7158	4380853	4380853
Hf I	$\mathbf{5d^26s^2}$, $5d^26s^16p^1$, $5d^36s^1$, $5d^4$, $5d^36p^1$, $5d^26s^17s^1$	313	11138	4146
Hf II	$\mathbf{5d^16s^2}$, $5d^26s^1$, $5d^3$, $5d^16s^16p^1$, $5d^26p^1$, $5d^27s^1$, $5d^16s^17s^1$	129	2418	2418
Hf III	$\mathbf{5d^2}$, $5d^16s^1$, $6s^2$, $5d^16p^1$, $6s^16p^1$, $5d^16d^1$, $5d^17s^1$, $5d^17p^1$	64	594	594
Hf IV	$\mathbf{4f^{14}5d^1}$, $4f^{14}6s^1$, $4f^{14}6p^1$, $4f^{14}6d^1$, $4f^{14}7s^1$, $4f^{14}5f^1$, $4f^{14}7p^1$, $4f^{14}7d^1$	14	35	35
Hf V	$\mathbf{4f^{14}5p^6}$, $4f^{12}5p^66s^2$, $4f^{12}5p^65d^2$, $4f^{12}5p^66p^2$, $4f^{13}5p^66s^1$, $4f^{13}5p^65d^1$, $4f^{13}5p^66p^1$, $4f^{14}5p^56s^1$, $4f^{14}5p^55d^1$, $4f^{14}5p^56p^1$	704	10461	7105
Hf VI	$\mathbf{4f^{13}5p^6}$, $4f^{11}5p^66s^2$, $4f^{11}5p^65d^2$, $4f^{11}5p^66p^2$, $4f^{12}5p^66s^1$, $4f^{12}5p^65d^1$, $4f^{12}5p^66p^1$, $4f^{13}5p^56s^1$, $4f^{13}5p^55d^1$, $4f^{13}5p^56p^1$	2668	240950	174990
Hf VII	$\mathbf{4f^{13}5p^5}$, $4f^{11}5p^56s^2$, $4f^{11}5p^55d^2$, $4f^{11}5p^56p^2$, $4f^{12}5p^56s^1$, $4f^{12}5p^55d^1$, $4f^{12}5p^56p^1$, $4f^{13}5p^46s^1$, $4f^{13}5p^45d^1$, $4f^{13}5p^46p^1$	14972	5370715	3874607

Continued on next page

Table D.1 – *Continued from previous page*

Ion	Configurations	N_{level}	N_{line}	N^*_{line}
Hf VIII	$\mathbf{4f^{13}5p^4}$, $4f^{11}5p^46s^2$, $4f^{11}5p^45d^2$, $4f^{11}5p^46p^2$, $4f^{12}5p^46s^1$, $4f^{12}5p^45d^1$, $4f^{12}5p^46p^1$, $4f^{13}5p^36s^1$, $4f^{13}5p^35d^1$, $4f^{13}5p^36p^1$	35958	26949534	19498022
Hf IX	$\mathbf{4f^{13}5p^3}$, $4f^{11}5p^36s^2$, $4f^{11}5p^35d^2$, $4f^{11}5p^36p^2$, $4f^{12}5p^36s^1$, $4f^{12}5p^35d^1$, $4f^{12}5p^36p^1$, $4f^{13}5p^26s^1$, $4f^{13}5p^25d^1$, $4f^{13}5p^26p^1$	47646	42884855	31062138
Hf X	$\mathbf{4f^{13}5p^2}$, $4f^{12}5p^16s^2$, $4f^{12}5p^15d^2$, $4f^{12}5p^16p^2$, $4f^{12}5p^26s^1$, $4f^{12}5p^25d^1$, $4f^{12}5p^26p^1$, $4f^{13}5p^16s^1$, $4f^{13}5p^15d^1$, $4f^{13}5p^16p^1$	6703	3537394	2893863
Hf XI	$\mathbf{4f^{12}5p^2}$, $4f^{11}5p^16s^2$, $4f^{11}5p^15d^2$, $4f^{11}5p^16p^2$, $4f^{11}5p^26s^1$, $4f^{11}5p^25d^1$, $4f^{11}5p^26p^1$, $4f^{12}5p^16s^1$, $4f^{12}5p^15d^1$, $4f^{12}5p^16p^1$	24773	43159096	34428174
Ta I	$\mathbf{5d^36s^2}$, $\mathbf{5d^5}$, $5d^46s^1$, $5d^36s^16p^1$, $5d^26s^26p^1$, $5d^46p^1$, $5d^36s^17s^1$, $5d^36s^18s^1$	705	58122	25703
Ta II	$\mathbf{5d^36s^1}$, $\mathbf{5d^26s^2}$, $\mathbf{5d^4}$, $5d^36p^1$, $5d^26s^16p^1$, $5d^37s^1$, $5d^36d^1$	487	27199	27162
Ta III	$\mathbf{5d^3}$, $5d^26s^1$, $5d^26p^1$, $5d^16s^2$, $5d^16s^16p^1$, $5d^26d^1$, $5d^27s^1$	188	4452	4452
Ta IV	$\mathbf{5d^2}$, $5d^16s^1$, $5d^16p^1$, $6s^2$, $6s^16p^1$, $5d^16d^1$, $5d^17s^1$	52	336	336
Ta V	$\mathbf{4f^{14}5p^65d^1}$, $4f^{13}5p^66s^2$, $4f^{13}5p^66d^2$, $4f^{13}5p^66p^2$, $4f^{14}5p^56s^2$, $4f^{14}5p^56d^2$, $4f^{14}5p^56p^2$, $4f^{14}5p^66s^1$, $4f^{14}5p^66d^1$, $4f^{14}5p^66p^1$	188	503	8
Ta VI	$\mathbf{4f^{14}}$, $4f^{12}6s^2$, $4f^{12}6d^2$, $4f^{12}6p^2$, $4f^{12}5d^16s^1$, $4f^{12}5d^16d^1$, $4f^{12}5d^16p^1$, $4f^{13}6s^1$, $4f^{13}6d^1$, $4f^{13}6p^1$	2510	446729	2154
Ta VII	$\mathbf{4f^{13}5p^6}$, $4f^{11}5p^66s^2$, $4f^{11}5p^66d^2$, $4f^{11}5p^66p^2$, $4f^{12}5p^56s^2$, $4f^{12}5p^56d^2$, $4f^{12}5p^56p^2$, $4f^{13}5p^56s^1$, $4f^{13}5p^56d^1$, $4f^{13}5p^56p^1$	6119	323087	6071
Ta VIII	$\mathbf{4f^{13}5p^5}$, $4f^{11}5p^56s^2$, $4f^{11}5p^56d^2$, $4f^{11}5p^56p^2$, $4f^{12}5p^46s^2$, $4f^{12}5p^46d^2$, $4f^{12}5p^46p^2$, $4f^{12}5p^56s^1$, $4f^{12}5p^56d^1$, $4f^{12}5p^56p^1$	23497	6130471	140369
Ta IX	$\mathbf{4f^{13}5p^4}$, $4f^{11}5p^46s^2$, $4f^{11}5p^46d^2$, $4f^{11}5p^46p^2$, $4f^{12}5p^36s^2$, $4f^{12}5p^36d^2$, $4f^{12}5p^36p^2$, $4f^{13}5p^36s^1$, $4f^{13}5p^36d^1$, $4f^{13}5p^36p^1$	44996	7220318	72766
Ta X	$\mathbf{4f^{13}5p^3}$, $4f^{11}5p^36s^2$, $4f^{11}5p^35d^2$, $4f^{11}5p^36p^2$, $4f^{12}5p^26s^2$, $4f^{12}5p^25d^2$, $4f^{12}5p^26p^2$, $4f^{13}5p^26s^1$, $4f^{13}5p^25d^1$, $4f^{13}5p^26p^1$	52925	6337511	4493657
Ta XI	$\mathbf{4f^{13}5p^2}$, $4f^{11}5p^26s^2$, $4f^{11}5p^26d^2$, $4f^{11}5p^26p^2$, $4f^{12}5p^16s^2$, $4f^{12}5p^16d^2$, $4f^{12}5p^16p^2$, $4f^{13}5p^16s^1$, $4f^{13}5p^16d^1$, $4f^{13}5p^16p^1$	36330	1813837	24004
W I	$\mathbf{5d^46s^2}$, $5d^56s^1$, $5d^46s^16p^1$, $5d^56p^1$, $5d^46s^17s^1$	808	61598	22278
W II	$\mathbf{5d^46s^1}$, $5d^5$, $5d^36s^2$, $5d^36s^16p^1$, $5d^46p^1$, $5d^47s^1$, $5d^46d^1$	851	84312	80301
W III	$\mathbf{5d^4}$, $5d^36s^1$, $5d^26s^2$, $5d^36p^1$, $5d^26s^16p^1$, $5d^37s^1$, $5d^36d^1$	487	27199	27199
W IV	$\mathbf{5d^3}$, $5d^26s^1$, $5d^26p^1$, $5d^16s^2$, $5d^16s^16p^1$, $5d^27s^1$, $5d^26d^1$	188	4452	4452
W V	$\mathbf{5d^2}$, $5d^16s^1$, $5d^16p^1$, $6s^16p^1$, $5d^15f^1$, $5d^17p^1$, $6s^17p^1$, $6p^17p^1$, $5d^17s^1$, $5d^16d^1$	97	1293	1243
W VI	$\mathbf{4f^{14}5d^1}$, $4f^{14}6s^1$, $4f^{14}6p^1$, $4f^{14}5f^1$, $4f^{14}6d^1$, $4f^{14}7s^1$, $4f^{14}5g^1$, $4f^{14}6g^1$, $4f^{14}7p^1$, $4f^{14}7d^1$	18	41	41
W VII	$\mathbf{4f^{14}}$, $4f^{13}6s^1$, $4f^{13}6p^1$, $4f^{13}5f^1$, $4f^{13}6d^1$, $4f^{13}7s^1$, $4f^{13}5g^1$, $4f^{13}6g^1$, $4f^{13}7p^1$, $4f^{13}7d^1$	155	2292	2292
W VIII	$\mathbf{4f^{13}5p^6}$, $4f^{14}5p^46s^1$, $4f^{14}5p^46p^1$, $4f^{14}5p^45f^1$, $4f^{14}5p^46d^1$, $4f^{14}5p^47s^1$, $4f^{14}5p^45g^1$, $4f^{14}5p^46g^1$, $4f^{14}5p^47p^1$, $4f^{14}5p^47d^1$	206	4994	4994
W IX	$\mathbf{4f^{14}5p^4}$, $4f^{14}5p^36s^1$, $4f^{14}5p^36p^1$, $4f^{14}5p^35f^1$, $4f^{14}5p^36d^1$, $4f^{14}5p^37s^1$, $4f^{14}5p^35g^1$, $4f^{14}5p^36g^1$, $4f^{14}5p^37p^1$, $4f^{14}5p^37d^1$	277	8568	8568

Continued on next page

Table D.1 – *Continued from previous page*

Ion	Configurations	$N_{\rm level}$	$N_{\rm line}$	$N^*_{\rm line}$
W X	$\mathbf{4f^{14}5p^3}$, $4f^{14}5p^26s^1$, $4f^{14}5p^26p^1$, $4f^{14}5p^25d^1$, $4f^{14}5p^16s^2$, $4f^{14}5p^16p^2$, $4f^{14}5p^15d^2$, $4f^{13}5p^26s^2$, $4f^{13}5p^26p^2$, $4f^{13}5p^25d^2$	1726	27111	19039
W XI	$\mathbf{4f^{14}5p^2}$, $4f^{13}5p^26s^1$, $4f^{13}5p^26p^1$, $4f^{13}5p^25f^1$, $4f^{13}5p^26d^1$, $4f^{13}5p^27s^1$, $4f^{13}5p^25g^1$, $4f^{13}5p^26g^1$, $4f^{13}5p^27p^1$, $4f^{13}5p^27d^1$	2183	418768	418768
Re I	$\mathbf{5d^56s^2}$, $\mathbf{5d^66s^1}$, $5d^56s^16p^1$, $5d^46s^26p^1$, $5d^56s^17s^1$, $5d^66p^1$, $5d^56s^16d^1$, $5d^56s^18s^1$, $5d^46s^27s^1$	1875	389214	18721
Re II	$\mathbf{5d^56s^1}$, $\mathbf{5d^46s^2}$, $5d^56p^1$, $5d^6$, $5d^46s^16p^1$, $5d^57s^1$, $5d^56d^1$	1122	138447	102286
Re III	$\mathbf{5d^5}$, $5d^46s^1$, $5d^46p^1$, $5d^36s^16p^1$, $5d^36s^2$, $5d^47s^1$, $5d^46d^1$	851	84312	83853
Re IV	$\mathbf{5d^4}$, $5d^36s^1$, $5d^36p^1$, $5d^26s^2$, $5d^26s^16p^1$, $5d^37s^1$, $5d^36d^1$	487	27199	27199
Re V	$\mathbf{5d^3}$, $5d^26s^1$, $5d^26p^1$, $6s^26p^1$, $5d^25f^1$, $5d^27p^1$, $6s^27p^1$, $6p^27p^1$, $5d^27s^1$, $5d^26d^1$	314	11621	10148
Re VI	$\mathbf{5d^2}$, $5d^16s^1$, $5d^16p^1$, $6s^16p^1$, $5d^15f^1$, $5d^17p^1$, $6s^17p^1$, $6p^17p^1$, $5d^17s^1$, $5d^16d^1$	97	1293	1181
Re VII	$\mathbf{4f^{14}5d^1}$, $4f^{14}6s^1$, $4f^{14}6p^1$, $4f^{14}5f^1$, $4f^{14}6d^1$, $4f^{14}7s^1$, $4f^{14}5g^1$, $4f^{14}6g^1$, $4f^{14}7p^1$, $4f^{14}7d^1$	18	41	41
Re VIII	$\mathbf{4f^{14}5p^6}$, $4f^{14}5p^56s^1$, $4f^{14}5p^56p^1$, $4f^{14}5p^55f^1$, $4f^{14}5p^56d^1$, $4f^{14}5p^57s^1$, $4f^{14}5p^55g^1$, $4f^{14}5p^56g^1$, $4f^{14}5p^57p^1$, $4f^{14}5p^57d^1$	89	896	896
Re IX	$\mathbf{4f^{14}5p^5}$, $4f^{14}5p^46s^1$, $4f^{14}5p^46p^1$, $4f^{14}5p^45f^1$, $4f^{14}5p^46d^1$, $4f^{14}5p^47s^1$, $4f^{14}5p^45g^1$, $4f^{14}5p^46g^1$, $4f^{14}5p^47p^1$, $4f^{14}5p^47d^1$	206	4950	4950
Re X	$\mathbf{4f^{14}5p^4}$, $4f^{14}5p^36s^1$, $4f^{14}5p^36p^1$, $4f^{14}5p^35f^1$, $4f^{14}5p^36d^1$, $4f^{14}5p^37s^1$, $4f^{14}5p^35g^1$, $4f^{14}5p^36g^1$, $4f^{14}5p^37p^1$, $4f^{14}5p^37d^1$	277	8568	8568
Re XI	$\mathbf{4f^{14}5p^3}$, $4f^{14}5p^26s^1$, $4f^{14}5p^26p^1$, $4f^{14}5p^25f^1$, $4f^{14}5p^26d^1$, $4f^{14}5p^27s^1$, $4f^{14}5p^25g^1$, $4f^{14}5p^26g^1$, $4f^{14}5p^27p^1$, $4f^{14}5p^27d^1$	209	5176	5176
Os I	$\mathbf{5d^66s^2}$, $5d^76s^1$, $5d^66s^16p^1$, $5d^66s^17s^1$, $5d^76p^1$, $5d^77s^1$, $5d^77p^1$, $5d^76d^1$	984	107910	27186
Os II	$\mathbf{5d^66s^1}$, $5d^66p^1$, $5d^7$, $5d^66p^1$, $5d^56s^16p^1$, $5d^67s^1$, $5d^66d^1$, $5d^56s^17p^1$	1435	195855	112108
Os III	$\mathbf{5d^6}$, $5d^56s^1$, $5d^56p^1$, $5d^46s^16p^1$, $5d^56d^1$, $5d^57s^1$	1088	130730	117655
Os IV	$\mathbf{5d^5}$, $5d^46s^1$, $5d^46p^1$, $5d^36s^2$, $5d^36s^16p^1$, $5d^47s^1$, $5d^46d^1$	851	84312	84312
Os V	$\mathbf{5d^4}$, $5d^36s^1$, $5d^36p^1$, $5d^16s^26p^1$, $5d^26s^16p^1$, $5d^16s^16p^2$, $5d^35f^1$, $5d^37p^1$, $5d^27p^2$, $5d^16p^27p^1$, $5d^37s^1$, $5d^36d^1$	1131	143017	70770
Os VI	$\mathbf{5d^3}$, $5d^26s^1$, $5d^26p^1$, $5d^16s^16p^1$, $5d^25f^1$, $5d^27p^1$, $5d^17p^2$, $5d^16p^17p^1$, $5d^27s^1$, $5d^26d^1$	405	21187	14055
Os VII	$\mathbf{5d^2}$, $5d^16s^1$, $5d^16p^1$, $6s^16p^1$, $5d^15f^1$, $5d^17p^1$, $6s^17p^1$, $6p^17p^1$, $5d^17s^1$, $5d^16d^1$	97	1293	1243
Os VIII	$\mathbf{4f^{14}5d^1}$, $4f^{14}6s^1$, $4f^{14}6p^1$, $4f^{14}5f^1$, $4f^{14}6d^1$, $4f^{14}7s^1$, $4f^{14}5g^1$, $4f^{14}6g^1$, $4f^{14}7p^1$, $4f^{14}7d^1$	18	41	41
Os IX	$\mathbf{4f^{14}5p^6}$, $4f^{14}5p^56s^1$, $4f^{14}5p^56p^1$, $4f^{14}5p^55f^1$, $4f^{14}5p^56d^1$, $4f^{14}5p^57s^1$, $4f^{14}5p^55g^1$, $4f^{14}5p^56g^1$, $4f^{14}5p^57p^1$, $4f^{14}5p^57d^1$	89	896	896
Os X	$\mathbf{4f^{14}5p^5}$, $4f^{14}5p^46s^1$, $4f^{14}5p^46p^1$, $4f^{14}5p^45f^1$, $4f^{14}5p^46d^1$, $4f^{14}5p^47s^1$, $4f^{14}5p^45g^1$, $4f^{14}5p^46g^1$, $4f^{14}5p^47p^1$, $4f^{14}5p^47d^1$	206	4950	4950

Continued on next page

Table D.1 – *Continued from previous page*

Ion	Configurations	N_{level}	N_{line}	N^*_{line}
Os XI	**$4f^{14}5p^4$**, $4f^{14}5p^3 6s^1$, $4f^{14}5p^3 6p^1$, $4f^{14}5p^3 5f^1$, $4f^{14}5p^3 6d^1$, $4f^{14}5p^3 7s^1$, $4f^{14}5p^3 5g^1$, $4f^{14}5p^3 6g^1$, $4f^{14}5p^3 7p^1$, $4f^{14}5p^3 7d^1$	277	8568	8568
Ir I	**$5d^7 6s^2$**, **$5d^9$**, $5d^8 6s^1$, $5d^7 6s^1 6p^1$, $5d^7 6s^1 7s^1$, $5d^8 6p^1$, $5d^8 7s^1$	385	16855	9449
Ir II	**$5d^7 6s^1$**, $5d^8$, $5d^6 6s^2$, $5d^7 6p^1$, $5d^6 6s^1 6p^1$, $5d^7 7s^1$, $5d^7 7p^1$	699	32647	29639
Ir III	**$5d^7$**, $5d^6 6s^1$, $5d^6 6p^1$, $5d^5 6s^2$, $5d^6 6d^1$, $5d^6 7s^1$, $5d^6 7p^1$	818	76592	73814
Ir IV	**$5d^6$**, $5d^5 6s^1$, $5d^5 6p^1$, $5d^4 6s^2$, $5d^5 6d^1$, $5d^5 7s^1$, $5d^5 7p^1$	976	104622	104622
Ir V	**$5d^5$**, $5d^3 6s^2$, $5d^4 6s^1$, $5d^3 6s^1 6p^1$, $5d^2 6s^2 6p^1$, $5d^4 6p^1$, $5d^3 6s^1 7s^1$, $5d^3 6s^1 8s^1$	705	58122	43221
Ir VI	**$5d^4$**, $5d^2 6s^2$, $5d^2 6s^1 6p^1$, $5d^3 6s^1$	171	3606	3606
Ir VII	**$5d^3$**, $5d^1 6s^2$, $6s^2 6p^1$, $5d^1 6s^1 6p^1$, $5d^2 6s^1$, $6s^2 7s^1$, $6s^2 7p^1$, $6s^2 6d^1$, $6s^1 6p^2$, $6s^2 8s^1$, $6s^2 5f^1$, $6s^2 7d^1$, $6s^2 8p^1$, $5d^1 6s^1 7s^1$	90	1156	896
Ir VIII	**$5d^2$**, $5d^1 6s^1$, $5d^1 6p^1$, $6s^1 6p^1$, $5d^1 5f^1$, $5d^1 7p^1$, $6s^1 7p^1$, $6p^1 7p^1$, $5d^1 7s^1$, $5d^1 6d^1$	97	1293	1280
Ir IX	**$4f^{14}5d^1$**, $4f^{14}6s^1$, $4f^{14}6p^1$, $4f^{14}5f^1$, $4f^{14}6d^1$, $4f^{14}7s^1$, $4f^{14}5g^1$, $4f^{14}6g^1$, $4f^{14}7p^1$, $4f^{14}7d^1$	18	41	41
Ir X	**$4f^{14}5p^6$**, $4f^{14}5p^5 6s^1$, $4f^{14}5p^5 6p^1$, $4f^{14}5p^5 5f^1$, $4f^{14}5p^5 6d^1$, $4f^{14}5p^5 7s^1$, $4f^{14}5p^5 5g^1$, $4f^{14}5p^5 6g^1$, $4f^{14}5p^5 7p^1$, $4f^{14}5p^5 7d^1$	89	896	896
Ir XI	**$4f^{14}5p^5$**, $4f^{14}5p^4 6s^1$, $4f^{14}5p^4 6p^1$, $4f^{14}5p^4 5f^1$, $4f^{14}5p^4 6d^1$, $4f^{14}5p^4 7s^1$, $4f^{14}5p^4 5g^1$, $4f^{14}5p^4 6g^1$, $4f^{14}5p^4 7p^1$, $4f^{14}5p^4 7d^1$	206	4950	4950
Pt I	**$5d^9 6s^1$**, **$5d^{10}$**, **$5d^9 6p^1$**, **$5d^9 7s^1$**, $5d^8 6s^2$, $5d^8 6s^1 6p^1$, $5d^8 6s^1 7s^1$	152	2729	1637
Pt II	**$5d^9$**, $5d^8 6s^1$, $5d^7 6s^2$, $5d^8 6p^1$, $5d^8 7s^1$, $5d^8 6d^1$, $5d^8 8s^1$, $5d^8 7d^1$	248	4837	4759
Pt III	**$5d^8$**, $5d^7 6s^1$, $5d^7 6p^1$, $5d^7 7s^1$, $5d^6 6s^1 6p^1$	555	19157	18477
Pt IV	**$5d^7$**, $5d^6 6s^1$, $5d^6 6p^1$, $5d^6 6d^1$, $5d^6 7s^1$, $5d^6 7p^1$	781	70102	70102
Pt V	**$5d^6$**, $5d^5 6s^1$, $5d^5 6p^1$, $5d^4 6s^2$, $5d^4 6s^1 6p^1$, $5d^4 6s^1 7s^1$	842	70268	65327
Pt VI	**$5d^5$**, $5d^4 6s^1$, $5d^4 6p^1$, $5d^3 6s^2$, $5d^3 6s^1 6p^1$, $5d^2 6s^2 6p^1$, $5d^3 6s^1 7s^1$, $5d^3 6s^1 8s^1$	705	58122	42946
Pt VII	**$5d^4$**, $5d^3 6s^1$, $5d^3 6p^1$, $5d^2 6s^2$, $5d^2 6s^1 6p^1$	281	7872	7872
Pt VIII	**$5d^3$**, $5d^2 6s^1$, $5d^2 6p^1$, $5d^1 6s^2$, $6s^2 6p^1$, $5d^1 6s^1 6p^1$, $6s^2 7s^1$, $6s^2 7p^1$, $6s^2 6d^1$, $6s^1 6p^2$, $6s^2 8s^1$, $6s^2 5f^1$, $6s^2 7d^1$, $6s^2 8p^1$, $5d^1 6s^1 7s^1$	135	2666	2250
Pt IX	**$5d^2$**, $6s^2$, $6s^1 6p^1$, $5d^1 6s^1$, $6s^1 7s^1$, $6s^1 7p^1$, $6s^1 6d^1$, $6s^1 8s^1$, $6p^2$, $6s^1 5f^1$, $6s^1 8p^1$, $6s^1 7d^1$, $6s^1 9s^1$, $6s^1 6f^1$, $6s^1 9p^1$, $6s^1 8d^1$	61	520	404
Pt X	**$4f^{14}5d^1$**, $4f^{13}6s^2$, $4f^{12}5d^1 6s^2$, $4f^{13}6s^1 6p^1$, $4f^{13}5d^1 6s^1$, $4f^{12}6s^2 6p^1$, $4f^{13}6s^1 7s^1$, $4f^{13}6s^1 7p^1$, $4f^{13}5d^1 6p^1$, $4f^{13}6s^1 6d^1$, $4f^{13}6s^1 8s^1$, $4f^{13}6p^2$, $4f^{13}6s^1 8p^1$	489	26962	2113

Continued on next page

Table D.1 – *Continued from previous page*

Ion	Configurations	N_{level}	N_{line}	N^*_{line}
Pt XI	$\mathbf{4f^{14}5p^6}$, $4f^{12}5p^66s^2$, $4f^{13}5p^65d^1$, $4f^{13}5p^66p^1$, $4f^{13}5p^66s^1$, $4f^{12}5p^65d^16s^1$, $4f^{11}5p^65d^26s^1$, $4f^{12}5p^65d^16p^1$, $4f^{12}5p^66s^17s^1$, $4f^{12}5p^66s^16d^1$, $4f^{12}5p^66s^18s^1$, $4f^{11}5p^65d^16s^17s^1$	5974	1055973	169
Au I	$\mathbf{5d^{10}6s^1}$, $5d^96s^2$, $5d^{10}6p^1$, $5d^96s^16p^1$, $5d^{10}7s^1$, $5d^{10}7p^1$, $5d^{10}6d^1$, $5d^{10}8s^1$, $5d^{10}8p^1$	36	141	101
Au II	$\mathbf{5d^{10}}$, $5d^96s^1$, $5d^86s^2$, $5d^96p^1$, $5d^97s^1$, $5d^96d^1$, $5d^97p^1$	60	516	516
Au III	$\mathbf{5d^9}$, $5d^86s^1$, $5d^86p^1$, $5d^76s^2$, $5d^87s^1$, $5d^86d^1$, $5d^87p^1$	210	5764	5690
Au IV	$\mathbf{5d^8}$, $5d^76s^1$, $5d^76p^1$, $5d^66s^2$, $5d^77s^1$, $5d^76d^1$, $5d^77p^1$	507	29606	29606
Au V	$\mathbf{5d^7}$, $5d^56s^2$, $5d^66s^1$, $5d^56s^16p^1$, $5d^46s^26p^1$, $5d^56s^17s^1$, $5d^66p^1$, $5d^56s^16d^1$, $5d^56s^18s^1$, $5d^46s^27s^1$	1894	396564	266496
Au VI	$\mathbf{5d^6}$, $5d^46s^2$, $5d^56s^1$, $5d^46s^16p^1$, $5d^56p^1$, $5d^46s^17s^1$	842	70268	68707
Au VII	$\mathbf{5d^5}$, $5d^36s^2$, $5d^46s^1$, $5d^36s^16p^1$, $5d^26s^26p^1$, $5d^46p^1$, $5d^36s^17s^1$, $5d^36s^18s^1$	705	58122	43338
Au VIII	$\mathbf{5d^4}$, $5d^26s^2$, $5d^26s^16p^1$, $5d^36s^1$	171	3606	3606
Au IX	$\mathbf{5d^3}$, $5d^16s^2$, $6s^26p^1$, $5d^16s^16p^1$, $5d^26s^1$, $6s^27s^1$, $6s^27p^1$, $6s^26d^1$, $6s^16p^2$, $6s^28s^1$, $6s^25f^1$, $6s^27d^1$, $6s^28p^1$, $5d^16s^17s^1$	90	1156	896
Au X	$\mathbf{5d^2}$, $6s^2$, $6s^16p^1$, $5d^16s^1$, $6s^17s^1$, $6s^17p^1$, $6s^16d^1$, $6s^18s^1$, $6p^2$, $6s^15f^1$, $6s^18p^1$, $6s^17d^1$, $6s^19s^1$, $6s^16f^1$, $6s^19p^1$, $6s^18d^1$	61	520	378
Au XI	$\mathbf{4f^{14}5d^1}$, $4f^{13}6s^2$, $4f^{12}5d^16s^2$, $4f^{13}6s^16p^1$, $4f^{13}5d^16s^1$, $4f^{12}6s^26p^1$, $4f^{12}5d^16s^16p^1$, $4f^{13}6s^17s^1$, $4f^{13}6s^17p^1$, $4f^{13}5d^16p^1$, $4f^{13}6s^16d^1$, $4f^{13}6s^18s^1$, $4f^{13}6p^2$, $4f^{13}6s^18p^1$, $4f^{13}6s^117p^1$, $4f^{13}6s^118p^1$, $4f^{13}6s^119p^1$, $4f^{13}6s^120p^1$, $4f^{13}6s^130p^1$, $4f^{13}6s^131p^1$	1862	266914	2048
Hg I	$\mathbf{5d^{10}6s^2}$, $5d^{10}6s^16p^1$, $5d^{10}6s^17s^1$, $5d^96s^26p^1$, $5d^{10}6s^17p^1$, $5d^{10}6s^16d^1$, $5d^{10}6s^18s^1$, $5d^{10}6s^18p^1$, $5d^{10}6s^17d^1$, $5d^{10}6s^15f^1$	41	229	177
Hg II	$\mathbf{5d^{10}6s^1}$, $5d^96s^2$, $5d^{10}6p^1$, $5d^96s^16p^1$, $5d^{10}7s^1$, $5d^{10}6d^1$, $5d^{10}7p^1$, $5d^{10}8s^1$, $5d^{10}5f^1$, $5d^{10}7d^1$	38	180	180
Hg III	$\mathbf{5d^{10}}$, $5d^96s^1$, $5d^86s^2$, $5d^96p^1$, $5d^86s^16p^1$, $5d^97s^1$, $5d^96d^1$	138	1948	1948
Hg IV	$\mathbf{5d^9}$, $5d^86s^1$, $5d^86p^1$, $5d^76s^2$, $5d^86d^1$, $5d^87s^1$	165	2882	2882
Hg V	$\mathbf{5d^8}$, $5d^66s^2$, $5d^76s^1$, $5d^66s^16p^1$, $5d^66s^17s^1$	567	34122	30074
Hg VI	$\mathbf{5d^7}$, $5d^56s^2$, $5d^66s^1$, $5d^56s^16p^1$, $5d^46s^26p^1$, $5d^56s^17s^1$, $5d^66p^1$, $5d^56s^16d^1$, $5d^56s^18s^1$, $5d^46s^27s^1$	1894	396564	291191
Hg VII	$\mathbf{5d^6}$, $5d^46s^2$, $5d^56s^1$, $5d^46s^16p^1$, $5d^56p^1$, $5d^46s^17s^1$	842	70268	69613
Hg VIII	$\mathbf{5d^5}$, $5d^36s^2$, $5d^46s^1$, $5d^36s^16p^1$, $5d^26s^26p^1$, $5d^46p^1$, $5d^36s^17s^1$, $5d^36s^18s^1$	705	58122	43338
Hg IX	$\mathbf{5d^4}$, $5d^26s^2$, $5d^26s^16p^1$, $5d^36s^1$	171	3606	3606
Hg X	$\mathbf{5d^3}$, $5d^16s^2$, $6s^26p^1$, $5d^16s^16p^1$, $5d^26s^1$, $6s^27s^1$, $6s^27p^1$, $6s^26d^1$, $6s^16p^2$, $6s^28s^1$, $6s^25f^1$, $6s^27d^1$, $6s^28p^1$, $5d^16s^17s^1$	90	1156	917

Continued on next page

Table D.1 – *Continued from previous page*

Ion	Configurations	N_{level}	N_{line}	N^*_{line}
Hg XI	**$4f^{14}5d^2$**, $4f^{14}6s^2$, $4f^{14}6s^16p^1$, $4f^{14}5d^16s^2$, $4f^{14}5d^16s^1$, $4f^{13}6s^26p^1$, $4f^{14}6s^17s^1$, $4f^{13}5d^26s^1$, $4f^{14}6s^17p^1$, $4f^{14}6s^16d^1$	222	2531	1237
Tl I	**$6s^26p^1$**, **$6s^27s^1$**, **$6s^27p^1$**, $6s^26d^1$, $6s^28s^1$, $6s^28p^1$, $6s^27d^1$	12	30	30
Tl II	**$5d^{10}6s^2$**, $5d^{10}6s^16p^1$, $5d^{10}6s^17s^1$, $5d^96s^26p^1$, $5d^{10}6s^16d^1$, $5d^{10}6p^2$, $5d^{10}6s^17p^1$, $5d^{10}6s^18s^1$, $5d^{10}6s^15f^1$, $5d^{10}6s^17d^1$, $5d^{10}6s^18p^1$	46	312	312
Tl III	**$5d^{10}6s^1$**, $5d^{10}6p^1$, $5d^96s^2$, $5d^96s^16p^1$, $5d^{10}7s^1$, $5d^{10}6d^1$, $5d^{10}7p^1$, $5d^{10}5f^1$, $5d^{10}8s^1$, $5d^{10}7d^1$, $5d^{10}8p^1$	40	195	195
Tl IV	**$5d^{10}$**, $5d^96s^1$, $5d^96p^1$, $5d^96d^1$, $5d^97s^1$, $5d^98s^1$	43	234	234
Tl V	**$5d^9$**, $5d^76s^2$, $5d^86s^1$, $5d^76s^16p^1$, $5d^76s^17s^1$	324	12007	12007
Tl VI	**$5d^8$**, $5d^66s^2$, $5d^76s^1$, $5d^66s^16p^1$, $5d^66s^17s^1$	567	34122	32137
Tl VII	**$5d^7$**, $5d^56s^2$, $5d^66s^1$, $5d^56s^16p^1$, $5d^46s^26p^1$, $5d^56s^17s^1$, $5d^66p^1$, $5d^56s^16d^1$, $5d^56s^18s^1$, $5d^46s^27s^1$	1894	396564	307512
Tl VIII	**$5d^6$**, $5d^46s^2$, $5d^56s^1$, $5d^46s^16p^1$, $5d^56p^1$, $5d^46s^17s^1$	842	70268	70268
Tl IX	**$5d^5$**, $5d^36s^2$, $5d^46s^1$, $5d^36s^16p^1$, $5d^26s^26p^1$, $5d^46p^1$, $5d^36s^17s^1$, $5d^36s^18s^1$	705	58122	44037
Tl X	**$5d^4$**, $5d^26s^2$, $5d^26s^16p^1$, $5d^36s^1$	171	3606	3606
Tl XI	**$5d^3$**, $5d^16s^2$, $6s^26p^1$, $5d^16s^16p^1$, $5d^26s^1$, $6s^27s^1$, $6s^27p^1$, $6s^26d^1$, $6s^16p^2$, $6s^28s^1$, $6s^25f^1$, $6s^27d^1$, $6s^28p^1$, $5d^16s^17s^1$	90	1156	951
Pb I	**$6s^26p^2$**, **$6s^26p^17s^1$**, **$6s^26p^17p^1$**, **$6s^26p^16d^1$**, **$6s^26p^18s^1$**, **$6s^26p^18p^1$**, $6s^26p^17d^1$, $6s^26p^15f^1$, $6s^26p^19s^1$, $6s^26p^19p^1$, $6s^26p^18d^1$	95	1398	1182
Pb II	**$6s^26p^1$**, $6s^16p^2$, $6s^27s^1$, $6s^26d^1$, $6s^27p^1$, $6s^28s^1$, $6s^25f^1$, $6s^27d^1$, $6s^28p^1$, $6s^29s^1$, $6s^26f^1$, $6s^28d^1$	27	119	119
Pb III	**$5d^{10}6s^2$**, $5d^{10}6s^16p^1$, $5d^{10}6p^2$, $5d^{10}6s^17s^1$, $5d^{10}6s^16d^1$, $5d^96s^26p^1$, $5d^{10}6s^17p^1$, $5d^{10}6s^15f^1$, $5d^{10}6s^18s^1$, $5d^{10}6s^17d^1$, $5d^{10}6s^18p^1$, $5d^{10}6s^16f^1$	50	343	343
Pb IV	**$5d^{10}6s^1$**, $5d^{10}6p^1$, $5d^96s^2$, $5d^96s^16p^1$, $5d^{10}6d^1$, $5d^{10}7s^1$, $5d^{10}7p^1$, $5d^{10}5f^1$, $5d^{10}8s^1$, $5d^{10}7d^1$, $5d^96p^2$, $5d^{10}8p^1$	68	746	721
Pb V	**$5d^{10}$**, $5d^96s^1$, $5d^96p^1$, $5d^96d^1$, $5d^97s^1$, $5d^97p^1$, $5d^86s^2$, $5d^86s^16p^1$, $5d^86s^17s^1$	182	4167	4000
Pb VI	**$5d^9$**, $5d^76s^2$, $5d^86s^1$, $5d^76s^16p^1$, $5d^76s^17s^1$	324	12007	11055
Pb VII	**$5d^8$**, $5d^66s^2$, $5d^76s^1$, $5d^66s^16p^1$, $5d^66s^17s^1$	567	34122	33915
Pb VIII	**$5d^7$**, $5d^56s^2$, $5d^66s^1$, $5d^56s^16p^1$, $5d^46s^26p^1$, $5d^56s^17s^1$, $5d^66p^1$, $5d^56s^16d^1$, $5d^56s^18s^1$, $5d^46s^27s^1$	1894	396564	325532
Pb IX	**$5d^6$**, $5d^46s^2$, $5d^56s^1$, $5d^46s^16p^1$, $5d^56p^1$, $5d^46s^17s^1$	842	70268	70268
Pb X	**$5d^5$**, $5d^36s^2$, $5d^46s^1$, $5d^36s^16p^1$, $5d^26s^26p^1$, $5d^46p^1$, $5d^36s^17s^1$, $5d^36s^18s^1$	705	58122	46809
Pb XI	**$5d^4$**, $5d^26s^2$, $5d^26s^16p^1$, $5d^36s^1$	171	3606	3606

Continued on next page

Table D.1 – *Continued from previous page*

Ion	Configurations	$N_{\rm level}$	$N_{\rm line}$	$N^*_{\rm line}$
Bi I	$\mathbf{6p^27s^1}$, $\mathbf{6p^3}$, $6p^27p^1$, $6p^26d^1$, $6p^28s^1$, $6p^28p^1$, $6p^27d^1$, $6p^29s^1$, $6p^29p^1$, $6p^28d^1$	176	4986	270
Bi II	$\mathbf{6s^26p^2}$, $\mathbf{6s^26p^17s^1}$, $6s^16p^3$, $6s^26p^16d^1$, $6s^26p^17p^1$, $6s^26p^18s^1$, $6s^26p^15f^1$, $6s^26p^17d^1$, $6s^26p^18p^1$, $6s^26p^19s^1$, $6s^26p^16f^1$, $6s^26p^18d^1$	107	1685	744
Bi III	$\mathbf{6s^26p^1}$, $6s^16p^2$, $6s^27s^1$, $6s^26d^1$, $6s^27p^1$, $6s^25f^1$, $6s^28s^1$, $6s^27d^1$, $6s^28p^1$, $6s^26f^1$	24	98	98
Bi IV	$\mathbf{5d^{10}6s^2}$, $5d^{10}6s^16p^1$, $5d^{10}6p^2$, $5d^{10}6s^16d^1$, $5d^{10}6s^17s^1$, $5d^96s^26p^1$, $5d^{10}6s^17p^1$, $5d^{10}6s^15f^1$, $5d^{10}6s^18s^1$, $5d^{10}6s^17d^1$	42	262	262
Bi V	$\mathbf{5d^{10}6s^1}$, $5d^{10}6p^1$, $5d^96s^2$, $5d^{10}6d^1$, $5d^{10}7s^1$, $5d^{10}7p^1$, $5d^{10}7d^1$, $5d^{10}8s^1$, $5d^96s^16p^1$, $5d^{10}8p^1$	38	186	186
Bi VI	$\mathbf{5d^{10}}$, $5d^96s^1$, $5d^96p^1$, $5d^96d^1$, $5d^95f^1$, $5d^86s^16p^1$, $5d^97s^1$, $5d^97p^1$, $5d^96f^1$, $5d^86s^2$, $5d^86s^17s^1$	222	5461	5461
Bi VII	$\mathbf{5d^9}$, $5d^76s^2$, $5d^86s^1$, $5d^76s^16p^1$, $5d^76s^17s^1$	324	12007	12007
Bi VIII	$\mathbf{5d^8}$, $5d^66s^2$, $5d^76s^1$, $5d^66s^16p^1$, $5d^66s^17s^1$	567	34122	34122
Bi IX	$\mathbf{5d^7}$, $5d^56s^2$, $5d^66s^1$, $5d^56s^16p^1$, $5d^46s^26p^1$, $5d^56s^17s^1$, $5d^66p^1$, $5d^56s^16d^1$, $5d^56s^18s^1$, $5d^46s^27s^1$	1894	396564	343315
Bi X	$\mathbf{5d^6}$, $5d^46s^2$, $5d^56s^1$, $5d^46s^16p^1$, $5d^56p^1$, $5d^46s^17s^1$	842	70268	70268
Bi XI	$\mathbf{5d^5}$, $5d^36s^2$, $5d^46s^1$, $5d^36s^16p^1$, $5d^26s^26p^1$, $5d^46p^1$, $5d^36s^17s^1$, $5d^36s^18s^1$	705	58122	47199
Po I	$\mathbf{6p^4}$, $\mathbf{6p^37s^1}$, $\mathbf{6p^37p^1}$, $\mathbf{6p^36d^1}$, $\mathbf{6p^38s^1}$, $6p^38p^1$, $6p^37d^1$, $6p^39p^1$, $6p^38d^1$, $6p^310p^1$	251	9553	135
Po II	$\mathbf{6s^26p^3}$, $6s^16p^4$, $6s^26p^27s^1$, $6s^26p^26d^1$, $6s^26p^27p^1$, $6s^26p^28s^1$, $6s^26p^27d^1$, $6s^26p^25f^1$, $6s^26p^28p^1$, $6s^26p^29s^1$	165	4238	873
Po III	$\mathbf{6s^26p^2}$, $6s^16p^3$, $6s^26p^16d^1$, $6s^26p^17s^1$, $6s^26p^17p^1$, $6s^26p^17d^1$, $6s^26p^18s^1$	57	419	369
Po IV	$\mathbf{6s^26p^1}$, $6s^16p^2$, $6s^26d^1$, $6s^27s^1$, $6s^27p^1$, $6s^27d^1$, $6s^28s^1$	18	48	48
Po V	$\mathbf{6s^2}$, $6s^16p^1$, $6s^17s^1$, $6s^17p^1$, $6s^16d^1$, $6s^18s^1$, $6s^18p^1$, $6s^17d^1$, $6s^15f^1$	29	130	130
Po VI	$\mathbf{5d^{10}6s^1}$, $5d^96s^2$, $5d^{10}6p^1$, $5d^96s^16p^1$, $5d^{10}7s^1$, $5d^{10}7p^1$, $5d^{10}6d^1$, $5d^{10}8s^1$, $5d^{10}8p^1$, $5d^{10}6s^1$	36	141	141
Po VII	$\mathbf{5d^{10}}$, $5d^96s^1$, $5d^86s^2$, $5d^86s^16p^1$, $5d^96p^1$, $5d^97s^1$, $5d^86s^17s^1$	152	2729	2729
Po VIII	$\mathbf{5d^9}$, $5d^76s^2$, $5d^86s^1$, $5d^76s^16p^1$, $5d^76s^17s^1$	324	12007	12007
Po IX	$\mathbf{5d^8}$, $5d^66s^2$, $5d^76s^1$, $5d^66s^16p^1$, $5d^66s^17s^1$	567	34122	34122
Po X	$\mathbf{5d^7}$, $5d^56s^2$, $5d^66s^1$, $5d^56s^16p^1$, $5d^46s^26p^1$, $5d^56s^17s^1$, $5d^66p^1$, $5d^56s^16d^1$, $5d^56s^18s^1$, $5d^46s^27s^1$	1894	396564	332014
Po XI	$\mathbf{5d^6}$, $5d^46s^2$, $5d^56s^1$, $5d^46s^16p^1$, $5d^56p^1$, $5d^46s^17s^1$	842	70268	70268
At I	$\mathbf{6p^5}$, $6p^47s^1$, $6p^47p^1$, $6p^46d^1$, $6p^48s^1$, $6p^48p^1$, $6p^47d^1$	116	2136	3
At II	$\mathbf{6s^26p^4}$, $6s^26p^37s^1$, $6s^16p^5$, $6s^26p^36d^1$, $6s^26p^37p^1$, $6s^26p^38s^1$, $6s^26p^37d^1$, $6s^26p^35f^1$, $6s^26p^38p^1$, $6s^26p^39s^1$, $6s^26p^38d^1$, $6s^26p^36f^1$	289	11510	881

Continued on next page

Table D.1 – *Continued from previous page*

Ion	Configurations	N_{level}	N_{line}	N^*_{line}
At III	$\mathbf{6s^2 6p^3}$, $6s^1 6p^4$, $6s^2 6p^2 6d^1$, $6s^2 6p^2 7s^1$, $6s^2 6p^2 8s^1$, $6s^2 6p^2 7d^1$, $6s^2 6p^2 9s^1$, $6s^2 6p^2 8d^1$	121	431	317
At IV	$\mathbf{6s^2 6p^2}$, $6s^1 6p^3$, $6s^2 6p^1 6d^1$, $6s^2 6p^1 7s^1$, $6s^2 6p^1 7d^1$, $6s^2 6p^1 8s^1$, $6s^2 6p^1 8d^1$, $6s^2 6p^1 9s^1$	63	179	179
At V	$\mathbf{6s^2 6p^1}$, $6s^2 7s^1$, $6s^2 7p^1$, $6s^2 6d^1$, $6s^2 8s^1$, $6s^2 8p^1$, $6s^2 7d^1$, $6s^2 5f^1$, $6s^1 6p^2$	22	85	85
At VI	$\mathbf{6s^2}$, $6s^1 6p^1$, $6s^1 6d^1$, $6s^1 7p^1$	13	26	26
At VII	$\mathbf{5d^{10} 6s^1}$, $5d^9 6s^2$, $5d^{10} 6p^1$, $5d^{10} 7s^1$, $5d^{10} 7p^1$, $5d^{10} 6d^1$, $5d^{10} 8s^1$, $5d^{10} 8p^1$, $5d^{10} 6s^1$	13	36	36
At VIII	$\mathbf{5d^{10}}$, $5d^9 6s^1$, $5d^8 6s^2$, $5d^8 6s^1 6p^1$, $5d^9 6p^1$, $5d^9 7s^1$, $5d^8 6s^1 7s^1$	152	2729	2729
At IX	$\mathbf{5d^9}$, $5d^7 6s^2$, $5d^8 6s^1$, $5d^7 6s^1 6p^1$, $5d^7 6s^1 7s^1$	324	12007	12007
At X	$\mathbf{5d^8}$, $5d^6 6s^2$, $5d^7 6s^1$, $5d^6 6s^1 6p^1$, $5d^6 6s^1 7s^1$	567	34122	34122
At XI	$\mathbf{5d^7}$, $5d^5 6s^2$, $5d^6 6s^1$, $5d^5 6s^1 6p^1$, $5d^4 6s^2 6p^1$, $5d^5 6s^1 7s^1$, $5d^6 6p^1$, $5d^5 6s^1 6d^1$, $5d^5 6s^1 8s^1$, $5d^4 6s^2 7s^1$	1894	396564	337686
Rn I	$\mathbf{6p^6}$, $6p^5 7s^1$, $6p^5 7p^1$, $6p^5 6d^1$, $6p^5 8p^1$, $6p^5 7d^1$, $6p^5 9s^1$, $6p^5 5f^1$	65	634	0
Rn II	$\mathbf{6s^2 6p^5}$, $6s^1 6p^6$, $6s^2 6p^4 7s^1$, $6s^2 6p^4 6d^1$, $6s^2 6p^4 7p^1$, $6s^2 6p^4 8s^1$, $6s^2 6p^4 7d^1$, $6s^2 6p^4 5f^1$, $6s^2 6p^4 8p^1$, $6s^2 6p^4 9s^1$	155	3685	477
Rn III	$\mathbf{6s^2 6p^4}$, $6s^1 6p^5$, $6s^2 6p^3 6d^1$, $6s^2 6p^3 7s^1$, $6s^2 6p^3 7p^1$, $6s^2 6p^3 5f^1$, $6s^2 6p^3 7d^1$, $6s^2 6p^3 8s^1$, $6s^2 6p^3 6f^1$, $6p^6$	214	6052	1336
Rn IV	$\mathbf{6s^2 6p^3}$, $6s^1 6p^4$, $6s^2 6p^2 6d^1$, $6s^2 6p^2 7s^1$, $6s^2 6p^2 5f^1$, $6s^2 6p^2 7p^1$	100	1480	1368
Rn V	$\mathbf{6p^2}$, $6p^1 7s^1$, $6p^1 7p^1$, $6p^1 6d^1$, $6p^1 8s^1$, $6p^1 8p^1$, $6p^1 7d^1$, $6p^1 5f^1$, $6p^1 9s^1$, $6p^1 9p^1$, $6p^1 8d^1$	95	1398	43
Rn VI	$\mathbf{6s^2 6p^1}$, $6s^2 7s^1$, $6s^2 7p^1$, $6s^2 6d^1$, $6s^2 8s^1$, $6s^2 8p^1$, $6s^2 7d^1$, $6s^2 5f^1$, $6s^1 6p^2$	22	85	85
Rn VII	$\mathbf{6s^2}$, $\mathbf{6s^1 6p^1}$, $\mathbf{6s^1 7s^1}$, $6s^1 7p^1$, $6s^1 6d^1$, $6s^1 8s^1$, $6s^1 8p^1$, $6s^1 7d^1$, $6s^1 5f^1$, $6s^1 6f^1$	33	152	152
Rn VIII	$\mathbf{5d^{10} 6s^1}$, $5d^9 6s^2$, $5d^{10} 6p^1$, $5d^9 6s^1 6p^1$, $5d^{10} 7s^1$, $5d^{10} 7p^1$, $5d^{10} 6d^1$, $5d^{10} 8s^1$, $5d^{10} 8p^1$	36	141	141
Rn IX	$\mathbf{5d^{10}}$, $5d^9 6s^1$, $5d^8 6s^2$, $5d^8 6s^1 6p^1$, $5d^9 6p^1$, $5d^9 7s^1$, $5d^8 6s^1 7s^1$	152	2729	2729
Rn X	$\mathbf{5d^9}$, $5d^7 6s^2$, $5d^8 6s^1$, $5d^7 6s^1 6p^1$, $5d^7 6s^1 7s^1$	324	12007	12007
Rn XI	$\mathbf{5d^8}$, $5d^6 6s^2$, $5d^7 6s^1$, $5d^6 6s^1 6p^1$, $5d^6 6s^1 7s^1$	567	34122	34122
Fr I	$\mathbf{6p^6 7s^1}$, $6p^6 7p^1$, $6p^6 6d^1$, $6p^6 8s^1$, $6p^6 8p^1$, $6p^6 7d^1$, $6p^6 9s^1$, $6p^6 9p^1$, $6p^6 8d^1$, $6p^6 10s^1$	16	51	18
Fr II	$\mathbf{6p^6}$, $6p^5 7s^1$, $6p^5 6d^1$, $6p^5 7p^1$, $6p^5 8s^1$, $6p^5 7d^1$, $6p^5 5f^1$, $6p^5 8p^1$, $6p^5 9s^1$, $6p^5 6f^1$, $6p^5 8d^1$, $6p^5 9p^1$	103	1569	132
Fr III	$\mathbf{6s^2 6p^5}$, $6s^1 6p^6$, $6s^2 6p^4 6d^1$, $6s^2 6p^4 7s^1$, $6s^2 6p^4 7p^1$, $6s^2 6p^4 5f^1$, $6s^2 6p^4 7d^1$, $6s^2 6p^4 8s^1$, $6s^2 6p^4 8p^1$, $6s^2 6p^4 6f^1$, $6s^2 6p^4 9s^1$	185	4932	1231
Fr IV	$\mathbf{6s^2 6p^4}$, $6s^1 6p^5$, $6s^2 6p^3 6d^1$, $6s^2 6p^3 7s^1$, $6s^2 6p^3 7d^1$, $6s^2 6p^3 8s^1$, $6s^2 6p^3 8d^1$, $6s^2 6p^3 9s^1$	153	410	307
Fr V	$\mathbf{6p^3}$, $6p^2 7s^1$, $6p^2 7p^1$, $6p^2 6d^1$, $6p^2 8s^1$, $6p^2 8p^1$, $6p^2 7d^1$, $6p^2 9s^1$, $6p^2 9p^1$, $6p^2 8d^1$	176	4986	2656

Continued on next page

Table D.1 – *Continued from previous page*

Ion	Configurations	N_{level}	N_{line}	N^*_{line}
Fr VI	$\mathbf{6p^2}$, $6p^17s^1$, $6p^17p^1$, $6p^16d^1$, $6p^18s^1$, $6p^18p^1$, $6p^17d^1$, $6p^15f^1$, $6p^19s^1$, $6p^19p^1$, $6p^18d^1$	95	1398	1398
Fr VII	$\mathbf{6s^26p^1}$, $6s^16p^2$, $6s^27s^1$, $6s^27p^1$, $6s^26d^1$, $6s^28s^1$, $6s^28p^1$, $6s^27d^1$, $6s^25f^1$	22	85	0
Fr VIII	$\mathbf{5d^{10}6s^2}$, $5d^{10}6s^2$, $5d^{10}6s^16p^1$, $5d^{10}6s^17s^1$, $5d^96s^26p^1$, $5d^{10}6s^17p^1$, $5d^{10}6s^16d^1$, $5d^{10}6s^18s^1$, $5d^{10}6s^18p^1$, $5d^{10}6s^17d^1$, $5d^{10}6s^15f^1$	41	229	229
Fr IX	$\mathbf{5d^{10}6s^1}$, $5d^96s^2$, $5d^{10}6p^1$, $5d^96s^16p^1$, $5d^{10}7s^1$, $5d^{10}7p^1$, $5d^{10}6d^1$, $5d^{10}8s^1$, $5d^{10}8p^1$, $5d^{10}6s^1$	36	141	5
Fr X	$\mathbf{5d^{10}}$, $5d^96s^1$, $5d^86s^2$, $5d^86s^16p^1$, $5d^96p^1$, $5d^97s^1$, $5d^86s^17s^1$	152	2729	2729
Fr XI	$\mathbf{5d^9}$, $5d^76s^2$, $5d^86s^1$, $5d^76s^16p^1$, $5d^76s^17s^1$	324	12007	12007
Ra I	$\mathbf{7s^2}$, $7s^17p^1$, $7s^16d^1$, $7s^18s^1$, $6d^17p^1$, $7s^18p^1$, $7p^2$, $7s^17d^1$, $7s^19s^1$, $7s^15f^1$, $7s^16f^1$, $6d^18p^1$, $7d^17p^1$, $7d^18p^1$, $7p^18p^1$, $7s^18d^1$, $8s^17d^1$, $8s^18d^1$, $9s^17d^1$, $9s^18d^1$	112	2024	75
Ra II	$\mathbf{6p^67s^1}$, $6p^68s^1$, $6p^69s^1$, $6p^66d^1$, $6p^67d^1$, $6p^68d^1$, $6p^67p^1$, $6p^68p^1$, $6p^65f^1$, $6p^66f^1$	17	48	7
Ra III	$\mathbf{6p^6}$, $6p^56d^1$, $6p^57s^1$, $6p^55f^1$, $6p^57p^1$, $6p^57d^1$, $6p^58s^1$, $6p^56f^1$, $6p^58p^1$, $6p^58d^1$, $6p^59s^1$	93	1251	252
Ra IV	$\mathbf{6s^26p^5}$, $6s^16p^6$, $6s^26p^46d^1$, $6s^26p^47s^1$, $6s^26p^47p^1$	60	574	457
Ra V	$\mathbf{6p^4}$, $6p^37s^1$, $6p^37p^1$, $6p^36d^1$, $6p^38s^1$, $6p^38p^1$, $6p^37d^1$, $6p^39p^1$, $6p^38d^1$, $6p^310p^1$	251	9553	4793
Ra VI	$\mathbf{6p^3}$, $6p^27s^1$, $6p^27p^1$, $6p^26d^1$, $6p^28s^1$, $6p^28p^1$, $6p^27d^1$, $6p^29s^1$, $6p^29p^1$, $6p^28d^1$	176	4986	3201
Ra VII	$\mathbf{6p^2}$, $6p^17s^1$, $6p^17p^1$, $6p^16d^1$, $6p^18s^1$, $6p^18p^1$, $6p^17d^1$, $6p^15f^1$, $6p^19s^1$, $6p^19p^1$, $6p^18d^1$	95	1398	1398
Ra VIII	$\mathbf{6s^26p^1}$, $6s^16p^2$, $6s^27s^1$, $6s^27p^1$, $6s^26d^1$, $6s^28s^1$, $6s^28p^1$, $6s^27d^1$, $6s^25f^1$	22	85	85
Ra IX	$\mathbf{5d^{10}6s^2}$, $5d^{10}6s^2$, $5d^{10}6s^16p^1$, $5d^{10}6s^17s^1$, $5d^96s^26p^1$, $5d^{10}6s^17p^1$, $5d^{10}6s^16d^1$, $5d^{10}6s^18s^1$, $5d^{10}6s^18p^1$, $5d^{10}6s^17d^1$, $5d^{10}6s^15f^1$	41	229	229
Ra X	$\mathbf{5d^{10}6s^1}$, $5d^96s^2$, $5d^{10}6p^1$, $5d^96s^16p^1$, $5d^{10}7s^1$, $5d^{10}7p^1$, $5d^{10}6d^1$, $5d^{10}8s^1$, $5d^{10}8p^1$, $5d^{10}6s^1$	36	141	141
Ra XI	$\mathbf{5d^{10}}$, $5d^96s^1$, $5d^86s^2$, $5d^86s^16p^1$, $5d^96p^1$, $5d^97s^1$, $5d^86s^17s^1$	152	2729	2729

Bibliography

Abbott B. P., et al., 2017a, *GW170817: Observation of Gravitational Waves from a Binary Neutron Star Inspiral*, PhRvL, 119, 161101

Abbott B. P., Abbott R., Abbott T. D., et al. 2017b, *Multi-messenger Observations of a Binary Neutron Star Merger*, ApJL, 848, L12

Abbott B. P., et al., 2017c, *Estimating the Contribution of Dynamical Ejecta in the Kilonova Associated with GW170817*, ApJL, 850, L39

Abbott B. P., et al., 2017d, *On the Progenitor of Binary Neutron Star Merger GW170817*, ApJL, 850, L40

Abbott B. P., Abbott R., Abbott T. D., Acernese F., Ackley K., Adams C., et al. 2018, *GW170817: Measurements of Neutron Star Radii and Equation of State*, PhRvL, 121, 161101

Abbott B. P., et al., 2019, *Search for Gravitational-wave Signals Associated with Gamma-Ray Bursts during the Second Observing Run of Advanced LIGO and Advanced Virgo*, ApJ, 886, 75

Abbott B. P., Abbott R., Abbott T. D., Abraham S., Acernese F., Ackley K., et. al. 2020, *GW190425: Observation of a Compact Binary Coalescence with Total Mass* $\sim$ *3.4* $M_{\odot}$, ApJL, 892, L3

Andreoni I., et al., 2020, *GROWTH on S190814bv: Deep Synoptic Limits on the Optical/Near-infrared Counterpart to a Neutron Star'-'Black Hole Merger*, ApJ, 890, 131

Antoniadis J., et al., 2013, *A Massive Pulsar in a Compact Relativistic Binary*, Science, 340, 448

Arcavi I., 2018, *The First Hours of the GW170817 Kilonova and the Importance of Early Optical and Ultraviolet Observations for Constraining Emission Models*, ApJL, 855, L23

Arcones A., Janka H. T., Scheck L., 2007, *Nucleosynthesis-relevant conditions in neutrino-driven supernova outflows. I. Spherically symmetric hydrodynamic simulations*, A&A, 467, 1227

Arnett W. D., 1982, *Type I supernovae. I - Analytic solutions for the early part of the light curve*, ApJ, 253, 785

Arnould M., Goriely S., 2003, *The p-process of stellar nucleosynthesis: astrophysics and nuclear physics status*, PhR, 384, 1

Banerjee S., Tanaka M., Kawaguchi K., Kato D., Gaigalas G., 2020, *Simulations of Early Kilonova Emission from Neutron Star Mergers*, ApJ, 901, 29

Banerjee S., Tanaka M., Kato D., Gaigalas G., Kawaguchi K., Domoto N., 2022, *Opacity of the highly ionized lanthanides and the effect on the early kilonova*, arXiv e-prints, p. arXiv:2204.06861

Bar-Shalom A., Klapisch M., Oreg J., 2001, *HULLAC, an integrated computer package for atomic processes in plasmas*, JQSRT, 71, 169

Barbieri C., Salafia O. S., Colpi M., Ghirlanda G., Perego A., 2020, *The kilonova of GW190425-like events*, arXiv e-prints, p. arXiv:2002.09395

Barnes J., Kasen D., 2013, *Effect of a High Opacity on the Light Curves of Radioactively Powered Transients from Compact Object Mergers*, ApJ, 775, 18

Barnes J., Kasen D., Wu M.-R., Martínez-Pinedo G., 2016, *Radioactivity and Thermalization in the Ejecta of Compact Object Mergers and Their Impact on Kilonova Light Curves*, ApJ, 829, 110

Bauswein A., Goriely S., Janka H. T., 2013, *Systematics of Dynamical Mass Ejection, Nucleosynthesis, and Radioactively Powered Electromagnetic Signals from Neutron-star Mergers*, ApJ, 773, 78

Bekker H., et al., 2015, *Identifications of* $5s_{1/2}-5p_{3/2}$ *and* $5s^2-5s5p$ *EUV transitions of promethium-like Pt, Ir, Os and Re*, Journal of Physics B: Atomic, Molecular and Optical Physics, 48, 144018

Brown P. J., Breeveld A. A., Holland S., Kuin P., Pritchard T., 2014, *SOUSA: the Swift Optical/Ultraviolet Supernova Archive*, Ap&SS, 354, 89

Burbidge E. M., Burbidge G. R., Fowler W. A., Hoyle F., 1957, *Synthesis of the Elements in Stars*, Reviews of Modern Physics, 29, 547

Cameron A. G. W., 1957, *Nuclear Reactions in Stars and Nucleogenesis*, PASP, 69, 201

Carlson T. A., Nestor C., Wasserman N., Mcdowell J., 1970, *Calculated ionization potentials for multiply charged ions*, Atomic Data and Nuclear Data Tables, 2, 63

Carroll P. K., O'Sullivan G., 1982, *Ground-state configurations of ionic species I though XVI for Z=57-74 and the interpretation of 4d-4f emission resonances in laser-produced plasmas*, Physical Review A, 25, 275

Chevalier R. A., Soker N., 1989, *Asymmetric Envelope Expansion of Supernova 1987A*, ApJ, 341, 867

Connaughton V., Goldstein A., Fermi GBM - LIGO Group 2017, in American Astronomical Society Meeting Abstracts #229. p. 406.08

Côté B., et al., 2019, *Neutron Star Mergers Might Not Be the Only Source of r-process Elements in the Milky Way*, ApJ, 875, 106

Coughlin M. W., Ahumada T., Anand S., De K., et. al. 2019, *GROWTH on S190425z: Searching Thousands of Square Degrees to Identify an Optical or Infrared Counterpart to a Binary Neutron Star Merger with the Zwicky Transient Facility and Palomar Gattini-IR*, ApJL, 885, L19

Coulter D. A., et al., 2017, *Swope Supernova Survey 2017a (SSS17a), the optical counterpart to a gravitational wave source*, Science, 358, 1556

Cowan R. D., 1967, *Atomic Self-Consistent-Field Calculations Using Statistical Approximations for Exchange and Correlation*, Physical Review, 163, 54

Cowan R. D., 1973, *The theory of rare earth eaergy levels and spectra*, Nuclear Instruments and Methods, 110, 173

Cowan R. D., 1977, *Spectra of highly ionized atoms of tokamak interest*, doi:10.2172/7327427

Cowan R. D., 1981a, *The theory of atomic structure and spectra*

Cowan R. D., 1981b, *Progress in the spectroscopy of highly ionized atoms and its use in plasma diagnostics*, PhyS, 24, 615

Cowperthwaite P. S., et al., 2017, *The Electromagnetic Counterpart of the Binary Neutron Star Merger LIGO/Virgo GW170817. II. UV, Optical, and Near-infrared Light Curves and Comparison to Kilonova Models*, ApJL, 848, L17

Dessart L., Ott C. D., Burrows A., Rosswog S., Livne E., 2009, *Neutrino Signatures and the Neutrino-Driven Wind in Binary Neutron Star Mergers*, ApJ, 690, 1681

Dietrich T., Ujevic M., Tichy W., Bernuzzi S., Brügmann B., 2017, *Gravitational waves and mass ejecta from binary neutron star mergers: Effect of the mass ratio*, PhRvD, 95, 024029

Domoto N., Tanaka M., Wanajo S., Kawaguchi K., 2021, *Signatures of r-process Elements in Kilonova Spectra*, ApJ, 913, 26

Dorsman B., et al., 2022, *Prospects of Gravitational Wave Follow-up Through a Wide-field Ultra-violet Satellite: a Dorado Case Study*, arXiv e-prints, p. arXiv:2206.09696

Drout M. R., et al., 2017, *Light curves of the neutron star merger GW170817/SSS17a: Implications for r-process nucleosynthesis*, Science, 358, 1570

Duffell P. C., Quataert E., Kasen D., Klion H., 2018, *Jet Dynamics in Compact Object Mergers: GW170817 Likely Had a Successful Jet*, ApJ, 866, 3

Eastman R. G., Pinto P. A., 1993, *Spectrum Formation in Supernovae: Numerical Techniques*, ApJ, 412, 731

Eichler D., Livio M., Piran T., Schramm D. N., 1989, *Nucleosynthesis, neutrino bursts and γ-rays from coalescing neutron stars*, Nature, 340, 126

Evans P. A., et al., 2017, *Swift and NuSTAR observations of GW170817: Detection of a blue kilonova*, Science, 358, 1565

Fernández R., Metzger B. D., 2013, *Delayed outflows from black hole accretion tori following neutron star binary coalescence*, MNRAS, 435, 502

Fernandez R., Metzger B., 2014, in AAS/High Energy Astrophysics Division #14. AAS/High Energy Astrophysics Division. p. 304.07

Fernández R., Tchekhovskoy A., Quataert E., Foucart F., Kasen D., 2019, *Long-term GRMHD simulations of neutron star merger accretion discs: implications for electromagnetic counterparts*, MNRAS, 482, 3373

Finstad D., De S., Brown D. A., Berger E., Biwer C. M., 2018, *Measuring the Viewing Angle of GW170817 with Electromagnetic and Gravitational Waves*, ApJL, 860, L2

Fontes C. J., Fryer C. L., Hungerford A. L., Hakel P., Colgan J., Kilcrease D. P., Sherrill M. E., 2015, *Relativistic opacities for astrophysical applications*, High Energy Density Physics, 16, 53

Fontes C. J., Fryer C. L., Hungerford A. L., Wollaeger R. T., Rosswog S., Berger E., 2017, *A line-smeared treatment of opacities for the spectra and light curves from macronovae*, arXiv e-prints, p. arXiv:1702.02990

Fontes C. J., Fryer C. L., Hungerford A. L., Wollaeger R. T., Korobkin O., 2020, *A line-binned treatment of opacities for the spectra and light curves from neutron star mergers*, MNRAS, 493, 4143

Frebel A., 2018, *From Nuclei to the Cosmos: Tracing Heavy-Element Production with the Oldest Stars*, Annual Review of Nuclear and Particle Science, 68, 237

Freiburghaus C., Rosswog S., Thielemann F. K., 1999, *R-Process in Neutron Star Mergers*, ApJL, 525, L121

Froese Fischer C., Gaigalas G., Jönsson P., Bieroń J., 2019, *GRASP2018-A Fortran 95 version of the General Relativistic Atomic Structure Package*, Computer Physics Communications, 237, 184

Frostig D., et al., 2022, *An Infrared Search for Kilonovae with the WINTER Telescope. I. Binary Neutron Star Mergers*, ApJ, 926, 152

Fujibayashi S., Kiuchi K., Nishimura N., Sekiguchi Y., Shibata M., 2018, *Mass Ejection from the Remnant of a Binary Neutron Star Merger: Viscous-radiation Hydrodynamics Study*, ApJ, 860, 64

Fujibayashi S., Kiuchi K., Wanajo S., Kyutoku K., Sekiguchi Y., Shibata M., 2022, *Comprehensive study on the mass ejection and nucleosynthesis in the binary neutron star mergers leaving short-lived massive neutron stars*, arXiv e-prints, p. arXiv:2205.05557

Gaigalas G., Kato D., Rynkun P., Radžiūtė L., Tanaka M., 2019, *Extended Calculations of Energy Levels and Transition Rates of Nd II-IV Ions for Application to Neutron Star Mergers*, ApJS, 240, 29

Geng J.-J., Zhang B., Kölligan A., Kuiper R., Huang Y.-F., 2019, *Propagation of a Short GRB Jet in the Ejecta: Jet Launching Delay Time, Jet Structure, and GW170817/GRB 170817A*, ApJL, 877, L40

Gill R., Nathanail A., Rezzolla L., 2019a, *When Did the Remnant of GW170817 Collapse to a Black Hole?*, ApJ, 876, 139

Gill R., Granot J., De Colle F., Urrutia G., 2019b, *Numerical Simulations of an Initially Top-hat Jet and the Afterglow of GW170817/GRB170817A*, ApJ, 883, 15

Goriely S., Bauswein A., Janka H.-T., 2011, *r-process Nucleosynthesis in Dynamically Ejected Matter of Neutron Star Mergers*, ApJL, 738, L32

Goriely S., Bauswein A., Just O., Pllumbi E., Janka H. T., 2015, *Impact of weak interactions of free nucleons on the r-process in dynamical ejecta from neutron star mergers*, MNRAS, 452, 3894

Gottlieb O., Loeb A., 2020, *Electromagnetic signals from the decay of free neutrons in the first hours of neutron star mergers*, MNRAS, 493, 1753

Gu M. F., 2008, *The flexible atomic code*, Canadian Journal of Physics, 86, 675

Hallinan G., et al., 2017, *A radio counterpart to a neutron star merger*, Science, 358, 1579

Hotokezaka K., Nakar E., 2020, *Radioactive Heating Rate of r-process Elements and Macronova Light Curve*, ApJ, 891, 152

Hotokezaka K., Kiuchi K., Kyutoku K., et al. 2013a, *Remnant massive neutron stars of binary neutron star mergers: Evolution process and gravitational waveform*, PhRvD, 88, 044026

Hotokezaka K., Kiuchi K., Kyutoku K., Muranushi T., Sekiguchi Y.-i., Shibata M., Taniguchi K., 2013b, *Remnant massive neutron stars of binary neutron star mergers: Evolution process and gravitational waveform*, PhRvD, 88, 044026

Hulse R. A., Taylor J. H., 1975, *A deep sample of new pulsars and their spatial extent in the Galaxy.*, ApJL, 201, L55

Ioka K., Nakamura T., 2018, *Can an off-axis gamma-ray burst jet in GW170817 explain all the electromagnetic counterparts?*, Progress of Theoretical and Experimental Physics, 2018, 043E02

Just O., Bauswein A., Ardevol Pulpillo R., Goriely S., Janka H. T., 2015, *Comprehensive nucleosynthesis analysis for ejecta of compact binary mergers*, MNRAS, 448, 541

Just O., Kullmann I., Goriely S., Bauswein A., Janka H. T., Collins C. E., 2022, *Dynamical ejecta of neutron star mergers with nucleonic weak processes - II: kilonova emission*, MNRAS, 510, 2820

Kalogera V., Baym G., 1996, *The Maximum Mass of a Neutron Star*, ApJL, 470, L61

Karp A. H., Lasher G., Chan K. L., Salpeter E. E., 1977, *The opacity of expanding media: the effect of spectral lines.*, ApJ, 214, 161

Kasen D., Badnell N. R., Barnes J., 2013, *Opacities and Spectra of the r-process Ejecta from Neutron Star Mergers*, ApJ, 774, 25

Kasen D., Fernández R., Metzger B. D., 2015, *Kilonova light curves from the disc wind outflows of compact object mergers*, MNRAS, 450, 1777

Kasen D., Metzger B., Barnes J., Quataert E., Ramirez-Ruiz E., 2017, *Origin of the heavy elements in binary neutron-star mergers from a gravitational-wave event*, Nature, 551, 80

Kasliwal M. M., Nissanke S., 2014, *On Discovering Electromagnetic Emission from Neutron Star Mergers: The Early Years of Two Gravitational Wave Detectors*, ApJL, 789, L5

Kasliwal M. M., Nakar E., Singer L. P., et al. 2017, *Illuminating gravitational waves: A concordant picture of photons from a neutron star merger*, Science, 358, 1559

Kato D., Sakaue H. A., Murakami I., Nakamura N., 2017, *Population trapping: The mechanism for the lost resonance lines in Pm-like ions*, Nuclear Instruments and Methods in Physics Research B, 408, 16

Kawaguchi K., Shibata M., Tanaka M., 2018, *Radiative Transfer Simulation for the Optical and Near-infrared Electromagnetic Counterparts to GW170817*, ApJL, 865, L21

Kawaguchi K., Shibata M., Tanaka M., 2019, arXiv e-prints, p. arXiv:1908.05815

Kawaguchi K., Shibata M., Tanaka M., 2020, *Diversity of Kilonova Light Curves*, ApJ, 889, 171

Kilbane D., O'Sullivan G., 2010, *Ground-state configurations and unresolved transition arrays in extreme ultraviolet spectra of lanthanide ions*, Physical Review A, 82, 062504

Klion H., Duffell P. C., Kasen D., Quataert E., 2021, *The effect of jet-ejecta interaction on the viewing angle dependence of kilonova light curves*, MNRAS, 502, 865

Klion H., Tchekhovskoy A., Kasen D., Kathirgamaraju A., Quataert E., Fernández R., 2022, *The impact of r-process heating on the dynamics of neutron star merger accretion disc winds and their electromagnetic radiation*, MNRAS, 510, 2968

Kobayashi Y., et al., 2015, *Extreme ultraviolet and visible spectroscopy of promethiumlike heavy ions*, PhRvA, 92, 022510

Korobkin O., Rosswog S., Arcones A., Winteler C., 2012, *On the astrophysical robustness of the neutron star merger r-process*, MNRAS, 426, 1940

Kramida A. E., Reader J., 2006, *Ionization energies of tungsten ions: W^{2+} through W^{71+}*, Atomic Data and Nuclear Data Tables, 92, 457

Kramida A., Yu. Ralchenko Reader J., and NIST ASD Team 2020, NIST Atomic Spectra Database (ver. 5.8), [Online]. Available: `https://physics.nist.gov/asd` [2021, April 15]. National Institute of Standards and Technology, Gaithersburg, MD.

Kromer M., Sim S. A., 2009, *Time-dependent three-dimensional spectrum synthesis for Type Ia supernovae*, MNRAS, 398, 1809

Kulkarni S. R., 2005, *Modeling Supernova-like Explosions Associated with Gamma-ray Bursts with Short Durations*, arXiv e-prints, pp astro–ph/0510256

Kulkarni S. R., et al., 2021, *Science with the Ultraviolet Explorer (UVEX)*, arXiv e-prints, p. arXiv:2111.15608

Kullmann I., Goriely S., Just O., Ardevol-Pulpillo R., Bauswein A., Janka H. T., 2022, *Dynamical ejecta of neutron star mergers with nucleonic weak processes I: nucleosynthesis*, MNRAS, 510, 2804

Kyutoku K., Ioka K., Shibata M., 2014, *Ultrarelativistic electromagnetic counterpart to binary neutron star mergers*, MNRAS, 437, L6

Kyutoku K., Fujibayashi S., Hayashi K., Kawaguchi K., Kiuchi K., Shibata M., Tanaka M., 2020, *On the Possibility of GW190425 Being a Black Hole'-'Neutron Star Binary Merger*, ApJL, 890, L4

LSST Science Collaboration et al., 2009, *LSST Science Book, Version 2.0*, arXiv e-prints, p. arXiv:0912.0201

Lattimer J. M., Schramm D. N., 1974, *Black-Hole-Neutron-Star Collisions*, ApJL, 192, L145

Law N. M., Kulkarni S. R., et al. 2009, *The Palomar Transient Factory: System Overview, Performance, and First Results*, PASP, 121, 1395

Li L.-X., Paczyński B., 1998, *Transient Events from Neutron Star Mergers*, ApJL, 507, L59

Li S.-Z., Liu L.-D., Yu Y.-W., Zhang B., 2018, *What Powered the Optical Transient AT2017gfo Associated with GW170817?*, The Astrophysical Journal, 861, L12

Lippuner J., Fernández R., Roberts L. F., Foucart F., Kasen D., Metzger B. D., Ott C. D., 2017, *Signatures of hypermassive neutron star lifetimes on r-process nucleosynthesis in the disc ejecta from neutron star mergers*, MNRAS, 472, 904

Lodders K., 2003, *Solar System Abundances and Condensation Temperatures of the Elements*, ApJ, 591, 1220

Mann J. B., Waber J. T., 1973, *Self-Consistent Relativistic Dirac-Hartree-Fock Calculations of Lanthanide Atoms*, Atomic Data, 5, 201

Martin W. C., Sugar J., 1973, *Classifications of the Resonance Lines of Europium M*, ApJ, 184, 671

Martin W. C., Zalubas R., Hagan L., 1978, *Atomic energy levels - The rare-Earth elements*

Martin D., Perego A., Arcones A., Korobkin O., Thielemann F.-K., 2015, *Nucleosynthesis in the Ejecta of Neutron Star Mergers*, arXiv e-prints, p. arXiv:1509.07628

Martin D., Perego A., Kastaun W., Arcones A., 2018, *The role of weak interactions in dynamic ejecta from binary neutron star mergers*, Classical and Quantum Gravity, 35, 034001

Matsumoto T., Ioka K., Kisaka S., Nakar E., 2018, *Is the Macronova in GW170817 Powered by the Central Engine?*, ApJ, 861, 55

Metzger B. D., Fernández R., 2014, *Red or blue? A potential kilonova imprint of the delay until black hole formation following a neutron star merger*, MNRAS, 441, 3444

Metzger B. D., Piro A. L., Quataert E., 2008, *Time-dependent models of accretion discs formed from compact object mergers*, MNRAS, 390, 781

Metzger B. D., et al., 2010, *Electromagnetic counterparts of compact object mergers powered by the radioactive decay of r-process nuclei*, MNRAS, 406, 2650

Metzger B. D., Bauswein A., Goriely S., Kasen D., 2015, *Neutron-powered precursors of kilonovae*, MNRAS, 446, 1115

Metzger B. D., Thompson T. A., Quataert E., 2018, *A Magnetar Origin for the Kilonova Ejecta in GW170817*, ApJ, 856, 101

Mihalas D., Kunasz P. B., 1978, *Solution of the comoving-frame equation of transfer in spherically symmetric flows. V. Multilevel atoms.*, ApJ, 219, 635

Miller J. M., et al., 2019a, *Full transport model of GW170817-like disk produces a blue kilonova*, PhRvD, 100, 023008

Miller J. M., et al., 2019b, *Full transport model of GW170817-like disk produces a blue kilonova*, PhRvD, 100, 023008

Mooley K. P., Mooley S., 2017, *LIGO/Virgo GW170817: X-ray observations confirm prediction made from radio data.*, GRB Coordinates Network, 22211, 1

Nakar E., Piran T., 2017, *The Observable Signatures of GRB Cocoons*, ApJ, 834, 28

Narayan R., Paczynski B., Piran T., 1992, *Gamma-Ray Bursts as the Death Throes of Massive Binary Stars*, ApJL, 395, L83

Nativi L., Bulla M., Rosswog S., Lundman C., Kowal G., Gizzi D., Lamb G. P., Perego A., 2021, *Can jets make the radioactively powered emission from neutron star mergers bluer?*, MNRAS, 500, 1772

Nativi L., Lamb G. P., Rosswog S., Lundman C., Kowal G., 2022, *Are interactions with neutron star merger winds shaping the jets?*, MNRAS, 509, 903

Nicholl M., et al., 2017, *The Electromagnetic Counterpart of the Binary Neutron Star Merger LIGO/Virgo GW170817. III. Optical and UV Spectra of a Blue Kilonova from Fast Polar Ejecta*, ApJL, 848, L18

Nishimura N., Takiwaki T., Thielemann F.-K., 2015, *The r-process Nucleosynthesis in the Various Jet-like Explosions of Magnetorotational Core-collapse Supernovae*, ApJ, 810, 109

Nissanke S., Sievers J., Dalal N., Holz D., 2011, *Localizing Compact Binary Inspirals on the Sky Using Ground-based Gravitational Wave Interferometers*, ApJ, 739, 99

Nissanke S., Kasliwal M., Georgieva A., 2013, *Identifying Elusive Electromagnetic Counterparts to Gravitational Wave Mergers: An End-to-end Simulation*, ApJ, 767, 124

Nomoto K., Thielemann F. K., Wheeler J. C., 1984, *Explosive nucleosynthesis and Type I supernovae*, ApJL, 279, L23

Oechslin R., Janka H. T., Marek A., 2007, *Relativistic neutron star merger simulations with non-zero temperature equations of state. I. Variation of binary parameters and equation of state*, A&A, 467, 395

Ott U., Stephan T., Hoppe P., Savina M. R., 2019, *Isotopes of Barium as a Chronometer for Supernova Dust Formation*, ApJ, 885, 128

Özel F., Freire P., 2016, *Masses, Radii, and the Equation of State of Neutron Stars*, ARA&A, 54, 401

Paczynski B., 1986, *Gamma-ray bursters at cosmological distances*, ApJL, 308, L43

Perego A., 2018, in Journal of Physics Conference Series. p. 012018, doi:10.1088/1742-6596/940/1/012018

Perego A., Rosswog S., Cabezón R. M., Korobkin O., Käppeli R., Arcones A., Liebendörfer M., 2014, *Neutrino-driven winds from neutron star merger remnants*, MNRAS, 443, 3134

Perego A., Radice D., Bernuzzi S., 2017, *AT 2017gfo: An Anisotropic and Three-component Kilonova Counterpart of GW170817*, ApJL, 850, L37

Perego A., et al., 2022, *Production of Very Light Elements and Strontium in the Early Ejecta of Neutron Star Mergers*, ApJ, 925, 22

Pereira R., et al., 2013, *Spectrophotometric time series of SN 2011fe from the Nearby Supernova Factory*, A&A, 554, A27

Peters P. C., Mathews J., 1963, *Gravitational Radiation from Point Masses in a Keplerian Orbit*, Physical Review, 131, 435

Pian E., D'Avanzo P., Benetti S., Branchesi M., et al. 2017, *Spectroscopic identification of r-process nucleosynthesis in a double neutron-star merger*, Nature, 551, 67

Pinto P. A., Eastman R. G., 2000, *The Type Ia Supernova Width-Luminosity Relation*, arXiv e-prints, pp astro–ph/0006171

Piro A. L., Kollmeier J. A., 2018, *Evidence for Cocoon Emission from the Early Light Curve of SSS17a*, ApJ, 855, 103

Pognan Q., Jerkstrand A., Grumer J., 2022, *NLTE effects on kilonova expansion opacities*, MNRAS, 513, 5174

Priti Mita M., Kato D., Murakami I., Sakaue H. A., Nakamura N., 2020, *Identification of visible lines from multiply charged W^{8+} and W^{9+} ions*, PhRvA, 102, 042818

Radice D., Galeazzi F., Lippuner J., Roberts L. F., Ott C. D., Rezzolla L., 2016, *Dynamical mass ejection from binary neutron star mergers*, MNRAS, 460, 3255

Radice D., Perego A., Hotokezaka K., Fromm S. A., Bernuzzi S., Roberts L. F., 2018, *Binary Neutron Star Mergers: Mass Ejection, Electromagnetic Counterparts, and Nucleosynthesis*, ApJ, 869, 130

Radžiūtė L., Gaigalas G., Kato D., Rynkun P., Tanaka M., 2020, *Extended calculations of energy levels and transition rates for singly ionized lanthanide elements I: Pr - Gd*, arXiv e-prints, p. arXiv:2002.08075

Rastinejad J. C., et al., 2022, *A Kilonova Following a Long-Duration Gamma-Ray Burst at 350 Mpc*, arXiv e-prints, p. arXiv:2204.10864

Richers S., Kasen D., O'Connor E., Fernández R., Ott C. D., 2015, *Monte Carlo Neutrino Transport through Remnant Disks from Neutron Star Mergers*, ApJ, 813, 38

Roberts L. F., Kasen D., Lee W. H., Ramirez-Ruiz E., 2011, *Electromagnetic Transients Powered by Nuclear Decay in the Tidal Tails of Coalescing Compact Binaries*, ApJL, 736, L21

Rodrigues G. C., Indelicato P., Santos J. P., Patté P., Parente F., 2004, *Systematic calculation of total atomic energies of ground state configurations*, Atomic Data and Nuclear Data Tables, 86, 117

Roming P. W. A., et al., 2005, *The Swift Ultra-Violet/Optical Telescope*, SSRv, 120, 95

Rosswog S., Brüggen M., 2011, *Introduction to High-Energy Astrophysics*

Rosswog S., Sollerman J., Feindt U., Goobar A., Korobkin O., Wollaeger R., Fremling C., Kasliwal M. M., 2018, *The first direct double neutron star merger detection: Implications for cosmic nucleosynthesis*, A&A, 615, A132

Rybicki G. B., Lightman A. P., 1986, *Radiative Processes in Astrophysics*

Rynkun P., Banerjee S., Gaigalas G., Tanaka M., Radžiūtė L., Kato D., 2022, *Theoretical investigation of energy levels and transition for Ce IV*, A&A, 658, A82

Sagiv I., et al., 2014, *Science with a Wide-field UV Transient Explorer*, AJ, 147, 79

Savchenko V., et al., 2017a, in Proceedings of the 7th International Fermi Symposium. p. 58

Savchenko V., et al., 2017b, *INTEGRAL Detection of the First Prompt Gamma-Ray Signal Coincident with the Gravitational-wave Event GW170817*, ApJL, 848, L15

Schlegel D. J., Finkbeiner D. P., Davis M., 1998, *Maps of Dust Infrared Emission for Use in Estimation of Reddening and Cosmic Microwave Background Radiation Foregrounds*, ApJ, 500, 525

Sekiguchi Y., Kiuchi K., Kyutoku K., Shibata M., 2015, *Dynamical mass ejection from binary neutron star mergers: Radiation-hydrodynamics study in general relativity*, PhRvD, 91, 064059

Sekiguchi Y., Kiuchi K., Kyutoku K., Shibata M., Taniguchi K., 2016, *Dynamical mass ejection from the merger of asymmetric binary neutron stars: Radiation-hydrodynamics study in general relativity*, PhRvD, 93, 124046

Shibata M., Hotokezaka K., 2019, *Merger and Mass Ejection of Neutron Star Binaries*, Annual Review of Nuclear and Particle Science, 69, 41

Shibata M., Fujibayashi S., Hotokezaka K., Kiuchi K., Kyutoku K., Sekiguchi Y., Tanaka M., 2017, *Modeling GW170817 based on numerical relativity and its implications*, PhRvD, 96, 123012

Siegel D. M., Metzger B. D., 2017, *Three-Dimensional General-Relativistic Magnetohydrodynamic Simulations of Remnant Accretion Disks from Neutron Star Mergers: Outflows and r -Process Nucleosynthesis*, PhRvL, 119, 231102

Smartt S. J., et al., 2017, *A kilonova as the electromagnetic counterpart to a gravitational-wave source*, Nature, 551, 75

Sobolev V. V., 1960, *The Theory of Stellar Evolution*, Soviet Ast., 4, 372

Srivastav S., Ninan J. P., Kumar B., Anupama G. C., Sahu D. K., Ojha D. K., Prabhu T. P., 2016, *Optical and NIR observations of the nearby type Ia supernova SN 2014J*, MNRAS, 457, 1000

Sugar J., 1965, *Analysis of the Spectrum of Triply Ionized Praseodymium (Pr IV)*, Journal of the Optical Society of America (1917-1983), 55, 1058

Sugar J., 1975, *Ionization energies of quadruply ionized rare earths*, Journal of the Optical Society of America (1917-1983), 65, 1366

Sugar J., Kaufman V., 1975, *Seventh spectrum of tungsten (W vii); resonance lines of Hf v*, PhRvA, 12, 994

Tanaka M., 2016, *Kilonova/Macronova Emission from Compact Binary Mergers*, Advances in Astronomy, 2016, 634197

Tanaka M., Hotokezaka K., 2013, *Radiative Transfer Simulations of Neutron Star Merger Ejecta*, ApJ, 775, 113

Tanaka M., Hotokezaka K., Kyutoku K., Wanajo S., Kiuchi K., Sekiguchi Y., Shibata M., 2014, *Radioactively Powered Emission from Black Hole-Neutron Star Mergers*, ApJ, 780, 31

Tanaka M., et al., 2017, *Kilonova from post-merger ejecta as an optical and near-Infrared counterpart of GW170817*, PASJ, 69, 102

Tanaka M., et al., 2018, *Properties of Kilonovae from Dynamical and Post-merger Ejecta of Neutron Star Mergers*, ApJ, 852, 109

Tanaka M., Kato D., Gaigalas G., Kawaguchi K., 2020, *Systematic opacity calculations for kilonovae*, MNRAS, 496, 1369

Tanvir N. R., Levan A. J., Fruchter A. S., Hjorth J., Hounsell R. A., Wiersema K., Tunnicliffe R. L., 2013, *A 'kilonova' associated with the short-duration γ-ray burst GRB 130603B*, Nature, 500, 547

Tauris T. M., et al., 2017, *Formation of Double Neutron Star Systems*, ApJ, 846, 170

Taylor J. H., Weisberg J. M., 1982, *A new test of general relativity - Gravitational radiation and the binary pulsar PSR 1913+16*, ApJ, 253, 908

Troja E., et al., 2017, *The X-ray counterpart to the gravitational-wave event GW170817*, Nature, 551, 71

Utsumi Y., Tanaka M., Tominaga N., Yoshida M., et al. 2017, *J-GEM observations of an electromagnetic counterpart to the neutron star merger GW170817*, PASJ, 69, 101

Valenti S., et al., 2017, *The Discovery of the Electromagnetic Counterpart of GW170817: Kilonova AT 2017gfo/DLT17ck*, ApJL, 848, L24

Verner D. A., Ferland G. J., Korista K. T., Yakovlev D. G., 1996, *Atomic Data for Astrophysics. II. New Analytic FITS for Photoionization Cross Sections of Atoms and Ions*, ApJ, 465, 487

Villar V. A., et al., 2017, *The Combined Ultraviolet, Optical, and Near-infrared Light Curves of the Kilonova Associated with the Binary Neutron Star Merger GW170817: Unified Data Set, Analytic Models, and Physical Implications*, ApJL, 851, L21

Wanajo S., Sekiguchi Y., Nishimura N., et al. 2014, *Production of All the r-process Nuclides in the Dynamical Ejecta of Neutron Star Mergers*, ApJL, 789, L39

Wanderman D., Piran T., 2010, *The luminosity function and the rate of Swift's gamma-ray bursts*, MNRAS, 406, 1944

Watson D., et al., 2019, *Identification of strontium in the merger of two neutron stars*, Nature, 574, 497

Waxman E., Ofek E. O., Kushnir D., Gal-Yam A., 2018, *Constraints on the ejecta of the GW170817 neutron star merger from its electromagnetic emission*, MNRAS, 481, 3423

Wollaeger R. T., Hungerford A. L., Fryer C. L., Wollaber A. B., van Rossum D. R., Even W., 2017, *Light Curves and Spectra from a Unimodal Core-collapse Supernova*, ApJ, 845, 168

Wollaeger R. T., et al., 2019, *Impact of Pulsar and Fallback Sources on Multifrequency Kilonova Models*, ApJ, 880, 22

Wolszczan A., 1991, *A nearby 37.9-ms radio pulsar in a relativistic binary system*, Nature, 350, 688

Woosley S. E., Heger A., 2007, *Nucleosynthesis and remnants in massive stars of solar metallicity*, PhR, 442, 269

Wybourne B. G., 1965, *Spectroscopic Properties of Rare Earths*

Wybourne B. G., Meggers W. F., 1965, *Spectroscopic Properties of Rare Earths*, Physics Today, 18, 70

Yang S., GRAWITA and DLT40 Project 2018, in González G., Hynes R., eds, IAU Symposium Vol. 338, IAU Symposium. pp 9–13 (arXiv:1801.06506), doi:10.1017/S1743921318000157

Yang S., et al., 2017, *An Empirical Limit on the Kilonova Rate from the DLT40 One Day Cadence Supernova Survey*, ApJL, 851, L48

Yaron O., Gal-Yam A., 2012, *WISeREP—An Interactive Supernova Data Repository*, PASP, 124, 668

Yu Y.-W., Zhang B., Gao H., 2013, *Bright "Merger-nova" from the Remnant of a Neutron Star Binary Merger: A Signature of a Newly Born, Massive, Millisecond Magnetar*, ApJL, 776, L40